UNITED STATES DEPARTMENT OF THE INTERIOR

GEOLOGICAL SURVEY

Geochemistry and Mineralogy of the Carbonates of the Creede Mining District, Colorado

by

Pamela H. Wetlaufer
U.S.Geological Survey

Open-File Report 77-706
1977

The material in this report has been submitted as a thesis to George Washington University in partial fulfillment of the requirements for the degree of Master of Science

ACKNOWLEDGEMENTS

The support and advice of many persons helped to make this study possible, and I would like to extend my thanks to all of them. Philip M. Bethke and Paul B. Barton, Jr. suggested this study and have been most helpful in guiding its course. John F. Lewis has contributed many constructive suggestions and comments. L. B. Wiggins provided extensive instruction on the use of the electron microprobe. John L. Haas created the computer program with which the microprobe analyses were plotted and manipulated. Howard T. Evans provided instruction on the use of the Guinier-Haig powder camera and on the taking of single crystal photographs; he also helped with the interpreting of the powder and single crystal patterns. Robert O. Rye and Joseph Whelan made all the isotope measurements. Daniel Appleman helped to locate samples in the mineral collection of the U.S. National Museum of Natural History for microprobe standards. J. S. Huebner donated the rhodochrosite microprobe standard. Gerald B. Wetlaufer provided many useful editorial suggestions.

Carbonate samples were collected courtesy of the Emperius Mining Company and of Homestake Mining Company. M. M. Roeber, Michael McClure, Arthur Benson and John Jackson have contributed special samples to the study.

TABLE OF CONTENTS

LIST OF TABLES

LIST OF ILLUSTRATIONS

ABSTRACT

This paper describes the results of a study of the carbonate gangue in the silver-base metal ore deposit of the Creede mining district, located in Tertiary volcanic rocks of the central San Juan Mountains, southwestern Colorado. Two carbonate stages can be distinguished and defined on the basis of mineral association, compositional range and position in the sequence of ore deposition. Electron microprobe analyses show that the early pre-ore carbonate stage is comprised of rhodochrosite with a compositional range of 68 to 93 mole percent $MnCO_3$, 7 to 32 mole percent $FeCO_3$, 2 to 15 mole percent $CaCO_3$, and 0.5 to 4 mole percent $MgCO_3$. The later intra-ore carbonate stage is made up of siderite-manganosiderite with a broad range of iron content (33 to 94 mole percent $FeCO_3$; 6 to 67 mole percent $MnCO_3$; 1 to 13 mole percent $CaCO_3$; and 1 to 10 mole percent $MgCO_3$). Both carbonate stages are spatially restricted within the vein system, the rhodochrosite limited to the southern third and the siderite limited to the northern two-thirds. The two stages have not been found at the same sample locality.

The two stages of carbonate define two of the five main depositional stages in the history of the Creede hydrothermal system and thereby document broad scale variations within the depositing, and continually evolving fluids. However, the complexity of the textural and mineralogical variations within each carbonate stage limits their usefulness in unraveling the finer details of the character of the ore fluids. The frequently massive rhodochrosite has undergone several periods of leaching and regrowth

which, except at one locality, cannot be resolved by compositional, textural or color variations. Although some compositionally zoned siderite rhombs have been documented, the siderite, too, has had a complicated history of leaching and regrowth. The zoning indicates (1) an early low-calcium siderite + hematite growth followed by (2) relatively high-calcium siderite deposition (without hematite) followed by (3) low-calcium siderite deposition without hematite. The composition of the high-calcium siderite lies well outside of the recognized stability field for siderite at 250°C and, therefore, is considered either a metastable phase or possibly a new mineral.

Carbon and oxygen isotopic compositions of the carbonates together with the hydrogen isotopic composition of inclusion fluids suggest that the fluids depositing the carbonates either were deep-seated in origin, or, less likely, were meteoric waters which came in contact with a large volume of magmatic rock with which it exchanged isotopes. The oxygen and hydrogen isotopic compositions of the fluids that deposited the carbonates are significantly different from those that yielded the other vein minerals (sphalerite, chlorite, sericite, quartz, adularia). The latter minerals appear to have been deposited from two distinctive fluids of meteoric origin.

The stability fields of minerals present during the carbonate stages have been calculated for 250°C. The results indicate that conditions during carbonate deposition were not drastically different from those suggested by Barton and others (1977) for main-stage ore deposition, although little ore, if any, was deposited during the carbonate stages. A new value for the free energy of formation of siderite was calculated since all of the most recently published values predict too small a stability field for the siderite based on the occurrence of siderite at Creede. The change to the more iron-rich

composition of the later stage carbonate was probably controlled by the pyrite-chlorite buffer which was not present during early-stage carbonate deposition.

I. INTRODUCTION

This study is part of a U.S. Geological Survey program of research focussed on the Ag-Pb-Zn-Cu ore deposit of the Creede District, Mineral County, Colorado. The purpose of this program, which has been intermittently pursued since 1959, is to identify and define parameters with which to quantify the physical and chemical environment of metallic ore deposits. The Creede deposit was selected because of the history of open-fracture filling, the uniform wallrock, the lack of major post-mineralization movement, and the well-documented geology of the area (Steven and Ratté, 1965). Although the Creede deposit is far more complex than was originally thought, this complexity sets limits only on the degree of detail with which the filling history of the deposit can be documented.

The Creede study seeks to provide a better understanding of the detailed evolution of an ore deposit in time and space. Among the more important questions to be answered are: Does the ore-bearing fluid evolve as it passes through the hydrothermal system depositing the ore? Does the fluid change with time at depth? What are the sources of both the metals in solution and the transporting waters? What were the physical conditions imposed on the system such as pressure (depth of the system) and temperature? This paper will deal with aspects of these questions which pertain to carbonate deposition at Creede.

Approaches currently being used in the U.S.G.S. program to define the environment of ore deposition and the time/space relationships at Creede include: 1) light stable isotopic compositions (δD, $\delta^{18}O$, $\delta^{34}S$ and $\delta^{13}C$)

to determine the source(s) of the hydrothermal waters and of some of the elements within them and the degree of interaction with the wallrock; 2) fluid inclusion studies to determine the temperature of deposition, the salinity of the waters, the concentration of metals in the ore fluids and the pressure under which the fluids deposited the ore (as evidenced through boiling); 3) mineralogical and petrological studies of the ore and gangue minerals and of wallrock alteration to determine the presence and degree of equilibrium (Barton and others, 1963) and their time/space relationships and 4) experimental work on the solubilities and phase relations among the commonly found minerals at Creede.

Three papers have already been published in the series on the environment of ore deposition at Creede. Steven and Eaton (1975) described the geologic, hydrologic and geophysical setting of the Creede district. Bethke and others (1976) documented the age of mineralization and its position in time with respect to the sequence of volcanic activity. Barton and others (1977) discussed the chemistry of the ore-forming fluid and proposed an ore deposition model for the district.

II. THE CREEDE MINING DISTRICT

Location

The Creede mining district is located in Mineral County, in the central San Juan Mountains, southwestern Colorado (fig. 1). Most of the mining activity has been concentrated in the drainage basins of various tributaries of the Rio Grande, those being East Willow Creek, West Willow Creek, Windy Gulch, Rat Creek and Miners Creek. The main producing mines lie north of the town of Creede (population approximately 750 in 1976) which is situated on Willow Creek about two miles north of its junction with the Rio Grande. The altitude within the Creede district varies from 2590 m. to 4235 m.; the higher areas have been intensely glaciated.

Previous Investigations

The earliest detailed accounts of the geology and ore deposits of the Creede district can be found in two reports by Emmons and Larsen (1913; 1923). Larsen (1930) discussed the new mining developments between the years 1913 and 1927. Little was published from that time until the 1960's. Steven and Ratté (1965) provided the next major re-examination and updating of the geology, structure, and mining developments of the Creede district. A later paper (Ratté and Steven, 1967) described the petrography, areal distribution and chemistry of the ash flows and related volcanics of the Creede district. A geologic map of the Creede quadrangle was published in 1973 (Steven and Ratté, 1973). An unpublished Master's thesis (Cannaday, 1950) documented the OH vein mineralogy and the structural relations

between the OH vein and the Amethyst vein. Two unpublished Ph.D. dissertations (Chaffee, 1967; Hull, 1970) discussed respectively the geology and hydrothermal alteration north of the Creede district and the geology of the Bulldog vein system.

Production History[1]

The first discovery of mineralization in the Creede district was on the Alpha claim, located on the Alpha Corsair fault in 1869. Production was short-lived because the available metallurgical technology was not adequate to extract the silver, which occurred in oxidized, near-surface ores. Although several claims were established in the mid-1880's, major ore discovery did not take place until 1889 when Nicholas Creede located the Solomon-Holy Moses vein. High-grade silver ore along the Amethyst fault zone was discovered in 1891. In response to these ore discoveries, the town of Creede (population 600 in 1889) swelled into a city of 10,000 people by the end of 1891.

The greatest bonanzas of the district were in the near-surface oxidized or partly oxidized ores of the southern segment of the Amethyst vein. Almost the entire production during the boom period from 1891 through 1900 came from these oxidized ores along the Amethyst vein.

By 1900, the northern part of the Amethyst vein was furnishing sulfide ore consisting of lead, zinc, some silver and gold, and a little cadmium. Due to the increasing proportion of sulfides with relatively low silver contents in the district, mining activity in the early 1900's began to diminish. The years 1911-1914 saw the progressive exhaustion of the better

---

[1]This summary is based on information from Emmons and Larsen (1923), Larsen (1930), Steven and Ratté (1965), and Meeves and Darnell (1968).

grade ores from the upper levels of the mines, and since 1920, the main Amethyst vein itself has produced very little ore. However, several rich subsidiary veins in the hanging wall of the Amethyst fault zone and the high-silver Monon Hill ores kept the district in production through the 1920's. Mining activity continued to decline throughout the 1920's until a sharp drop in the price of silver caused the closing of all the mines in the district in 1930. The mines were reopened in 1934 when the price of silver was "pegged" by the Federal Government at roughly double the then current market price.

Most of the production in the 1940's and 1950's came from the OH vein, a major structure discovered in 1938 or 1939 in the hanging wall of the Amethyst fault zone. A second major hanging wall structure, the P vein, which parallels the OH vein 0.6 km to the north, was discovered by accident in 1960 when driving a crosscut for ventilation. The most recent major ore discovery came in 1961 when exploration in the Bulldog Mountain area indicated the presence of mineralization along the Bulldog Mountain fault. The technological difficulties of mining the thin, frequently unconsolidated, vertical veins were formidable (Jackson, 1974), but production finally began in 1969. Total value of silver, lead, zinc, gold and copper extracted from the Creede district was 69.5 million dollars through 1966 (Meeves and Darnell, 1968).

Regional Geology[2]

The Creede district lies near the center of the San Juan Mountains (fig. 1), the largest erosional remnant of a volcanic field which covered

[2]The geology of the San Juan Mountains has been described in detail in Larsen and Cross (1956), Steven and others (1967), Lipman and others (1970),

Figure 1. Location of the Creede mining district and extent of the San Juan Mountains volcanic field. From Steven and Ratté (1965).

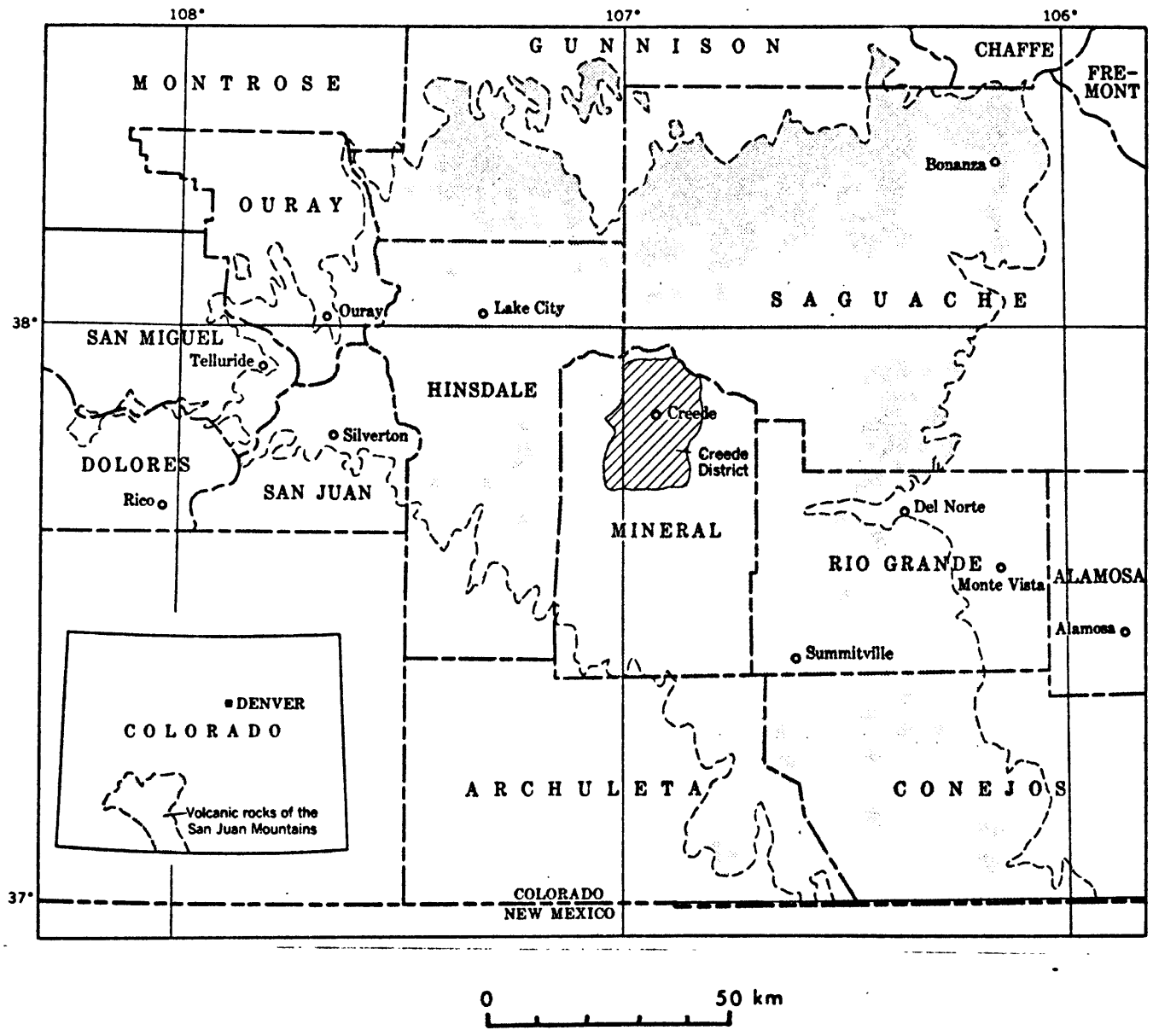
108°
107°
106°
GUNNISON
CHAFFE
FRE-
MONT
MONTROSE
OURAY
Bonanza
Ouray
Lake City
SAGUACHE
38°
SAN MIGUEL
Telluride
HINSDALE
Creede
Silverton
Creede
District
DOLORES
SAN JUAN
Rico
Del Norte
MINERAL
RIO GRANDE
Monte Vista
ALAMOSA
Alamosa
Summitville
DENVER
COLORADO
Volcanic rocks of the
San Juan Mountains
ARCHULETA
CONEJOS
37°
COLORADO
NEW MEXICO
0
50 km

most of the southern Rocky Mountains in middle Tertiary time. The volcanic sequence probably directly overlies Precambrian igneous and metamorphic rocks. Tweto (1968) suggested that post-Precambrian and pre-Jurassic strata were eroded away, except in fringe areas, after formation of the late Paleozoic/early Mesozoic Uncompahgre-San Luis highland. No pre-Tertiary rocks outcrop in the Creede district, although projection of Jurassic and Cretaceous sedimentary units from the southern fringe areas indicates that these units could possibly underlie the district (Steven, 1969).

The volcanic history of the San Juan Mountains has been documented by Lipman and others (1970) based on extensive mapping and K-Ar dating. Volcanic activity began about 40 to 35 m.y. ago when scattered volcanic centers erupted intermediate lavas and breccias of predominantly alkali andesite, rhyodacite and mafic quartz latite. The approximately 40,000 km^3 of magma erupted during this phase represents about two-thirds of the volume of the entire uneroded volcanic field. The peak of this period of activity was between 35 and 30 m.y. ago.

About 30 m.y. ago, the character of the volcanism changed to voluminous ash-flow eruptions. During the interval from 30 to 22 m.y., eruption of at least 18 major quartz latitic and low-silica rhyolitic ash-flow sheets took place (Steven and Lipman, 1976), the accompanying subsidence resulting in caldera formation at the sources. Steven and Lipman (1976) identified 15 calderas (fig. 2) and postulated the presence of three others in the San Juan volcanic field. The entire ash-flow sequence in the immediate vicinity of Creede appears to span less than 2 million years, from 28 to 26 m.y. (Steven and others, 1967).

---

and Steven and Lipman (1976). The following has been summarized from these sources.

Figure 2. Calderas of the San Juan volcanic field: S, Silverton; CP, Cochetopa Park; Bz, Bonanza; LG, La Garita; SL, San Luis, B, Bachelor; C, Creede; MH, Mount Hope; P, Platoro; SM, Summitville; L, Lost Lake; U, Ute Creek; SJ, San Juan; UN, Uncompahgre; M, general location of the Mammoth Mountain caldera. From Steven and Eaton (1975).

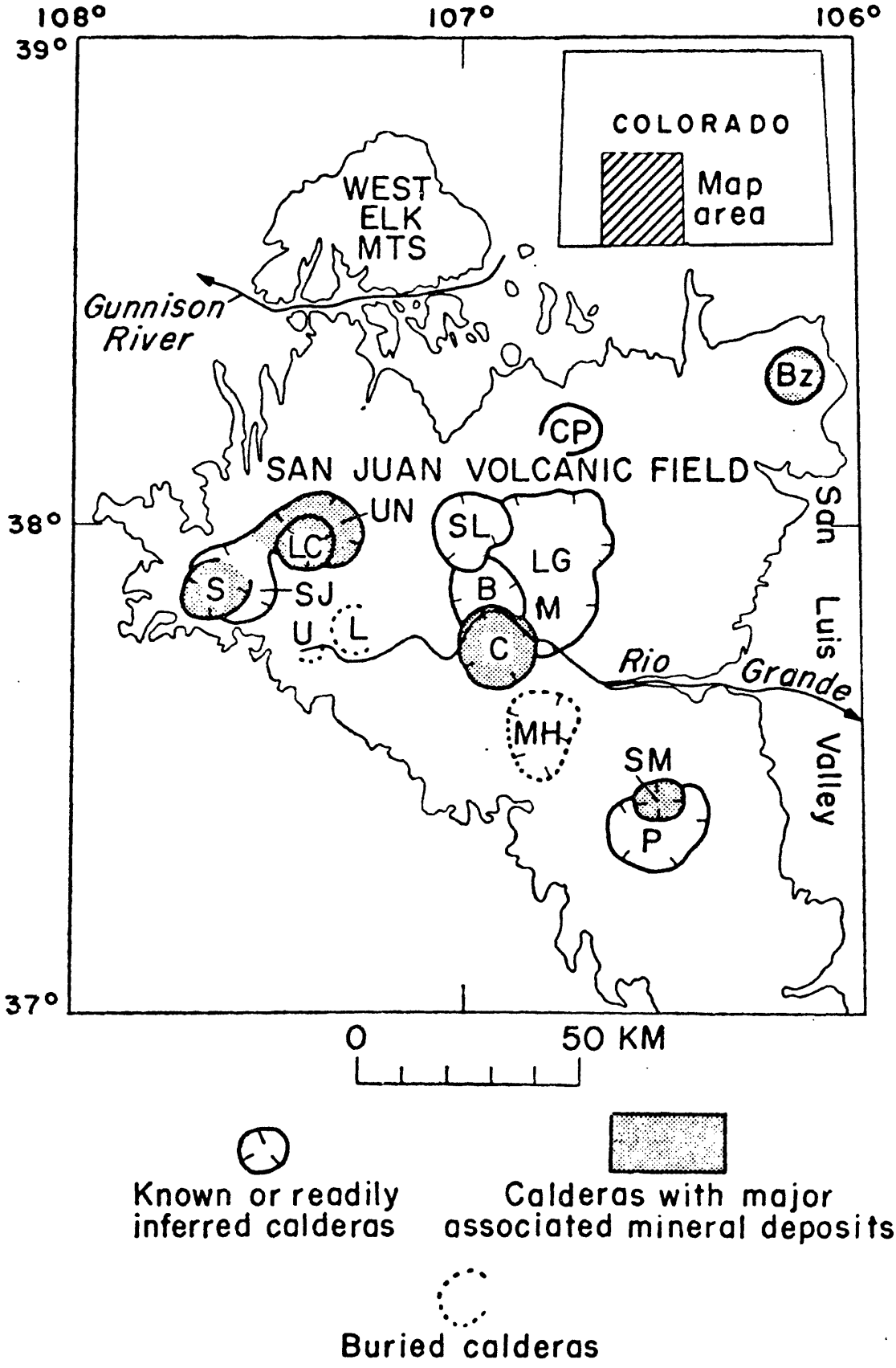
108°
107°
106°
39°
38°
37°
COLORADO
Map area
WEST ELK MTS
Gunnison River
Bz
CP
SAN JUAN VOLCANIC FIELD
UN
LC
S
SJ
U
L
SL
LG
B
M
C
MH
SM
P
Rio Grande
San Luis Valley
0
50 KM
Known or readily inferred calderas
Calderas with major associated mineral deposits
Buried calderas

A drastic petrologic change in the character of the volcanism took place 25 to 23 m.y. ago. The new volcanic activity produced bimodal assemblages of alkali olivine basalt and silicic alkali rhyolite. These younger volcanic rocks are included in the Hinsdale Formation and are volumetrically insignificant compared to the volcanics erupted between 40 and 26 m.y. ago. The change to the bimodal basalt-rhyolite volcanics roughly coincides with the structural development of the Rio Grande rift depression which bounds the eastern edge of the San Juan volcanic remnant. Its timing also corresponds to that of the initial intersection of the East Pacific Rise with the west coast of North America which caused similar petrologic changes in the character of Cenozoic volcanism over much of the western interior United States (Lipman and others, 1970). A change in direction of motion of the Pacific plate also occurred at this time.

Geology of the Creede District

The Creede mining district is located within a nested cluster of at least five calderas (fig. 3) belonging to the silicic ash-flow stage of volcanism. Table 1 shows the major ash-flow units in the district and the known corresponding source areas. Silicic to intermediate lava flows and breccias occur locally between the ash-flow units. The Fisher quartz latite lava flows and breccias, which overlie the ash-flow tuffs in this area, represent the end of the voluminous ash-flow phase in the central San Juan Mountains (Lipman and others, 1970) and partially fill the marginal moat around the resurgent dome in the Creede caldera. The Creede Formation, composed of stream, lake, and pyroclastic deposits and travertine, intertongues with the Fisher quartz latite and fills the remainder of the moat.

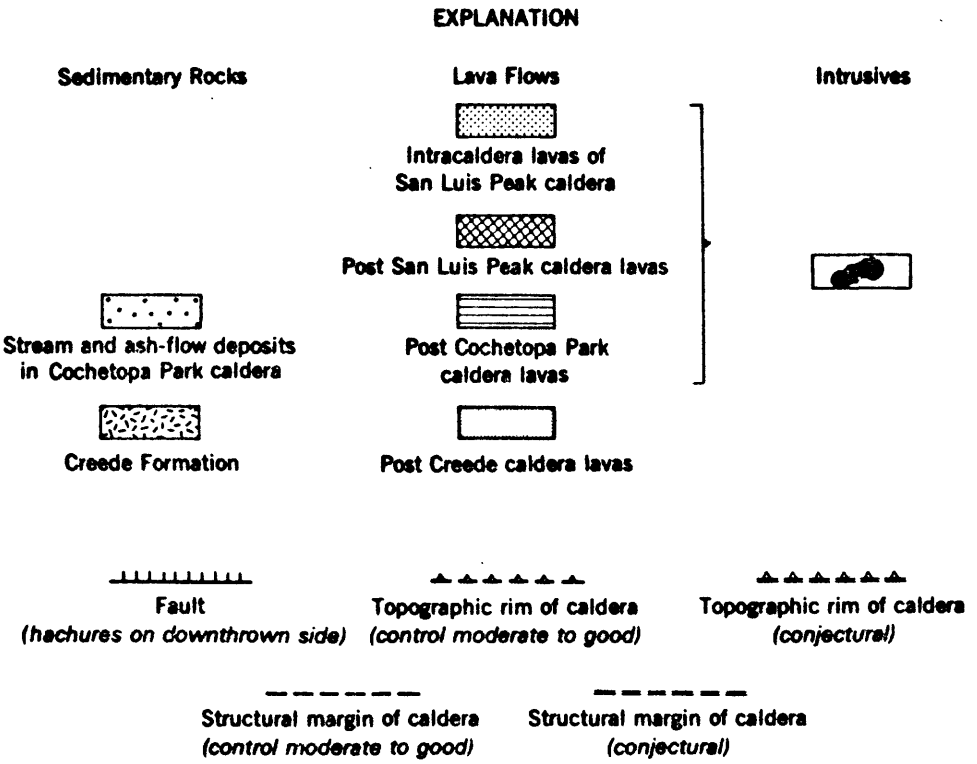

Figure 3. Spatial relations of the Creede, San Luis, and Cochetopa Park calderas and of the remnants of the Bachelor and La Garita calderas. E, general location of the Equity mine. Box shows area of figure 4. Compiled from figures 21 and 22 of Steven and Lipman (1976).

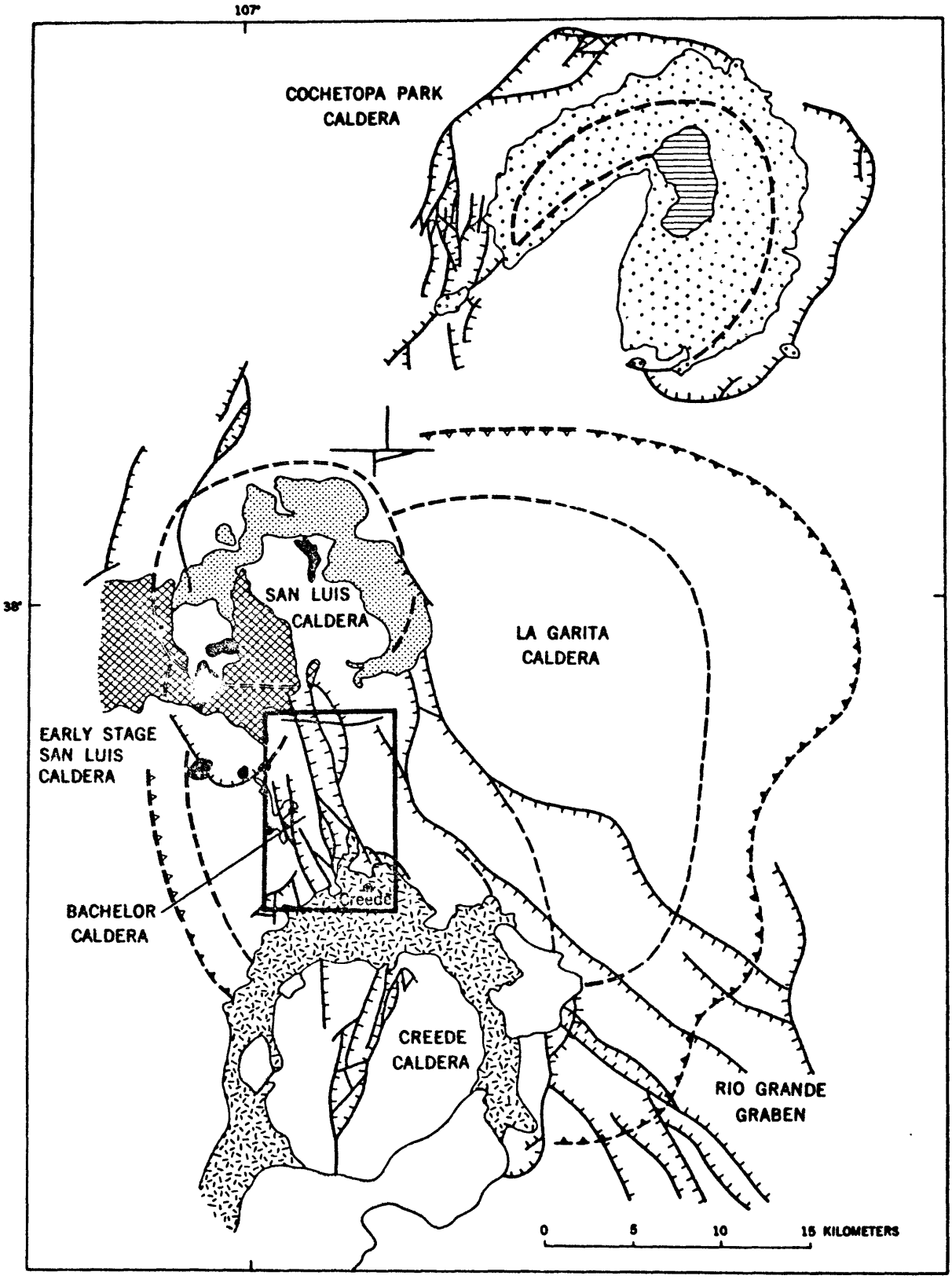
107°
38°
COCHETOPA PARK
CALDERA
SAN LUIS
CALDERA
LA GARITA
CALDERA
EARLY STAGE
SAN LUIS
CALDERA
BACHELOR
CALDERA
Creede
CREEDE
CALDERA
RIO GRANDE
GRABEN
0
5
10
15 KILOMETERS

TABLE 1. Calderas and related ash-flow units in the vicinity of the Creede District.

Compiled from Steven and Lipman (1976) and Steven and Eaton (1975).

decreasing age ▲

CALDERA	AGE (m.y.)	RELATED ASH FLOW UNIT	COMPOSITION
Creede	26.5	Snowshoe Mountain Tuff	Phenocryst-rich quartz latite
Cochetopa Park	>26.4 <26.7	Cochetopa Park Tuff	Zoned rhyolite to quartz latite
San Luis	>26.4 <26.7	Nelson Mountain Tuff	Phenocryst-rich quartz latite
		Rat Creek Tuff	Poorly welded phenocryst-poor rhyolite to densely welded phenocryst rich quartz latite
?? Wason Park ??[1]	>26.4 <26.7	Wason Park Tuff	Phenocryst-rich rhyolite
? Mammoth Mountain?[2]	26.7	Mammoth Mountain Tuff	Phenocryst-poor rhyolite to phenocryst-rich quartz latite
Bachelor	>26.7 <27.8	Carpenter Ridge Tuff Intracaldera member: Bachelor Mountain member	Phenocryst-poor rhyolite
La Garita	27.8	Fish Canyon Tuff Intracaldera member: La Garita member	Phenocryst-rich quartz latite

[1] Possibly under Creede caldera, but no caldera exposed

[2] Some indirect evidence; if existed, probably destroyed by Creede caldera

The mineralization is associated with a set of fractures (fig. 4) which form a graben (fig. 5). These fractures trend north-northwest from the northern margin of the Creede caldera. The mineralized fractures, which are younger than the Creede Formation, appear to have been localized in part along earlier fractures (fig. 4). These earlier fractures represent the keystone graben initially formed during the resurgent doming of the Bachelor caldera, the second oldest subsidence structure in the district. Silicified breccia fills the ancestral Amethyst fractures.

Steven and Ratté (1960) have shown that mineralization took place during the last major episode of movement along the graben. K-Ar dating of vein adualaria and sericite from altered wallrock indicates an age of mineralization of 24.6 ± 0.3 m.y. (Bethke and others, 1976). It has been suggested (Steven and Eaton, 1975) that the force necessary to reactivate the faults and to create the circulating hydrothermal system came from a small, still unexposed, pluton intruded below the district.

It is uncertain whether the mineralization is related to the terminal stages of the Creede caldera cycle. The youngest igneous rocks exposed in the district, the Fisher quartz latite, represent the final activity from the Creede caldera and are 26.4 ± 0.6 m.y. in age, 1.8 ± 0.9 m.y. older than the mineralization. Bethke and others (1976), therefore, suggested that the mineralization could be related either to a very late intrusion in the Fisher period of activity or to an early intrusion of the younger bimodal volcanic rocks of the Hinsdale Formation. Although mineralization can, in many cases, be related to the terminal stages of caldera evolution (Smith and Bailey, 1968), mineralization is associated with less than half the calderas of the San Juan Mountains (Lipman and others, 1976). Lipman and others (1976) suggested that the calderas provided only the structural

Figure 4. General geology of the Creede mining district. From Steven and Eaton (1975).

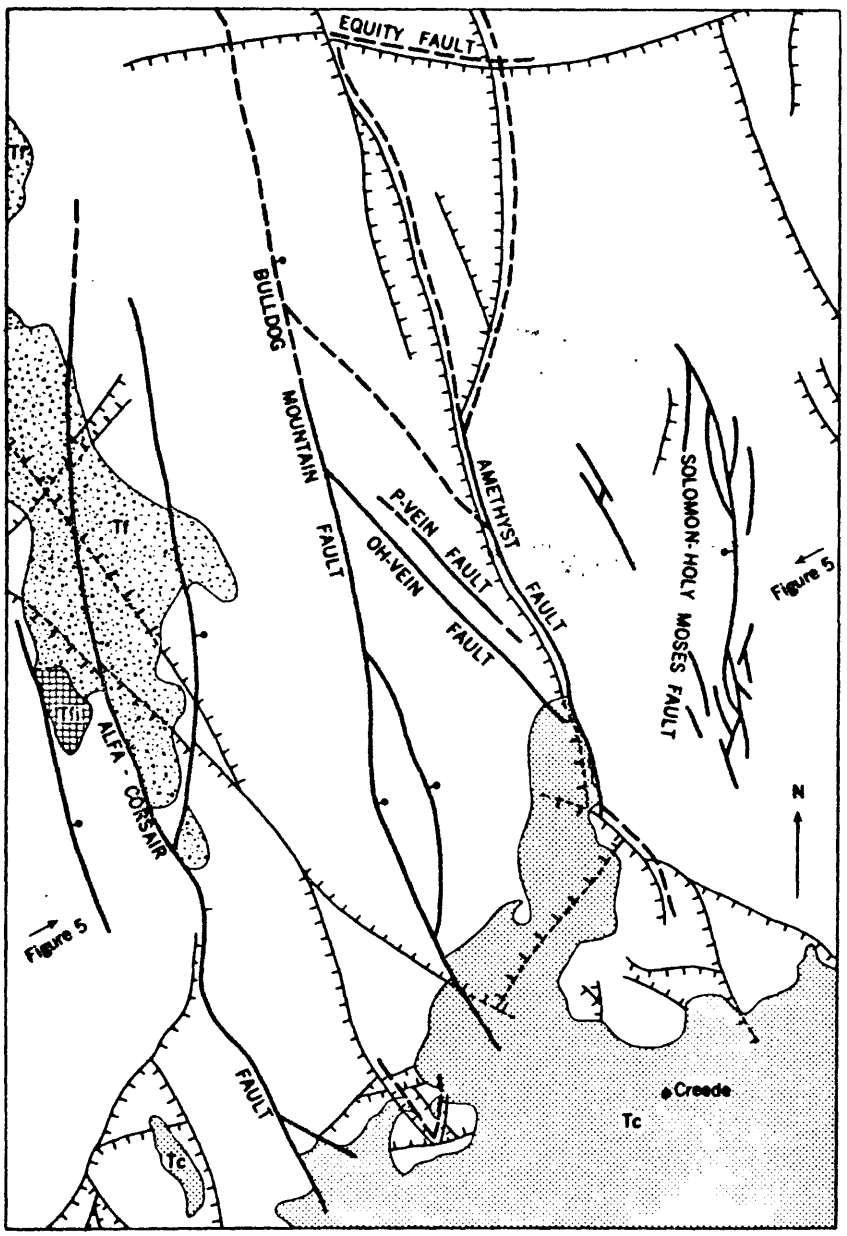

EXPLANATION

Older undifferentiated ash flow tuffs

Tf Tfi

Fisher Quartz Latite

Tf, *Quartz latite flow*

Tfi, *Volcanic neck*

Tc

Creede Formation

Geologic contact

Fault active just before and during mineralization

Dashed where uncertain or minor. Bar and ball on downthrown side

Older fault

Dotted where buried. Hachures on downthrown side

Approximate position of the generalized section shown on the figure indicated

0 1 2 KILOMETERS

Figure 5. Idealized cross section across the Creede mining district. From Steven and Eaton (1975).

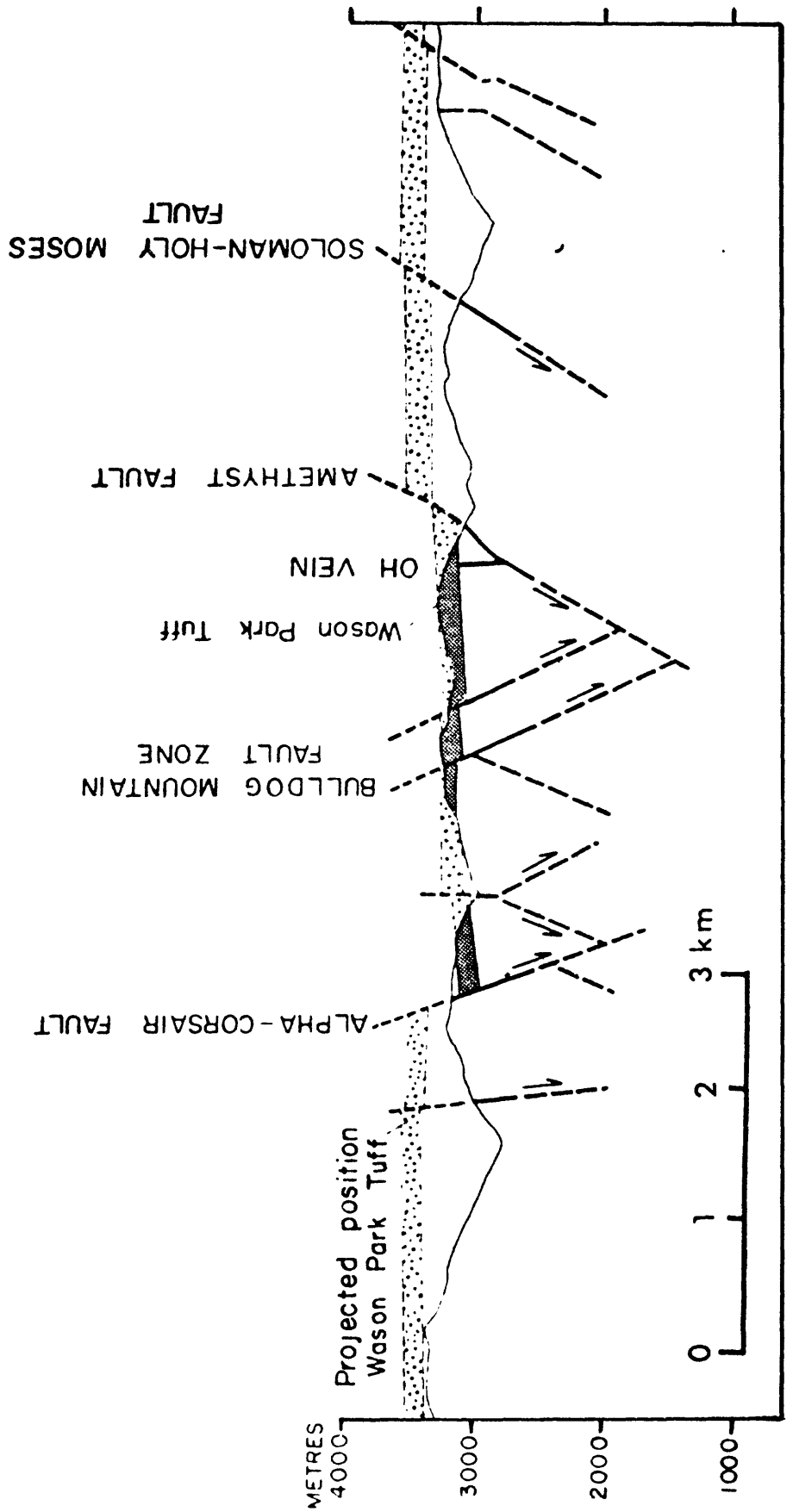
METRES
4000
3000
2000
1000
0
1
2
3 km
Projected position
Wason Park Tuff
ALPHA-CORSAIR FAULT
BULLDOG MOUNTAIN
FAULT ZONE
Wason Park Tuff
OH VEIN
AMETHYST FAULT
SOLOMAN-HOLY MOSES
FAULT

controls for the implacement of later intrusions and the plumbing system for the hydrothermal fluids.

The Creede ores occur as open-space fillings in veins cutting the devitrified welded tuffs of the Bachelor Mountain Member of the Carpenter Ridge Formation (table 1). This member is the intra-caldera accumulation of ash flows erupted within the Bachelor caldera. Three units of thick pumiceous material of quartz latitic to rhyolitic composition, the Willow Creek (0-610 m.), the Campbell Mountain (0-340 m.) and the Windy Gulch (0-275 m) make up the member. The absence of significant partings suggests that the Bachelor Mountain Member is a simple cooling unit (Smith, 1960; Steven and Ratté, 1965). The upward changes in textures of the three units into which the member is divided illustrate the classes of zonal variations in welded ash flows as described by Smith (1960). The fundamental upward zonation is from a densely welded zone through a particularly welded zone to an unwelded zone (fig. 6). The lower Willow Creek unit is a blue-to-grey, densely welded, fluidal tuff in which eutaxitic structures are developed in the upper parts. The Campbell Mountain unit is a purple-to-red, eutaxitic-to-vitroclastic, compactly welded tuff containing 5% or more foreign lithic fragments (versus 1 to 2 percent in the Willow Creek unit). The upper unit, the Windy Gulch, is a soft, poorly welded to unwelded tuff with a characteristic vitroclastic texture. The ore is found almost exclusively in the hard, massive Campbell Mountain unit. This spatial restriction is more likely due to the unit's structural competancy and favorable site in the zone where boiling took place during mineralization than due to chemical factors.

Prior to mineralization, the Bachelor Mountain Member underwent extensive potassium metasomatism. The rock was enriched in K_2O, from an

Figure 6. Schematic section of the Bachelor Mountain member of the Carpenter Ridge Formation showing the lithologic facies changes. From Ratté and Steven (1967).

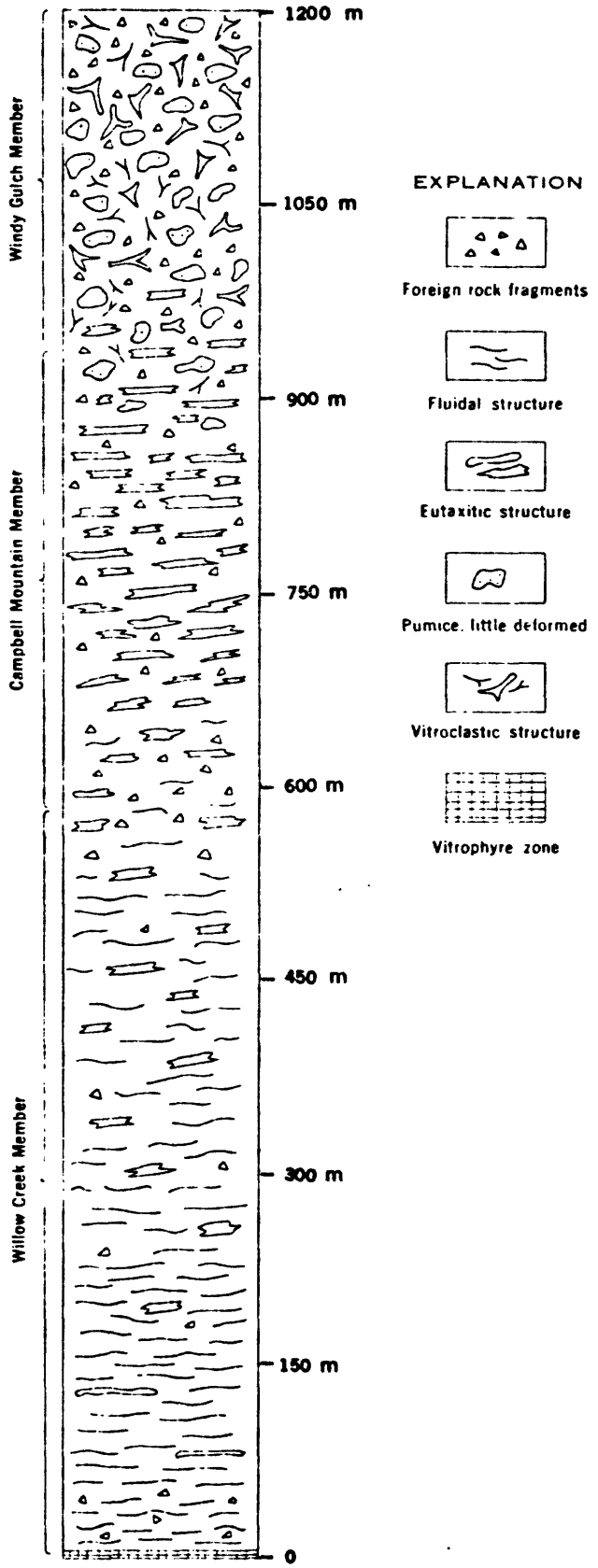
1200 m
1050 m
900 m
750 m
600 m
450 m
300 m
150 m
0
Windy Gulch Member
Campbell Mountain Member
Willow Creek Member
EXPLANATION
Foreign rock fragments
Fluidal structure
Eutaxitic structure
Pumice, little deformed
Vitroclastic structure
Vitrophyre zone

original 5 ± 1 weight percent, up to 11.35 weight percent (Ratté and Steven, 1967) and was depleted in Na_2O, CaO, MgO and total iron. The metasomatism probably took place during the cooling and devitrification of the Bachelor Mountain Member or during the resurgence of the Bachelor caldera, because the units above it show no evidence of potassium enrichment. A separate study within the program on the environment of ore deposition at Creede is currently underway to evaluate the areal extent of and the zonal variations within the potassium-enriched tuffs. Preliminary results show no significant changes in the K_2O/Na_2O ratios which can be correlated with distance from either the mineralized structures or the earlier fractures filled with silicified breccia.

Zones of intense sericitic alteration overlie some of the veins and mark the upper limits of mining. The boundaries of these alteration caps do not correspond to any primary lithologic changes in the wallrock. Except for some quartz, the alteration caps are made up of almost pure sericite. X-ray diffraction profiles show that the "sericite" is a 1M illite containing 10 to 25 percent interlayered smectite.

Alteration associated with the veins themselves, on the other hand, is not prominent. Extensive dusting of sericite in the potassium feldspar has been noted near veins. Local silicification of wallrock adjacent to veins is also common; Cannaday (1950) observed widespread silicification along the southern quarter of the OH vein. Chloritization of pumice fragments has taken place in the northern portions of the district. However, the bulk of the chlorite is in the veins, which may or may not be related to the chlorite in the altered wallrock. The chlorites will be the focus of another study in the near future.

Mineralization

Almost all of the Ag-Pb-Zn-Cu mineralization in the Creede district is contained within four major steeply-dipping fault zones which define the reactivated graben of the Bachelor caldera. These fault zones are the east-dipping Alpha-Corsair and Bulldog Mountain faults, and the west-dipping Amethyst and Solomon-Holy Moses faults (figs. 4 and 5). This study is restricted primarily to the central downdropped fault block comprising the Bulldog, Amethyst, OH and P veins. Most of the metal production in the district has come from these four veins.

The main ore minerals mined in the Creede district are native silver, sphalerite, galena, chalcopyrite, and tetrahedrite-tennantite. The silver is found in its native state, in galena, in the tetrahedrite-tennantite series and in other sulfosalts. Gangue minerals include: 1) quartz (much of which is amethystine), 2) chlorite, 3) pyrite, 4) barite, 5) sericite, 6) carbonate, 7) hematite, 8) fluorite and 9) adularia. Barite, carbonate and native silver are more abundant in the southern part of the district (southern Amethyst and Bulldog veins) whereas chlorite and hematite are more abundant in the northern parts (OH, P and northern Amethyst veins). Although most of the northern two-thirds of the Amethyst vein is almost completely inaccessible, the mineralogy described by Emmons and Larsen (1923) appears to have been very similar to that along the OH vein.

The early bonanza ores were composed mainly of native silver and silver chlorides and of $PbCO_3$ (with some $PbSO_4$) containing high-silver values. Most of the production of these ores came from the zone of supergene enrichment along the Amethyst vein. This zone of secondary enrichment extended either from the surface or from the base of a leached cap (which

was up to 150 m. deep) to a depth of about 240 m. (Meeves and Darnell, 1968) and dipped steeply to the south.

Barton and others (1977) proposed an ore deposition model based on fluid inclusion data and on geochemical considerations of the mineral associations, mineral deposition sequence and the varying iron contents in the sphalerite. They postulated a freely recirculating hydrothermal system (fig. 7), in direct contrast to the classical "once-through-and-out" model. Hot, metal-rich, ore fluid is thought to have ascended in the north and flowed south forming the top of a convecting cell and depositing (and sometimes leaching near the input area) gangue and ore minerals. Steven and Eaton (1975) suggest that movement upward was inhibited by the soft, impermeable Windy Gulch tuff and the Rat Creek tuff. Cooling of the fluids, due to boiling and to heat conduction into the overlying cooler rocks, and a small pH rise associated with the boiling off of acid components (H_2S and CO_2) contributed to the precipitation of ore. Condensation of the acid volatiles in the overlying unbuffered waters resulted in the forming of a sericitic capping. Redox reactions during deposition were governed by an iron-rich chlorite + pyrite (or hematite) + quartz (+ water) buffer. The progressively cooler and more mineral-depleted ore fluids continued to flow south until they either cooled enough to convect downward or encountered the structural margin of the Creede caldera. Some of the ore fluids leaked out into the Creede Formation, which is now being actively explored for commercial ore bodies. The waters were subsequently reheated at depth where they extracted metals and sulfur from whatever sources were available and eventually rose again in the north. This model is consistent with isotopic evidence which indicates that the ore-forming fluids were predominantly recirculated meteoric water.

Figure 7. Schematic hydrologic model for ore deposition in the Creede mining district. Cross-hatched pattern denotes the OH-Amethyst ore zone. Solid arrows represent depositing solutions and open arrows show undersaturated solutions; arrows with an 'X' indicate meteoric water recharge and stippled arrows indicate recharge at depth. From Barton and others (1977).

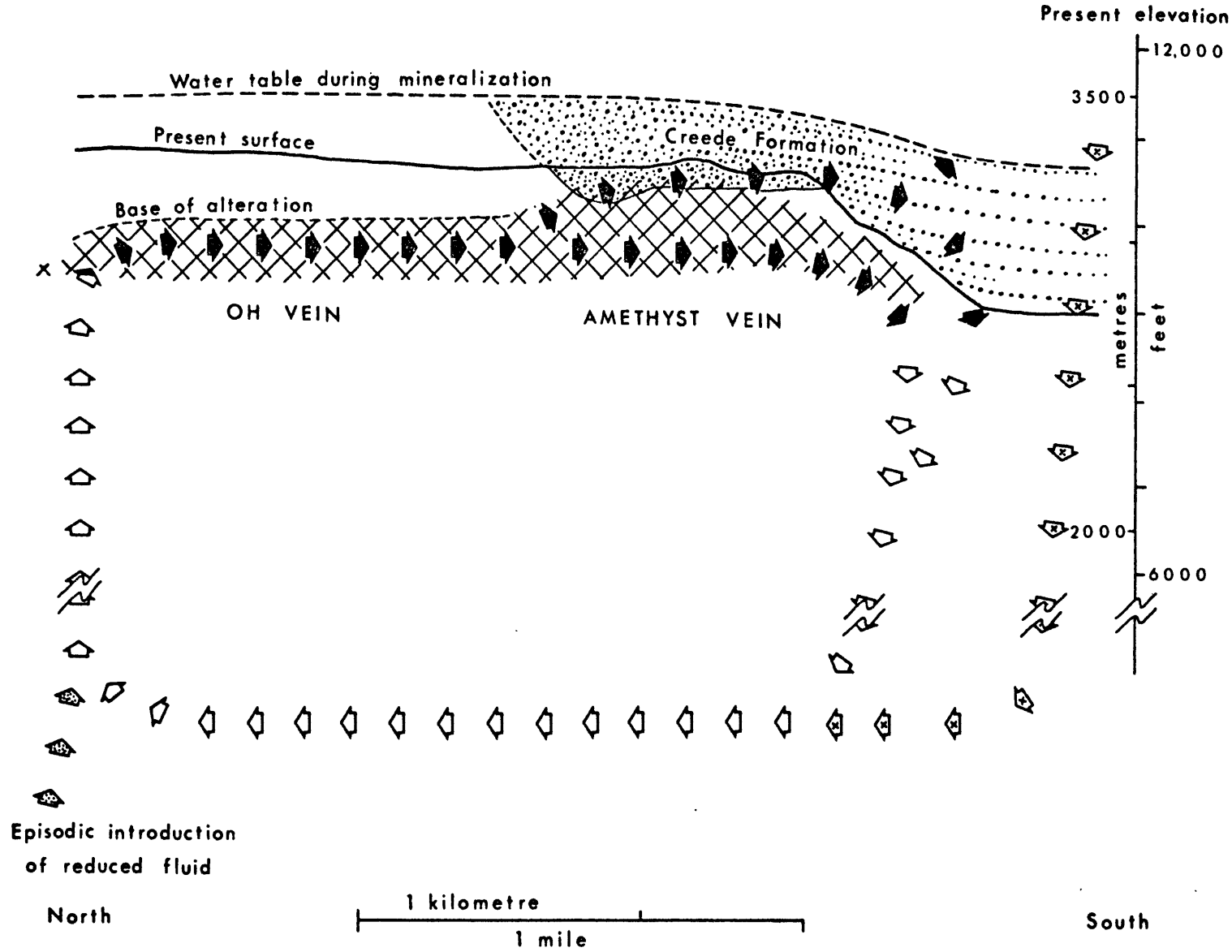
Present elevation
12,000
3500
Water table during mineralization
Present surface
Creede Formation
Base of alteration
OH VEIN
AMETHYST VEIN
metres
feet
2000
6000
Episodic introduction
of reduced fluid
North
1 kilometre
1 mile
South

III. CARBONATE MINERALOGY AND GEOCHEMISTRY

Statement of Study

This study of the mineralogy and compositional range of the carbonates in the Creede district was undertaken in an attempt to add to the documentation of the vein-filling history at Creede and of the geochemical conditions that existed during mineralization. A preliminary "ore stratigraphy" has already been established on the basis of iron-rich growth bands within the sphalerite (Bethke and Barton, 1971). It was hoped that the carbonates, which occupy two very distinctive positions within this "ore stratigraphy" would, like the sphalerite, show a detailed evolution and would provide some answers as to how and why conditions twice changed to allow carbonate precipitation to replace sulfide precipitation.

In important respects, this carbonate study makes use of and contributes to other ongoing Creede studies. The isotopic compositions of the carbonates were determined as part of a more encompassing isotopic study. The temperature of ore deposition of 250°C used in this paper was determined during a preliminary fluid inclusion study (Roedder, 1965). Data on the mineralogical character of the sericitic alteration overlying some of the veins was gathered as part of a broader study of the vein and wallrock alteration at Creede. The carbonate study should, in turn, improve the data base into which future studies at Creede can be integrated.

Procedures

Carbonate samples from forty-four localities from five vein systems in

Creede district have been examined using various approaches. The primary means of gathering data for this study has been the electron microprobe. Other techniques such as electron microscopy, x-ray diffraction, cathodoluminescence, and semi-quantitative spectrographic analyses have been used to supplement the microprobe data.

Some samples were collected by the author during two field seasons totalling 5 weeks in 1975 and 1976. Other samples analyzed by the author came from the collections made by P. M. Bethke, P. B. Barton, Jr., E. Roedder, T. Nash, D. Hull and J. L. Haas. These collections consist of over 500 sample localities represented by more than two metric tons of specimens.

Eighty-eight doubly polished thin sections of the carbonate localities were prepared by the author for microprobe analysis. The downside of each section was ground flat using metal-bonded diamond grinding discs mounted on a Sampson Polishing Machine (model SP-1). A sequence employing three grinding discs imbedded with 30μ, 15μ and 6μ size diamonds was followed; the lubricant was water. The more fragile specimens were impregnated with epoxy prior to grinding. The three grinding stages were followed by three polishing stages, using a sequence of 15μ, 6μ and 1μ size of diamond as a paste or spray on cloth polishing discs (Metcloth for 15μ and 6μ; Texmet for 1μ). Water again was the lubricant. Between each polishing stage, the specimen was washed in an ultrasonic cleaner. The specimen was then mounted, polished-side down, on a 1 x 1-3/4 inch microscope slide with Buelher No. 20-8130 AB epoxy. When the epoxy had cured, the specimen was cut to about 1 mm thickness and thinned by grinding using a Hillquist thin section machine. The second side was then ground and polished in the same manner as the down side. The finished products were from 30μ to 100μ thick.

The specimens were subsequently examined in detail under the microscope, and sites to probe were chosen and photographed at 100X magnification, which approximates the high-power magnification on the electron microprobe used. Sites were chosen for analysis based on color variation in transmitted light, microscopic and macroscopic textural variations, and mineral associations. The typically pitted surfaces (probably due to the opening up of abundant fluid inclusions during the polishing procedure) frequently made site selection difficult.

Subsequent to photographic documentation, the thin sections were given a light carbon coating in order to eliminate charge build-up under the electron beam of the microprobe by providing a conductive path. A number of individual points within the chosen sites were then analyzed using an ARL-EMX-SM electron microprobe under the following conditions: accelerating voltage, 15 kv; beam current, 0.05 A; beam diameter, 2-3 m; and preset time and count limits, 20 seconds or 20,000 counts. Raw counts were collected by the Krisel control system and corrected for beam current drift and for dead time. Parameters from the previously analyzed standards were used to calculate metal compositions which were subsequently corrected for matrix effects using the Bence-Albee correction scheme (Bence and Albee, 1968; Albee and Ray, 1970). The analyses are given in the form of weight percent oxides and of mole percent carbonates.

Iron and manganese contents were analyzed with a lithium fluoride (LIF) crystal, magnesium with a rubidium acid phthalate (RAP) crystal; calcium was analyzed first with an LIF crystal and then with a pentaerythritol (PET) crystal. Due to the restriction of three spectrometers, iron, magnesium and calcium were analyzed simultaneously, followed by analysis of the manganese content. Several other elements, such as Zn and Pb, are present in

the carbonates in small amounts, frequently too small to be analyzed by electron microprobe, and will be discussed later. Of the standards used (table 2), the siderite (for iron) and the dolomite (for calcium and magnesium) were obtained from the U.S. National Museum of Natural History (Smithsonian Institution). J. S. Huebner donated the rhodochrosite standard (used for Mn). Repeated microprobe analyses on the grains were made to check for homogeneity.

The accuracy of the microprobe analyses of the Creede unknowns is dependent on the quality of the wet chemistry of the standards. The degree of agreement among replicate analyses (precision) of the standards was calculated in order to evaluate the total effect of the many possible sources of error inherent in electron microprobe analyses (i.e., statistical counting errors, instrumental errors, operational errors and specimen errors (Bertin, 1971)). Thirty-seven analyses of standards gathered on eight days over a period of two years were examined. Relative precisions (standard deviation divided by the mean) for the element used as the standard in analyzing itself are Ca 1.82%, Mg 2.23%, Mn 1.52% and Fe 1.89% of the amount present. Therefore, the error for most analyses should be within approximately 2 percent of the amount present. Relative precision is worse when there is only a small amount (i.e., less than a few mole percent) of the element present. Nevertheless, values down to 0.3 mole percent do denote the presence of an element, although the value itself is more and more of a rough estimate with decreasing amounts present.

The values for precision in the preceding paragraph are fairly encouraging, especially because several analytical problems (with respect to electron microprobe analysis) are inherent in the carbonates. In the first place, it is not possible, using the present microprobe, to analyze

TABLE 2. Composition of standards used for electron microprobe analyses.

	DOLOMITE[1] (Austria)	SIDERITE[2] (Broken Hill, NSW, Australia)	RHODOCHROSITE (Alma Rock, New Mexico)
CaO	29.71	nd.	0.0
MgO	20.97	nd.	0.04
FeO	0.66	57.33	0.30
MnO	0.03	4.66	61.11
CO_2	46.64	38.01	38.50
	98.01	100.00	99.95
$CaCO_3$	53.02	nd.	0.0
$MgCO_3$	43.87	nd.	0.08
$FeCO_3$	1.06	92.45	0.48
$MnCO_3$	0.05	7.55	99.02
	98.00	100.00	99.58[4]

[1]As reported by Reddick (1968). U.S. National Museum of Natural History (Smithsonian Institution) No. R10057.

[2]Analysis by S. Spooner (personal communication, letter to J. White, Jr., in Smithsonian files), Georgia Institute of Technology. Only manganese content analyzed; iron and carbon dioxide contents calculated by difference. U.S. National Museum of Natural History (Smithsonian Institution) No. 93218.

[3]Analysis by J.J. Fahey, U.S. Geological Survey. U.S. National Museum of Natural History (Smithsonian Institution) No. R2478.

[4]Discrepancy in sums is due to the non-stoichiometry of the initial determination.

carbonates for carbon and oxygen so that the analyses cannot sum to 100%. There is, therefore, no automatic check on each analysis. Control on the quality of the analyses depended on frequent re-analyses of the standards to demonstrate that no drift in the standardization had taken place and on critical evaluation of the analyses of the unknown carbonate; analyses departing more than ±2% from the mean sum of several analyses of the pertinent standard were discarded. In the second place, carbon dioxide is apparently driven off from the carbonate structure when the focussed electron beam hits the carbonate. It is difficult to evaluate the effects of this process although it appears to be most detrimental to calcium-rich carbonates and is not visibly apparent in manganese-rich and iron-rich carbonates. Thirdly, the β factors used for the matrix correction had to be calculated as if the standards were oxides instead of carbonates.

In addition to the single spot analyses, the electron microprobe was used to traverse and to raster scan selected sites. The electron beam was set up to traverse, at 3 μ/sec, several of the more apparently zoned siderite crystals; uncorrected intensities of several elements were plotted automatically during the traverse. An attempt was also made to map compositional variations pictorially using the raster scanning capability of the electron microprobe to look at 80μ x 64μ areas.

Other techniques were used to complement the electron microprobe data. The scanning electron microscope was used to examine some of the carbonates. X-ray diffraction techniques using a Guinier-Haig camera helped to define the presence of one or two phases in some samples; both iron and chromium radiation were used. The degree of ordering in single crystals of the carbonate was examined using a precession camera. A luminiscope turned out not to be useful with respect to the carbonates because the iron and

manganese contents were too high to permit fluorescence; however, the technique was useful in detecting cadmium-rich sphalerite within the carbonate. Semi-quantitative spectrographic analyses were used to determine the minor and trace element contents in the carbonates.

Carbonate Mineralogy

Introduction

Carbonate minerals from forty-two localities along the four major vein systems in the Creede district have been examined. Plate I shows the distribution of localities along the four major veins in cross-section: 20 on the Bulldog vein; 4 on the Amethyst vein and 5 in hanging wall structures off the Amethyst vein; 11 on the OH vein; and 2 on the P vein. Two additional sample localities are from the Equity mine on the Equity fault (fig. 4), which trends east-west about 9.6 km. north of Creede; this mine represents the northernmost limit of production in the Creede district.

The carbonates help to define the general sequence of mineral deposition which has been established by Bethke and Barton (1971) based primarily on varying iron contents in sphalerite along the OH vein. The paragenesis can be divided into five stages: Stage A is the pre-ore rhodochrosite-barite-quartz stage; Stages B and D represent the periods of major ore deposition, being respectively finer and coarser grained and having very similar mineral associations although Stage D is lower in silver; Stage C denotes the volumetrically insignificant fluorite-siderite-quartz stage separating the two stages (B and D) of major ore deposition; Stage E denotes the post-ore gel pyrite stage. Approximate relative volumes of each stage are Stage A, 5% (of which roughly 80% is rhodochrosite); Stage B, 65%; Stage C, 0.1% (of which roughly 10% is siderite); Stage D, 30%; and Stage E,

4%. Due to the complex flow pattern of the ore-forming fluid, few localities exhibit all stages (Bethke and Barton, 1971). Along the OH vein, the ratio of early-fine Stage B to late-coarse Stage D increases southward and upward.

Rhodochrosite was deposited prior to the main phase of sulfide and barite deposition, frequently directly on wallrock, and defines Stage A. This carbonate is light to dark pink to buff in color, usually massive (fig. 8a) and less frequently rhombic (fig. 8b) in form, and not uncommonly banded (fig. 8c) or brecciated (fig. 8d) in appearance. The rhodochrosite also precipitated as individual saddle-shaped rhombs in some localities (fig. 8e). This early carbonate occurs with quartz and barite and frequently contains finely disseminated sulfide blebs or narrow bands of sulfide blebs. Much of this carbonate is fine-grained, but large, leached crystals up to 2 cm in size have been noted in several localities. Figure 8f shows a sulfide capping overlying now leached carbonate crystals which grew on massive carbonate. Figure 8g shows the remains of a large leached carbonate crystals which grew on massive carbonate. Figure 8g shows the remnants of a large carbonate crystal which has either been leached or which grew skeletally.

Siderite is limited in occurrence to Stage C and helps to define that period of deposition. This stage documents a break in major sulfide deposition between the early fine-grained stage and the late coarse-grained stage; it was preceded by extensive leaching of Stage B. The carbonate is tan to milk-chocolate brown in color and occurs either as perched rhombs (1 mm average) in vugs (fig. 8h) or as infilling in small interstitial spaces (generally less than 1 mm) in the fine-grained Stage B. It overlies light-colored sphalerite, fluorite, quartz and/or chalcopyrite and is intergrown with hematite platelets (0.05 mm diameter) in some localities.

Both the siderite and rhodochrosite generations can almost always be

Figure 8. Hand specimens of carbonates showing characteristic textures and growth features.

A) Slab of massive rhodochrosite containing disseminated sulfides. (PMB-MP)

B) Rhodochrosite rhombs on barite. (PMB-UH)

C) Banded rhodochrosite on wallrock. (PMB-FO)

D) Brecciated rhodochrosite cemented by later rhodochrosite and barite. Darker fragments are wallrock; lighter areas are rhodochrosite; white areas are barite. (PMB-HE)

Figure 8. (continued)

E) Saddle-shaped rhodochrosite rhombs. Black specks are sulfide grains. (DH-147 (Bulldog vein, location unknown)).

F) Sulfide and carbonate capping retaining crystal form of now leached rhodochrosite scalenohedrons which overlay massive rhodochrosite. (PMB-NB)

G) Outlined area is a single rhodochrosite crystal which has been etched along cleavage planes. Entire specimen is rhodochrosite. (PBB-143)

H) Siderite rhombs on coarse octahedral fluorite and dark-appearing sphalerite. (PMB-BL)

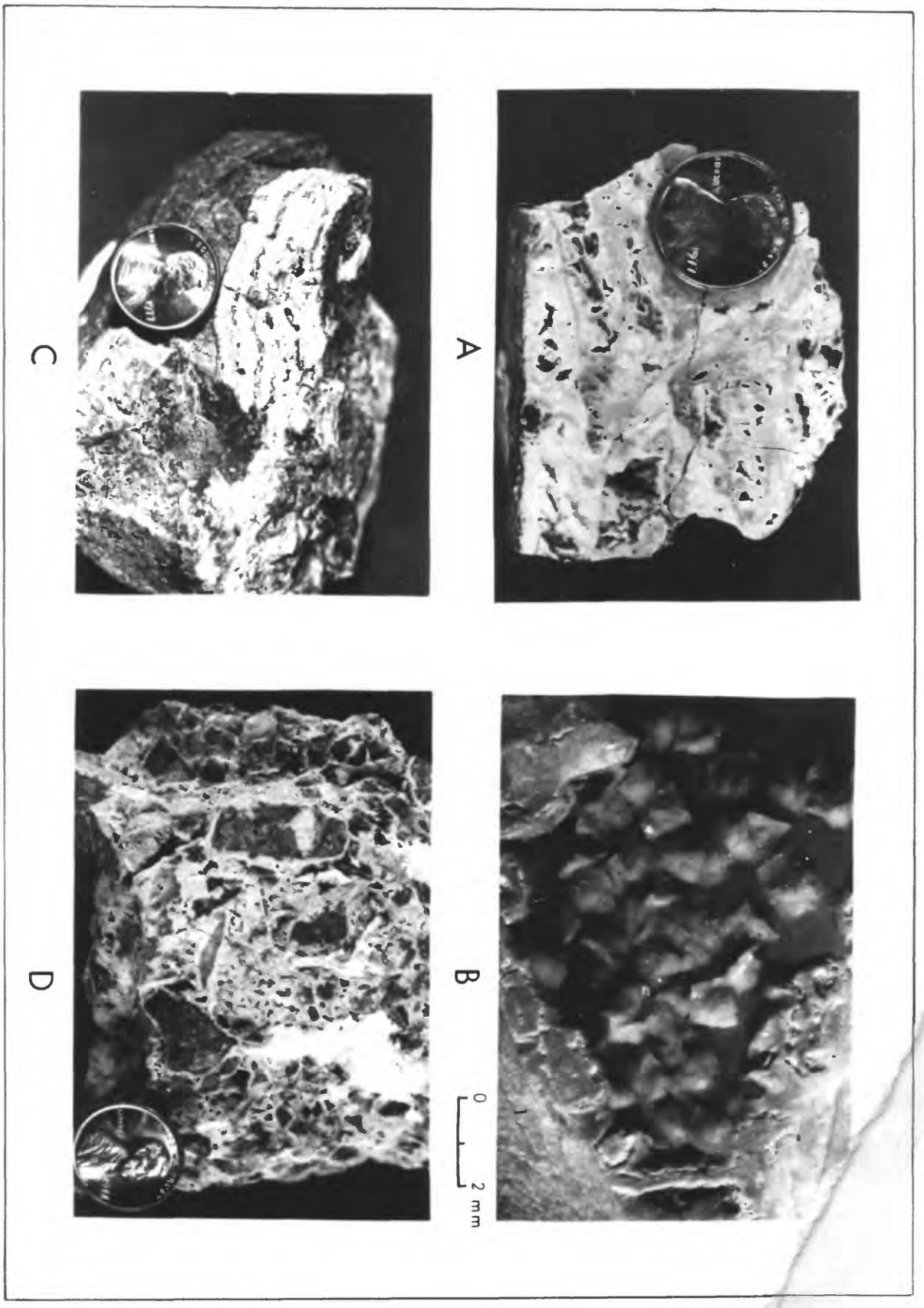
A
B
C
D
0
2 mm

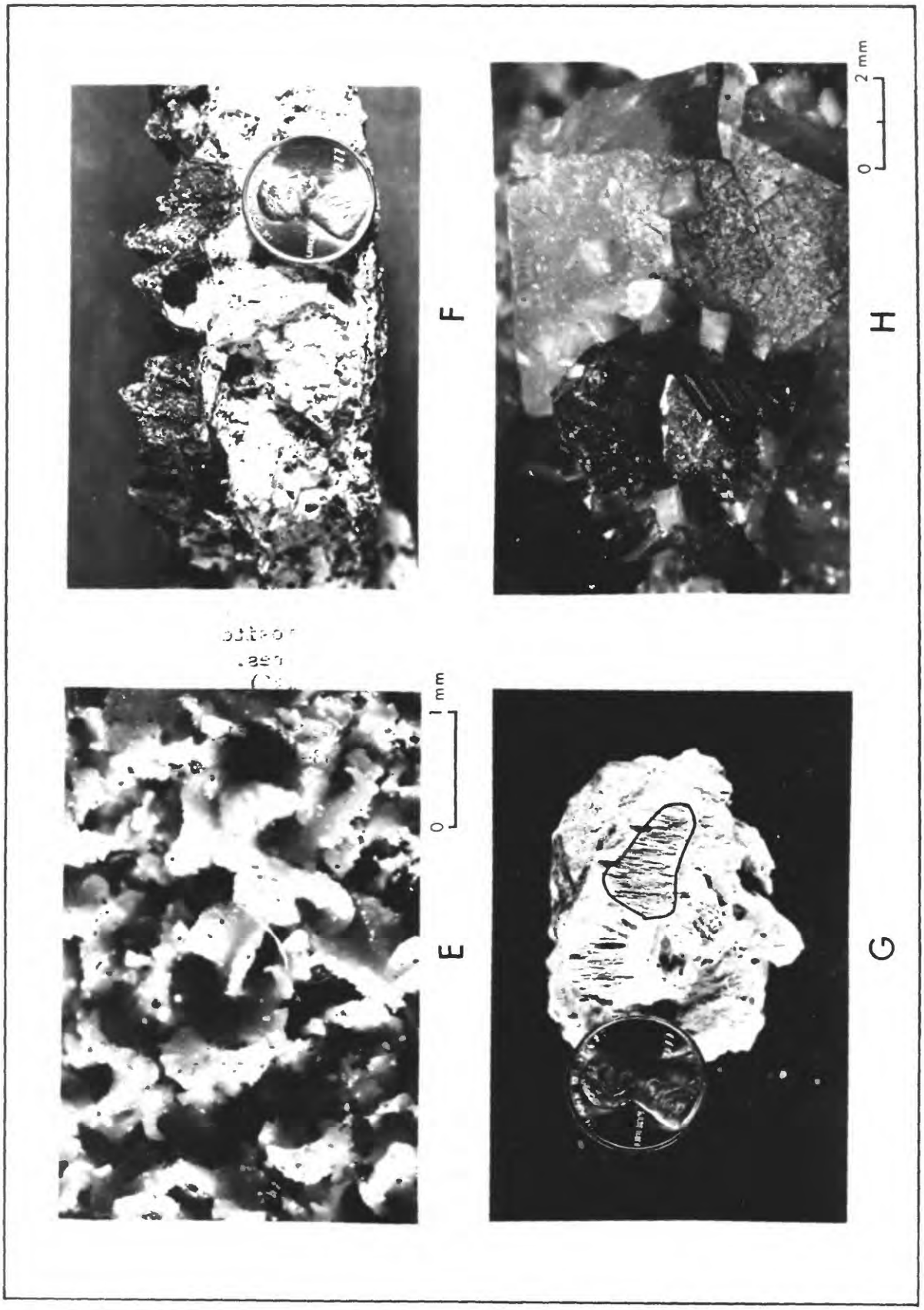
E
F
G
H
0
1 mm
0
2 mm

defined and distinguished by field criteria which include form, color, mineral associations and paragenetic position. The following discussion is based on the separation of sample localities using these criteria. No samples containing both generations have been found.

Early-Stage Carbonate (Stage A)

Electron microprobe analyses indicate that almost all of the carbonate of Stage A is rhodochrosite with a fairly limited compositional range. Figure 9 shows the microprobe analyses of the early carbonate projected onto a ternary base of $FeCO_3$-$CaCO_3$-$MnCO_3$ from the fourth apex, $MgCO_3$. In projecting from a fourth apex, the three components defining the base of the tetrahedron are used to recalculate each composition to 100% and the fourth component is ignored. All of the subsequent compositional figures have been constructed using the same procedure. In figure 9, the data are not significantly distorted by plotting them in this manner because the majority of analyses have less than 3 mole percent $MgCO_3$. Most analyses fall between 70 and 93 mole percent $MnCO_3$ but cluster predominantly in the 85 to 93 mole percent $MnCO_3$ range. Calcium contents are fairly low (generally 2.5 to 8 mole percent $CaCO_3$) with ratios of $CaCO_3$ to $MgCO_3$ usually greater than 4. No rhodochrosite was found with less than 1.4 mole percent $CaCO_3$ or less than 2.2 mole percent $FeCO_3$. A subgroup of analyses with relatively higher $CaCO_3$ contents (11 to 15 mole percent) should be noted. Atypical analyses include a few exceptionally high-calcium, low-iron compositions (all from one locality, PBB-147, which will be discussed below) and a few high-iron, low-calcium compositions.

Compositional variation within individual localities is frequently fairly limited as shown in figure 10 (a and b). The localities have been arranged from left to right going from south to north along each level for

Figure 9. Compositional range of the early-stage carbonate plotted within the system $MnCO_3$-$FeCO_3$-$CaCO_3$-$MgCO_3$ projected from the $MgCO_3$ apex.

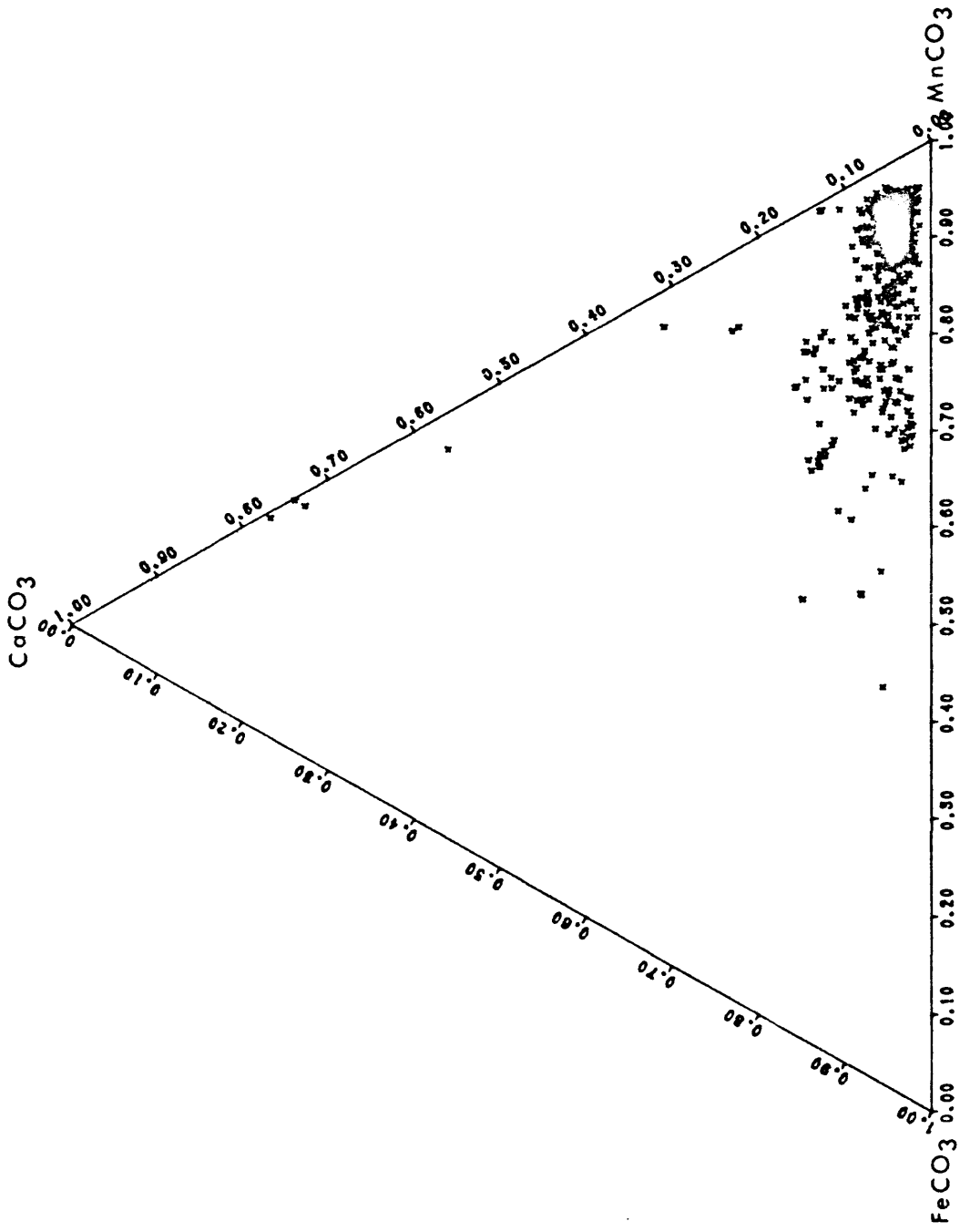
CaCO3
MnCO3
FeCO3

each vein (the highest level is in the upper left hand corner). The small compositional range in many sample localities precludes defining any relationships between distinctive growth textures and composition. However, even when the compositional range in a rhodochrosite locality is relatively broad, correlation between composition and sequence of deposition is difficult. Several of the sample localities containing the broader ranges in composition illustrate this problem; these include PBB-147, DH-23, PMB-MJ, PMB-NB, and PMB-UH (plate I and fig. 10). These localities also contain almost all of the high-calcium (typically 11 to 15 mole percent $CaCO_3$) rhodochrosite analyses.

PBB-147: Sample locality PBB-147 is unique in having several exceptionally high-calcium carbonates with $CaCO_3$ contents greater than 20 mole percent. These calcium-rich carbonates occur in barite molds which are enclosed in massive fine-grained quartz (fig. 11a). It is not possible to determine their time relationship with the low-calcium rhodochrosite which also occurs in this locality.

DH-23: Sample locality DH-23 contains only the more common relatively high-calcium (11 to 15 mole percent $CaCO_3$) rhodochrosite which occurs as rhombs growing on barite (fig. 8b). At this locality, "stratigraphic" relations show that there were at least two periods of carbonate deposition (fig. 11b, showing growth sequence $B_1R_1B_2R_2B_3$). At least one period of carbonate leaching took place. Unfortunately, it is not possible to distinguish the different carbonate growth substages compositionally except for an increase in iron content near the outer edges of the latest growth zone.

Figure 10. Compositional ranges within each sample locality of the early-stage carbonate plotted within the system $MnCO_3$-$FeCO_3$-$CaCO_3$-$MgCO_3$ projected from the $MgCO_3$ apex.

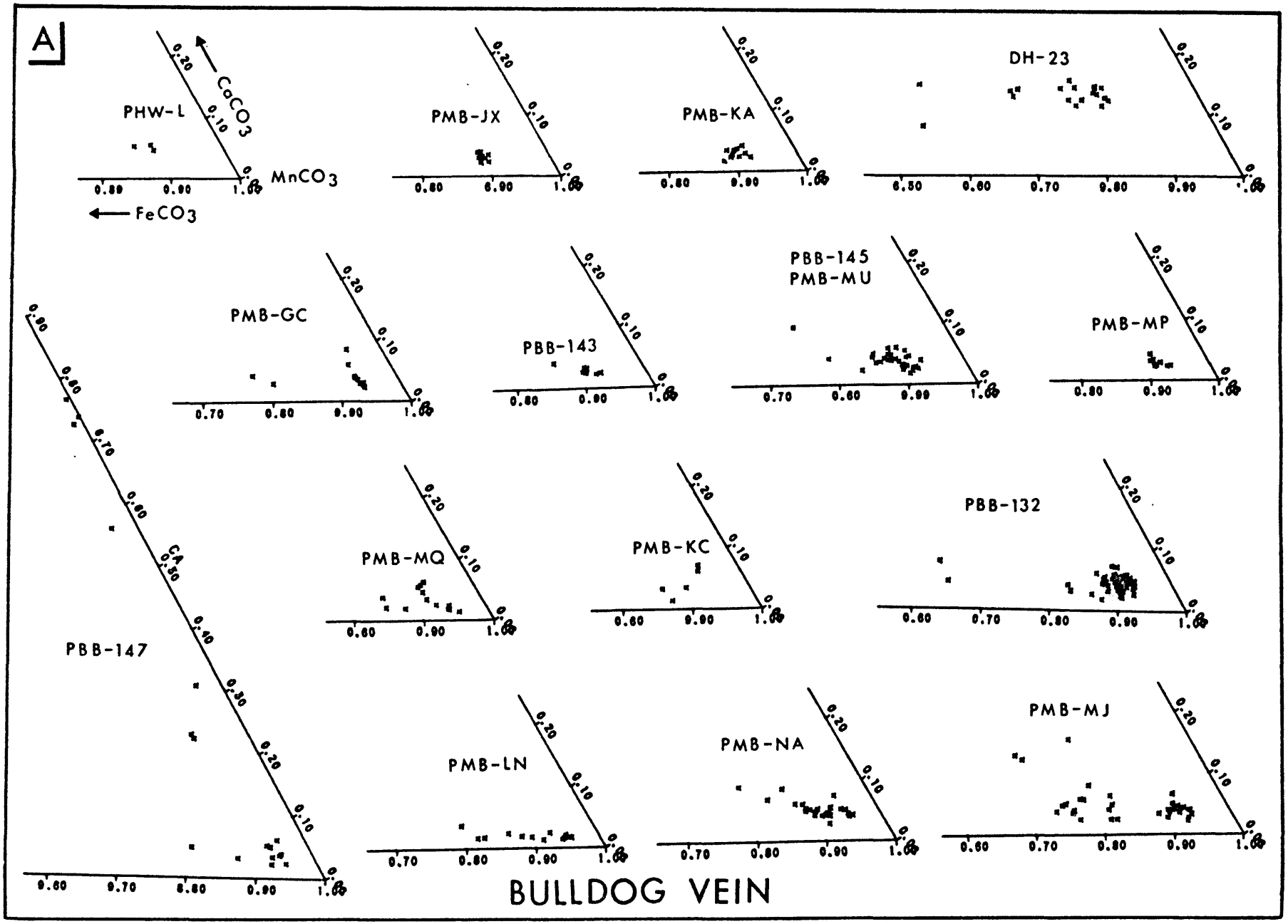
A
PHW-L
PMB-JX
PMB-KA
DH-23
PMB-GC
PBB-143
PBB-145
PMB-MU
PMB-MP
PBB-147
PMB-MQ
PMB-KC
PBB-132
PMB-LN
PMB-NA
PMB-MJ
CaCO3
MnCO3
FeCO3
BULLDOG VEIN

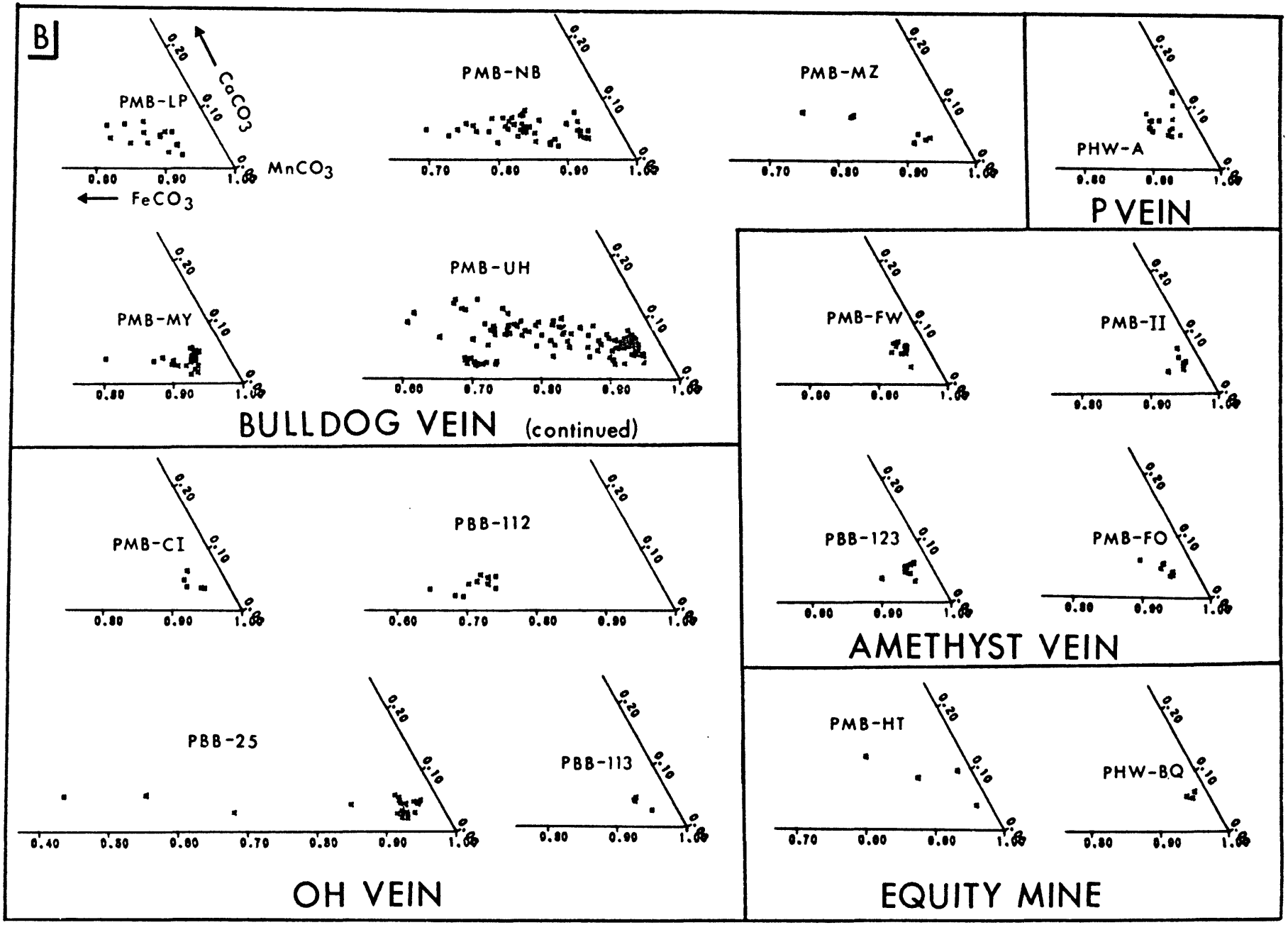
B
PMB-LP
CaCO3
MnCO3
FeCO3
PMB-NB
PMB-MZ
PHW-A
P VEIN
PMB-MY
PMB-UH
BULLDOG VEIN (continued)
PMB-FW
PMB-II
PMB-CI
PBB-112
PBB-123
PMB-FO
AMETHYST VEIN
PBB-25
PBB-113
OH VEIN
PMB-HT
PHW-BQ
EQUITY MINE

Figure 11. Photomicrographs showing textural variations of the early-stage carbonate. In transmitted light, the carbonate can appear either opaque (due to abundant fluid inclusions) or clear (due to few fluid inclusions).

A) Suggested sequence of events is 1) barite deposition; 2) quartz deposition; 3) leaching of barite; 4) deposition of carbonate in barite molds and in vugs in the quartz; 5) partial leaching of carbonate; 6) deposition of quartz which infills remaining open areas in the barite molds and elsewhere. Quartz shows ghost structure of the former barite blades. Black material is carbonate and white is quartz. (PBB-147, transmitted light)

B) Alternating deposition of rhodochrosite and barite is evident. Growth sequence of barite (B_1), rhodochrosite (R_1), barite (B_2), rhodochrosite (R_2), and barite (B_3) is shown. Material enclosing the rhodochrosite is epoxy. (DH-23, reflected light)

C) Whole thin section showing complex textural relations in the early-stage carbonate. (PMB-MJ, transmitted light, crossed nicols)

D) Sample showing at least three periods of rhodochrosite deposition (R_1, R_2, R_3) and one period of sulfide deposition (S_1). (PMB-NB, transmitted light)

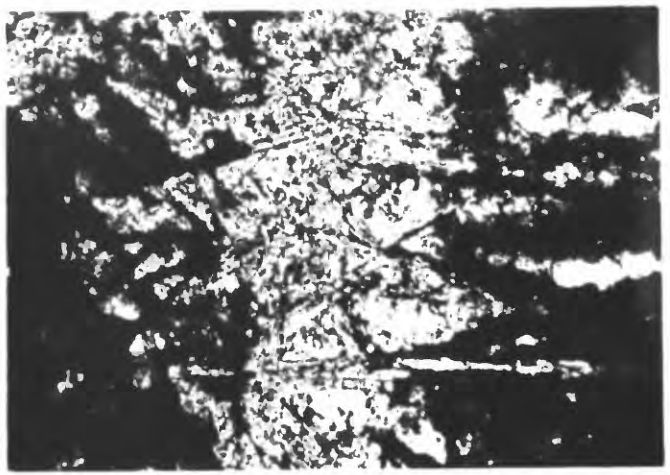

A 0 0.4 mm

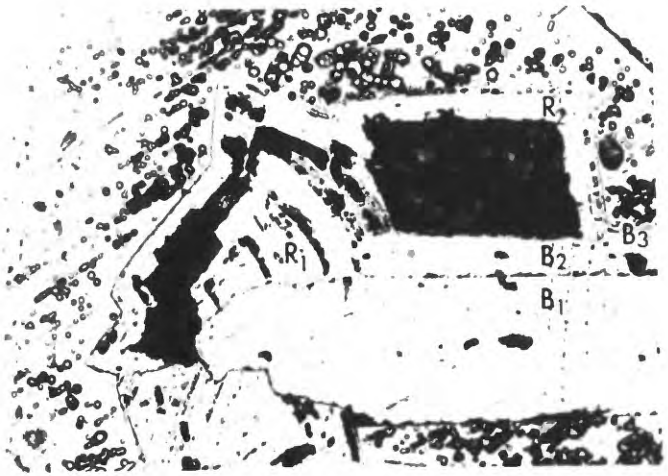

B 0 0.2 mm

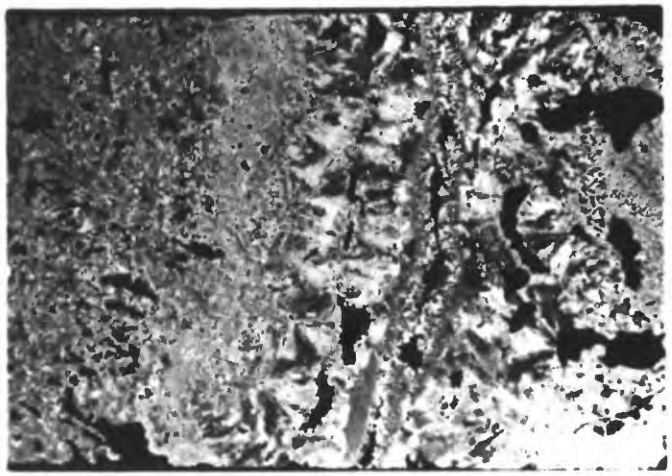

C 0 1 cm

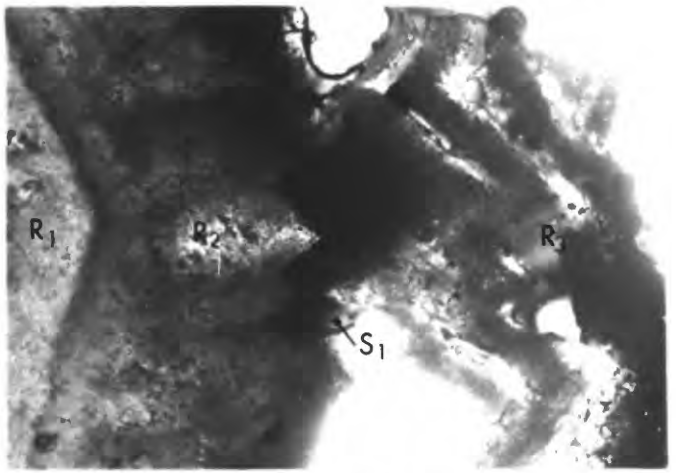

D 0 0.2 mm

Figure 11. (continued)

E) Whole thin section showing growth substages of rhodochrosite (see table 3 for description of numbered carbonate substages). Note the rhombic crystal form of the gemmy material (1_A). Epoxy encases the thin section; the two white areas in the lower half of the section are voids. (PMB-UH, transmitted light)

F) Growth substages of rhodochrosite which have been compositionally documented (table 3). Dark grey material in which the rhodochrosite (white) of substage (2) occurs is epoxy. Epoxy also overlies substage (4). (PMB-UH, reflected light)

G) Saddle-shaped rhomb growth (black). Vug has later been filled with quartz (light colored). (PMB-MU, transmitted light, crossed nicols)

H) Two periods of brecciation are evident. An early fine-grained breccia (a) was rebroken into a large fragment now cemented by later carbonate (b). Reasons for the linearity of the edges of the early breccia fragment are unclear. (PMB-LP, transmitted light)

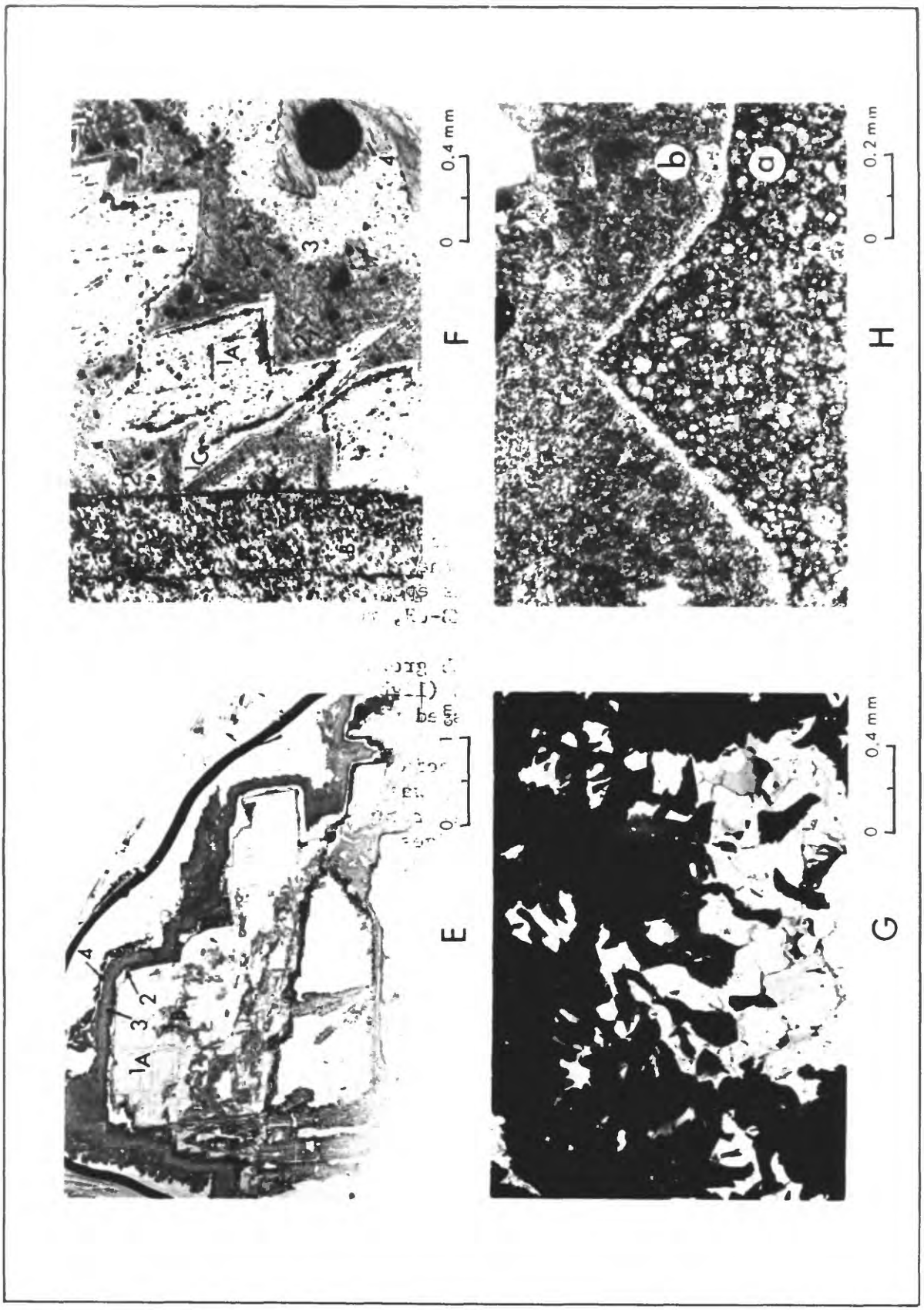
F
0
0.4 mm
1A
2
3
4
H
b
a
0
0.2 mm
E
4
3
2
1A
G
0
0.4 mm

Figure 11. (continued)

I) Selectively leached scalenohedral carbonate crystal infilled by saddle-shaped carbonate rhombs. Material surrounding the large crystal is also carbonate. (PBB-132, transmitted light, crossed nicols)

J) Late, clear borders on carbonate rhombs show possible skeletal growth. (PBB-25, transmitted light)

K) Sutured boundaries around uniformly extinguishing irregular mass of rhodochrosite suggest possible recrystallization of rhodochrosite. (PMB-NB, transmitted light, crossed nicols)

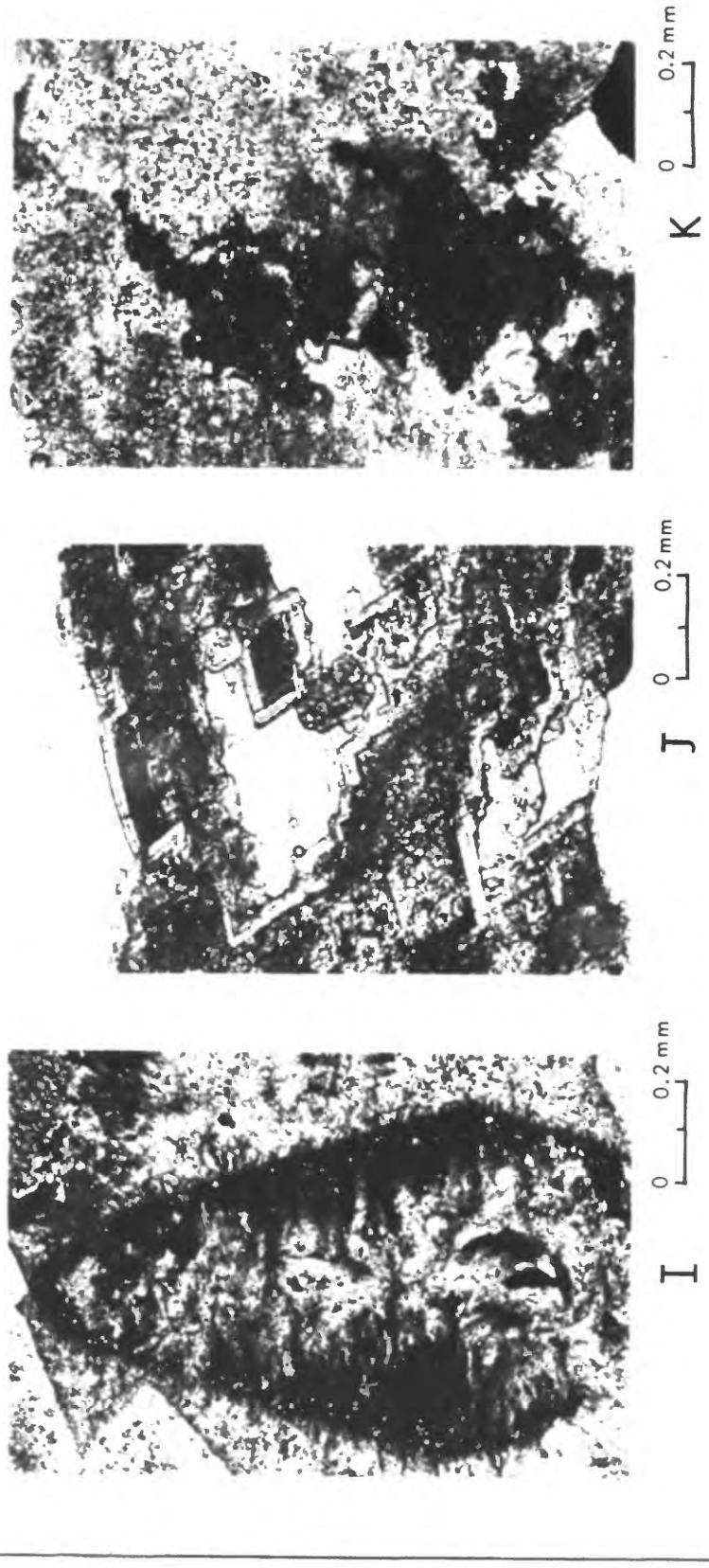
I
0
0.2 mm
J
0
0.2 mm
K
0
0.2 mm

PMB-MJ: Sample locality PMB-MJ is typical of the massive rhodochrosite at Creede. The few high-calcium analyses are associated with late rhombs; the low-calcium, iron-rich analyses also seem to be late in the sequence of carbonate deposition. The variety of textures in this carbonate is impressive (fig. 11c), but the variations cannot be correlated with compositional changes.

PMB-NB: Sample locality PMB-NB covers the entire low-calcium compositional range of the rhodochrosite generation. Although several periods of carbonate deposition can be documented (fig. 11d), they cannot be correlated with compositional variation.

PMB-UH: Sample locality PMB-UH is unique in that several periods of carbonate deposition can be distinguished compositionally. Figures 11e and 11f and table 3 document these growth substages. The earliest substage (1) is partly made up of a clear deep-pink gemmy rhodochrosite (1_A) which is manganese rich with intermediate-calcium and low-magnesium and low-iron contents. The gemmy material is usually intergrown with opaque light-pink carbonate (1_B) having a similar composition. The difference in color and opacity of these carbonates appears to be related to fluid inclusion content. The not uncommon rhombic crystal form (fig. 11e) of the gemmy material suggests that it is most likely a growth phenomenon (as opposed to a recrystallization phenomenon.

TABLE 3. Compositional ranges of growth substages in sample locality PMB-UH.
(mole percent)

SUBSTAGE	$MnCO_3$	$CaCO_3$	$MgCO_3$	$FeCO_3$
Inner gemmy (1_A) and associated light pink carbonate (1_B)	87.6 - 92.3	2.7 - 6.9	0.2 - 0.8	3.2 - 8.3
Outer gemmy (1_C)	52.4 - 77.4	5.3 - 12.3	1.1 - 6.8	15.0 - 30.7
Remnants in leached zone (2)	55.2 - 80.2	6.1 - 12.6	0.5 - 3.3	12.5 - 34.1
Inner carbonate cap (3)	67.5 - 80.0	2.2 - 8.8	0.0 - 1.7	10.1 - 29.3
Outer carbonate cap (4)	85.1 - 90.1	5.0 - 7.2	0.1 - 0.7	4.9 - 9.5

The outer zones (1_C) of the gemmy material are typically much richer in iron and contain a broad range of overall lower manganese contents; calcium and magnesium contents are substantially higher in the outer gemmy zones than in the rest of the early carbonate (1_A and 1_B). Carbonate remnants in the now-leached zone (2) above the gemmy rhodochrosite are similar in composition to the outer gemmy material except for somewhat lower magnesium contents. The late, light-pink, opaque carbonate overlying the leached zone can be divided into two substages (3 and 4), which are sometimes separated by a narrow leached band. The earlier (3) of the two substages generally contains less calcium and magnesium than the remnants in the leached zone and can be distinguished from substage (1) by the lower manganese content. The latest carbonate (4) is significantly higher in manganese than substages (1_C), (2) and (3) but is almost identical in composition to the earliest carbonate (1_A and 1_B). There appear to have been two generations of barite deposition, one prior to at least some of the gemmy carbonate deposition (fig. 11f) and the other prior to deposition of most of substage 2.

Except for sample locality PMB-UH, it has been impossible to document a "carbonate stratigraphy" through systematic compositional variations. Although many textural features can be distinguished, they are fequently so intricate as to defy mapping (fig. 11c), and they cannot be consistently correlated with characteristic compositions. Distinctive compositions are not seen in carbonate which has replaced barite (fig. 11a), in the saddle-

shaped rhombs of carbonate (figs. 8e and 11g), in early carbonate fragments (fig. 11h), in the large leached carbonate crystals (figs. 8g and 11i), or in the later small rhombs of clear carbonate (fig. 11j). The textural relations are so complicated because the rhodochrosite has undergone several periods of leaching and regrowth, may have grown as skeletal crystals (fig. 11j), may have been recrystallized, and may have been involved in now-cryptic brecciation. It is not possible to be certain that recrystallization has taken place, but some textures suggest that it has; figure 11k illustrates some large, irregular, optically continuous masses of carbonate which may have resulted from recrystallization.

Even though the compositionally documented growth substages in sample locality PMB-UH cover almost the entire range of rhodochrosite compositions seen at Creede, it has not been possible to correlate these substages with those in other sample localities. For example, virtually no gemmy rhodochrosite has been seen in other sample localities. One possible explanation for this scarcity is that the gemmy rhodochrosite is the end product of local recrystallization. However, as mentioned previously, the crystal form of some of the gemmy material is suggestive of a growth phenomenon. Confusion in relating the stages in sample locality PMB-UH with those in other sample localities is also inevitable due to the similarity in composition and appearance between the early light-pink opaque carbonate (1_B) in sample locality PMB-UH and the latest carbonate identified (4). The relatively high-calcium analyses of the leached zone remnants (2) in sample locality PMB-UH may represent the same substage as that in DH-23, but there is no way of knowing with any degree of certainty.

Color changes, like textural variations, do not appear to be related to compositional variations in the rhodochrosite and therefore cannot be used

as a visual aid to composition. The clear, deep-pink nature of the carbonate in PMB-UH appears to be due to the paucity of fluid inclusions, whereas the more typical opaque light-pink color appears to be due to abundant fluid inclusions. The tan hues in many of these manganese-rich carbonates are not related to iron content as might have been expected. A luminoscope was used in several unsuccessful attempts to show up compositionally related color changes in the carbonate. However, the early-stage carbonate is too rich in manganese to permit luminescence. Ultraviolet-excited luminescence, a process similar to cathodoluminescence, has been shown to rise to a maximum in calcite containing 3.7 mole percent $MnCO_3$ and to decrease to zero at 17 mole percent $MnCO_3$ (Brown, 1934). In addition, the presence of iron is known to inhibit luminescence.

Limited documentation, therefore, of several substages of rhodochrosite deposition, some separated by periods of barite deposition, is possible. However, visual aids like texture and color are generally not adequate to untangle the growth complexities of the rhodochrosite. In rare cases, growth textures can be related to composition (e.g., PMB-UH), but the compositional variations documented cannot be related to those in other sample localities.

Late-Stage Carbonate (Stage C)

Figure 12 shows the electron microprobe analyses of the late-stage carbonate projected onto the same kind of three-component diagram used for the early stage carbonate analyses (fig. 9). The late-stage carbonate is composed of siderite and manganosiderite. The range of iron content for this stage is much broader than for the rhodochrosite stage although the ranges of calcium and magnesium contents are similar. The analyses fall naturally into two compositional groupings, a relatively high-calcium (and

Figure 12. Compositional range of the late-stage carbonate plotted within the system $MnCO_3$-$FeCO_3$-$CaCO_3$-$MgCO_3$ projected from the $MgCO_3$ apex.

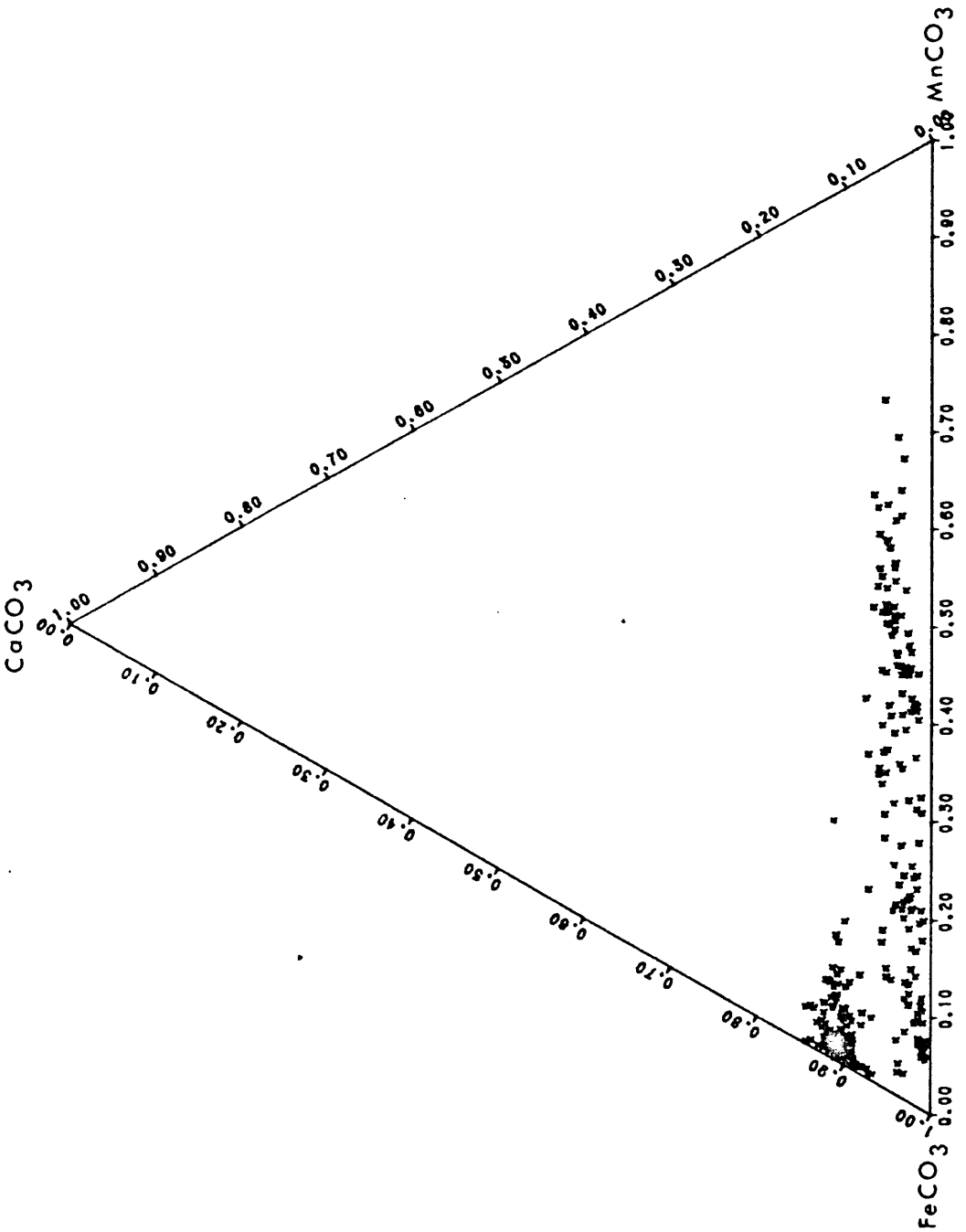
CaCO3
MnCO3
FeCO3

high-magnesium) siderite group and a low-calcium (and low-magnesium) siderite-manganosiderite series.

The siderite-manganosiderite series has the most extensive compositional range. Iron contents range from 33 to 94 mole percent $FeCO_3$ and overlap with the compositional range of the early stage carbonate. Calcium and magnesium contents (1 to 7 mole % $CaCO_3$; 1 to 4 mole % $MgCO_3$) are similar to those of the early stage carbonate. The calcium-to-magnesium ratio ranges from about 4:1 to 1:1.

The higher-calcium siderite group has a more limited compositional range with respect to iron content (72 to 87 mole % $FeCO_3$). The seemingly higher (than 87 mole % $FeCO_3$) iron contents in this group as seen in figure 13 are an artificial product of the way the analyses are plotted; because this siderite group has relatively high-magnesium contents (4 to 10 mole % $MgCO_3$), projection of the analyses onto the $FeCO_3$-$MnCO_3$-$CaCO_3$ compositional triangle distorts these data. The upper and lower limits of this group are well defined; calcium contents range from 8.5 to 13.5 mole % $CaCO_3$, with a calcium-to-magnesium ratio varying between 1:1 and 2:1.

Compositional variation within sample localities is shown in figure 13. The localities have been arranged from left to right going from south to north along each level for each vein (the highest level is in the upper left-hand corner). Compositional variation within individual sample localities with respect to iron content (and manganese content, which is inversely related to the iron content) is much broader for the Stage C carbonate than for the Stage A carbonate. The maximum range in iron content of 40 mole percent is illustrated by four sample localities, PMB-BV, PBB-44, PBB-159, and ER-123, the latter two being generally more iron-rich than the former two. Even with the broad range in iron content, however, the more iron-rich

Figure 13. Compositional ranges within each sample locality of the late-stage carbonate plotted within the system $MnCO_3$-$FeCO_3$-$CaCO_3$-$MgCO_3$ projected from the $MgCO_3$ apex.

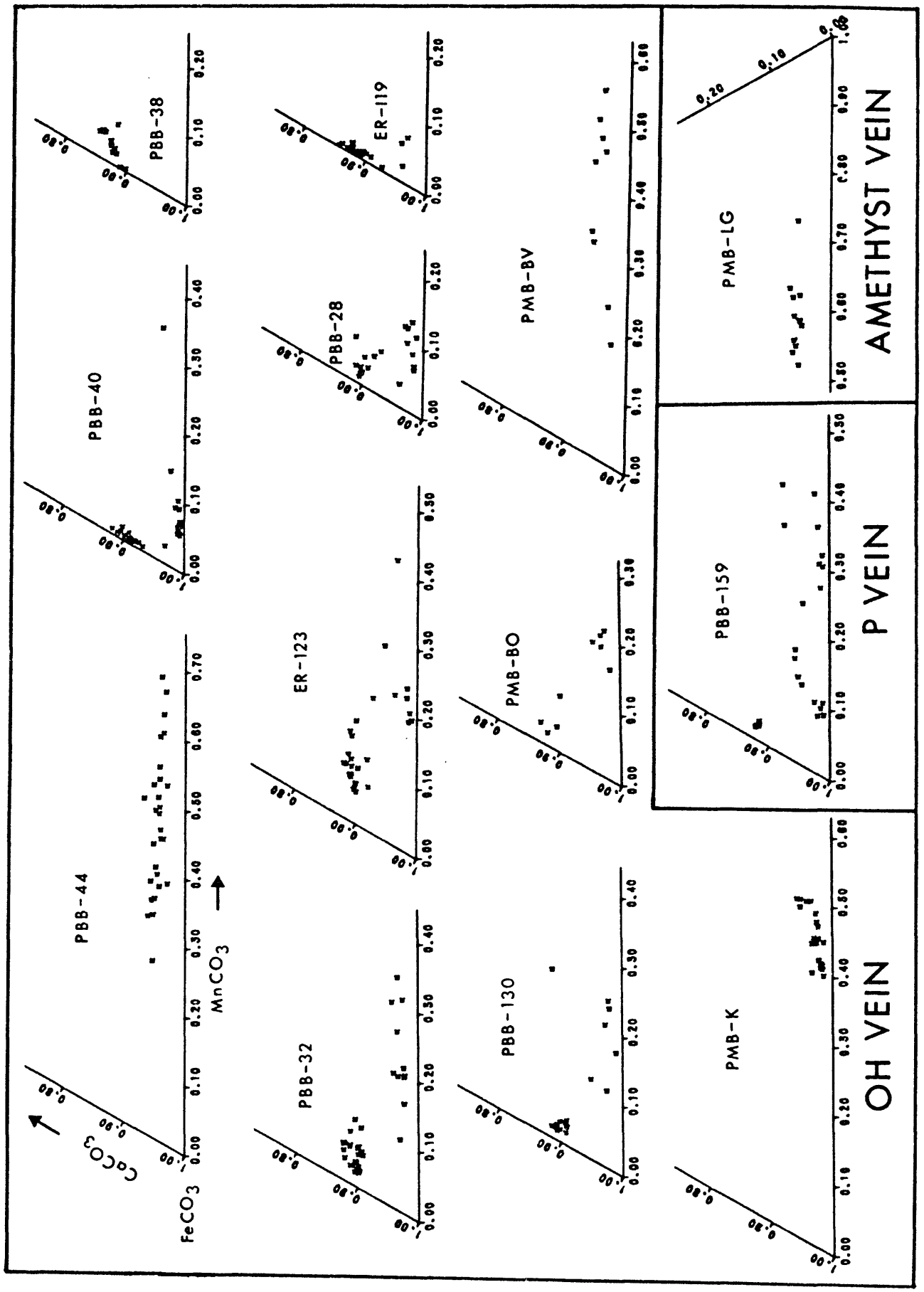
PBB-44
PBB-40
PBB-38
PBB-28
ER-119
ER-123
PMB-BV
PMB-LG
PBB-32
PMB-BO
PBB-159
PBB-130
PMB-K
CaCO3
FeCO3
MnCO3
OH VEIN
P VEIN
AMETHYST VEIN

localities rarely overlap in composition with those localities that are more manganese-rich (PMB-BV, PMB-K, PMB-LG and PBB-44). None of these four manganosiderite localities contains any of the high-calcium siderite. The high-calcium siderite is present in all the other sample localities (which are more iron-rich overall) and, except for locality PBB-38, is always associated with the low-calcium siderite.

As in the early stage carbonate, compositional variations in the late-stage carbonate are difficult to correlate with sequence of deposition, although the textural relations are not as complicated. Many of the siderite rhombs have been leached and subsequent regrowth in the leached areas complicates identification of growth stages (fig. 14a). Neither color nor degree of transparency appears to be related to composition.

Using both textural and compositional information, a very general sequence of deposition for the Stage C carbonate can be documented. The earliest siderite is low in calcium (generally 1-4 mole percent) and has been deposited in association with hematite platelets in interstitial spaces (fig. 14b). The hematite flakes are randomly oriented within the siderite matrix and appear to be a growth feature rather than an alteration product of the siderite. Electron microprobe analyses show that there has been no recognizable diffusion of iron between siderite and the adjacent hematite, corroborating this interpretation. Cores of the siderite rhombs are also low in calcium and may be equivalent to the early infilling siderite although the cores are not usually associated with hematite. Iron contents of the infilling siderite and of the cores of the rhombs range from 72-93 mole % $FeCO_3$ (although within a sample locality, the range is usually only 5 mole % $FeCO_3$). The subsequent main period of siderite rhomb growth is characterized by high-calcium contents (8.5-13.5 mole % $CaCO_3$) and again by a fairly broad

Figure 14. Photomicrographs showing textural variations of the late-stage carbonate. Material overlying the rhombs is epoxy (ER-123 shows two generations of epoxy).

A) High-calcium siderite rhomb. Leaching at the base of the rhomb was followed by regrowth of carbonate. Rhomb overlies low-iron sphalerite. (ER-123, transmitted light)

B) Hematite platelets intergrown with siderite in interstitial spaces. (PBB-32, reflected light)

C) Documented substages of siderite growth are shown; (1) low-calcium siderite + hematite, (2) high-calcium siderite, (3) low-calcium siderite. Siderite overlies quartz (grey) and sphalerite (white). (PBB-159, reflected light)

D) Siderite rhomb overlying quartz. Arrows indicate two prongs which may represent the earliest growth of this rhomb. The clear outer rim is high-calcium siderite, and the mottled inner potion is low-calcium and higher-manganese siderite. (PBB-32, transmitted light)

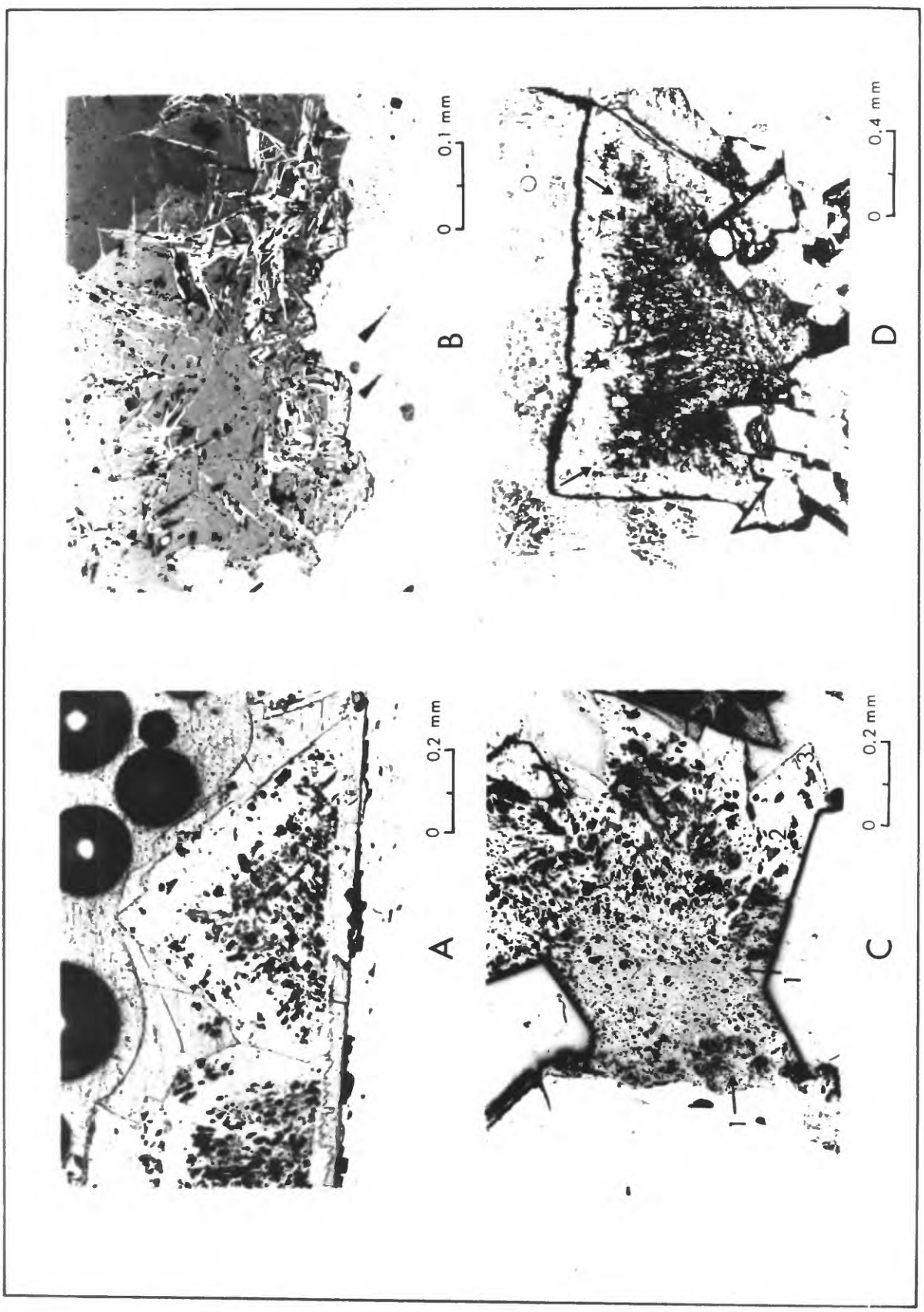
A
0 0.2 mm
B
0 0.1 mm
C
0 0.2 mm
1
2
3
D
0 0.4 mm

range of iron contents (72 to 88 mole % $FeCO_3$). A period of leaching ensued, predominantly of the low-calcium early carbonate. The last period of carbonate growth appears to have been low in calcium (1 to 7 mole % $CaCO_3$) and relatively low in iron (54 to 81 mole % $FeCO_3$ but generally below 70 mole %). It is not possible to distinguish this later substage from the earliest substage of siderite deposition unless iron contents are very low (suggesting the later substage) or hematite is present (suggesting the earlier stage) and/or growth textures are distinctive (fig. 14a). Figure 15c shows all of the above substages and illustrates that none are particularly distinctive visually.

No growth sequence has been discerned for the manganosiderite, and no correlations can be made between its compositions and those of the sideritic growth substages. It should be noted, however, that hematite is never present with the manganosiderite. The fairly broad range in iron content within most of the manganosiderite sample localities suggests that the intermediate composition is not simply due to alteration of siderite.

Several siderite rhombs which showed the greatest range in composition were examined in detail for the presence of fine-scale zoning. Electron microprobe traverses (3 μ/sec) of two rhombs in sample localities PBB-130 and PBB-32 showed that the distribution of iron was highly irregular. No systematic variation could be documented except for the probable presence of two relatively high-manganese prongs (fig. 14d) suggestive of a dendritic-type growth followed by infilling and formation of crystal faces. Electron microprobe raster scans of 80μ x 64μ areas also could define no compositional zoning and suggested a patchy distribution of calcium, magnesium and manganese. Examination of the rhomb in figure 14d under the scanning electron microscope also suggested that the rhomb was a fine patchwork of

scattered iron-rich and manganese-rich regions. However, the compositional differences seem to be too small to show substantial contrast between regions.

Compositional Zoning within the Main Vein Systems

No useful compositional patterns in either the rhodochrosite or the siderite-manganosiderite have been identified within any of the four major vein systems. Along the OH vein (plate Ib), a few rhodochrosite localities lie in the very southern end, but the siderite-manganosiderite is the predominant carbonate along the rest of the vein. Within the siderite group, no systematic variation in composition can be related to vertical or horizontal position. The three manganosiderite localities (PBB-44, PMB-BV, and PMB-K) appear to be randomly scattered among the siderite localities; the only other manganosiderite locality (PMB-LG) is isolated on the northern Amethyst vein (plate Ib). Overall, the late-stage carbonate localities along the OH vein are concentrated in the upper two-thirds of the mined area. It is important to note, however, that the fluorite on which much of the late-stage carbonate grew has been extensively leached, and that, as a result, the late-stage carbonate has been preserved only on those locations where Stage C was protected from later solutions.

No systematic variations among the carbonate sample localities along the Bulldog vein (all containing only the early-stage carbonate) have been identified. However, carbonate is most abundant in the lower levels (plate Ia). The P vein and Amethyst vein also show no distributional patterns with respect to carbonate compositions, possibly due to the paucity of sample localities (2 on the P vein and 9 related to the Amethyst vein). Nevertheless, within each of these veins, as well as in the OH vein, the

rhodochrosite localities are situated towards the southern end and the siderite towards the more northern. As the Bulldog mine is developed further north, rhodochrosite could very well give way to siderite, as happens along the other three major veins.

Minor and Trace Element Contents of the Creede Carbonates

In addition to the major-element distribution in the Creede carbonates discussed above, minor- and trace-element variations can also provide important clues as to the nature of the ore fluid. Emission spectrographic analyses of five early-stage carbonates and three late-stage carbonates (table 4) show that both the early- and late-stage carbonates contain significant quantities of the following elements which are of geochemical interest: Ba, Sr, Pb, Zn and Cd.

Barium is present in all the carbonates, though in higher concentrations in the rhodochrosite (84-1200 ppm) than in the siderite (4.4-7.4 ppm). Consequently, barium content could turn out to be a better discriminator of carbonate stages than the Fe/Mn ratio. Contamination of these particular samples with barite is unlikely. It seems reasonable that there was probably always plenty of barium in solution during rhodochrosite deposition because rhodochrosite deposition sometimes alternated with barite deposition. The low-barium values in the siderite samples suggest that there was little barium in solution when this carbonate was deposited because barium should have little, if any, preference between rhodochrosite and siderite. With the exception of the barite at sample locality PBB-159, neither barite nor barite molds have been found associated with the siderite stage. The strontium values are also noteworthy, especially because similar values occur in both the rhodochrosite (3.1-16 ppm) and the siderite (4.5-20 ppm).

TABLE 4. Emission spectrographic analyses of Creede carbonates.
The standard deviation of any single answer is +50% and -33%.
Analyses by Norma Rait, U.S. Geological Survey.

	EARLY STAGE (A) CARBONATE					LATE STAGE (C) CARBONATE		
Sample / Element	PMB-JX	PMB-MP	PMB-FW	PMB-MU	PBB-112	PBB-32	ER-119	PMB-LG
SI %	0.13	0.13	0.087	1.1	< 0.17	< 0.17	0.056	1.0
AL %	< 0.036	< 0.036	< 0.036	< 0.036	< 0.036	0.072	0.067	< 0.036
FE %	5.7	5.2	0.85	1.5	7.6	28	> 27	19
MG %	0.21	0.24	0.10	0.15	0.17	0.67	0.64	0.18
CA %	0.94	1.1	1.3	0.74	1.5	2.1	2.2	0.99
NA %	0.53	0.15	0.32	0.18	> 5.2	< 0.0076	1.1	> 5.2
K %	< 0.076	< 0.076	< 0.076	< 0.076	< 0.076	< 0.076	< 0.076	< 0.076
TI %	< 0.0076	0.020	0.029	< 0.0076	< 0.0076	0.011	< 0.0076	0.016
P %	0.84	0.75	0.12	0.69	< 0.081	< 0.081	< 0.081	< 0.081
MN %	41	40	44	37	29	2.1	1.2	19
AG PPM	5.2	25	2.0	17	3.0	2.4	0.71	0.68
AS PPM	< 170	< 170	< 170	< 170	< 170	< 170	< 170	< 170
AU PPM	< 11	< 11	< 11	< 11	< 11	< 11	< 11	< 11
B PPM	< 3.6	< 3.6	< 3.6	< 3.6	< 17	< 17	< 17	< 17
BA PPM	370	1200	390	570	84	7.4	7.3	4.4
BE PPM	1.0	0.97	4.1	0.80	2.1	< 25	< 25	4.5
BI PPM	< 25	< 25	< 25	< 25	< 25	< 25	< 25	< 25
CD PPM	< 36	< 52	< 36	< 36	< 52	< 36	120	340
CE PPM	< 100	< 100	< 100	< 100	< 32	< 32	< 32	< 100
CO PPM	< 1.1	< 1.1	< 1.1	< 1.1	< 1.1	< 1.1	1.9	< 1.1
CR PPM	4.0	< 1.1	< 1.1	< 1.1	< 1.1	5.8	4.5	4.3
CU PPM	5.6	30	5.3	95	9.7	5.0	7.2	5.3
DY PPM	< 36	< 36	< 76	< 36	< 76	< 36	< 36	< 36
ER PPM	< 52	< 52	< 52	< 52	< 11	< 11	< 11	< 11
EU PPM	< 1.7	< 1.7	< 1.7	< 1.7	< 1.7	< 1.7	< 1.7	< 1.7
GA PPM	< 2.5	< 2.5	< 2.5	< 2.5	< 2.5	< 2.5	< 2.5	< 2.5
GD PPM	< 7.6	< 7.6	< 7.6	< 7.6	< 7.6	< 7.6	< 7.6	< 7.6
GE PPM	< 5.2	< 5.2	< 5.2	< 5.2	< 5.2	< 5.2	< 5.2	< 5.2
HF PPM	< 110	< 110	< 110	< 110	< 110	< 110	< 110	< 110
HO PPM	< 7.6	< 7.6	< 7.6	< 7.6	< 7.6	< 7.6	< 7.6	< 7.6
IN PPM	< 7.6	< 7.6	< 7.6	< 7.6	< 7.6	< 7.6	< 7.6	< 7.6
IR PPM	< 17	< 17	< 17	< 17	< 17	< 17	< 17	< 17
LA PPM	< 11	< 11	< 11	< 11	< 11	< 11	< 11	< 11
LI PPM	< 76	< 76	< 76	< 76	< 76	H*	H*	< 76
LU PPM	< 25	< 25	< 25	< 25	< 25	< 25	< 25	< 25
MN PPM	410000	400000	440000	370000	290000	21000	12000	190000
MO PPM	3.5	4.0	< 2.5	3.0	< 3.6	< 5.2	< 5.2	< 5.2
NB PPM	36	34	40	30	20	4.6	< 3.6	10
ND PPM	< 52	< 52	< 52	< 52	< 52	< 52	< 52	< 52
NI PPM	< 5.2	< 5.2	< 5.2	< 5.2	< 5.2	< 5.2	< 5.2	< 5.2
OS PPM	< 11	< 11	< 11	< 11	< 11	< 11	< 11	< 11
PB PPM	1000	95	550	150	220	120	160	550
PD PPM	< 1.7	< 1.7	< 1.7	< 1.7	< 1.7	< 1.7	< 1.7	< 1.7
PR PPM	< 76	< 76	< 76	< 76	< 76	< 76	< 76	< 76
PT RRM	< 7.6	< 7.6	< 7.6	< 7.6	< 7.6	< 7.6	< 7.6	< 7.6
RE PPM	< 52	< 52	< 52	< 52	< 52	< 11	< 11	< 52
RH PPM	< 1.1	< 1.1	< 1.1	< 1.1	< 1.1	< 1.1	< 1.1	< 1.1
RU PPM	< 3.6	< 3.6	< 3.6	< 3.6	< 3.6	< 3.6	< 3.6	< 3.6
SB PPM	< 110	< 110	< 110	< 110	< 110	< 110	< 110	< 110
SC PPM	3.1	4.4	5.0	5.0	35	2.1	3.0	45
SM PPM	< 52	< 52	< 52	< 52	< 52	< 52	< 52	< 52
SH PPM	< 7.6	< 7.6	< 7.6	< 7.6	< 7.6	< 7.6	< 7.6	< 7.6
SR PPM	3.1	16	7.5	3.8	2.8	19	20	4.5
TA PPM	< 360	< 360	< 360	< 360	< 360	< 360	< 360	< 360
TB PPM	< 36	< 36	< 36	< 36	< 36	< 36	< 36	< 36
TH PPM	< 25	< 25	< 52	< 52	< 52	< 52	< 25	< 52
TL PPM	< 11	< 17	< 11	< 17	< 11	< 11	< 11	< 11
TM PPM	< 5.2	< 5.2	< 5.2	< 5.2	< 5.2	< 5.2	< 5.2	< 5.2
U PPM	< 360	< 360	< 360	< 360	< 360	< 360	< 360	< 360
V PPM	120	120	130	110	81	15	45	170
W PPM	< 11	< 11	< 11	< 11	< 11	< 11	< 11	< 11
Y PPM	< 1.7	< 1.7	< 1.7	< 76	22	< 1.7	< 1.7	< 76
YB PPM	0.95	< 0.76	< 0.76	1.1	3.2	< 0.11	< 0.11	< 5.2
ZN PPM	3700	1100	2200	1700	> 11000	680	5000	> 11000
ZR PPM	8.0	< 7.6	< 7.6	< 7.6	< 7.6	90	40	< 7.6

*'H' denotes interference for an element.

The highly variable Sr/Ba ratios suggest that the strontium and barium contents were controlled by reactions that are beyond present observation.

Both the rhodochrosite and the siderite analyses show a broad range of lead and zinc contents, and two siderite samples show significant cadmium contents. The only two samples which might be contaminated by sphalerite and/or galena are PMB-JX and ER-119. However, sample selection for analyses was based on microscopic and macroscopic observations of the sample locality specifically to minimize the possibility of contamination. Most of the lead and zinc is, therefore, considered to be in the carbonate itself, and it is known (Deer and others, 1963) that zinc can substitute for manganese in rhodochrosite and for iron in siderite. The Zn/Cd ratios for the two samples in which cadmium was detected (ER-119 and PMB-LG) are 42:1 and at least 32:1 respectively. These ratios are considerably lower than the more typical 200:1 ratio for most of the sphalerite at Creede. However, a sphalerite with a similar low Zn:Cd ratio was found by microprobe analysis in one carbonate locality, PMB-LP.

In order to confirm that zinc and cadmium were present in solid solution in the carbonate and not as physical impurities, semi-quantitative electron microprobe analyses were carried out using sphalerite and greenockite as standards. The analyses ranged from below the limit of detection (approximately 1000 ppm) to 8400 ppm zinc and 2400 ppm cadmium for the rhodochrosites analyzed (PBB-132, PMB-MU, PMB-KA and PMB-LP) and to 7000 ppm zinc and 1800 ppm cadmium for the siderites analyzed (PBB-28 and PBB-32). At these low levels and using sulfides as the standards, the error on the analyses is roughly ±10 percent of the amount present. The microprobe analyses show much higher average values for the zinc and cadmium contents and lower Zn:Cd ratios (2:1 to 8:1) than do the spectrographic analyses. This discrepancy

may be due to the apparently extremely irregular distribution of these elements in the carbonates. There remains the possibility that the cadmium and zinc values might be supergene in origin, occurring as coatings on intricately etched primary carbonate. This origin would be consistent with the scatter of values and with the lack of relationship between the zinc and cadmium values from the microprobe analyses.

Other minor and trace elements detected in the carbonates include P, Ag, Cr, Cu, Mo, Sc, V, and Zr. The rhodochrosite appears to contain more silver than the siderite and also is rich in phosphorous. Although one might expect P and V to be related, they do not vary together.

Spatial Distribution of Carbonates

No sample locality has been found in which the early-stage and late-stage carbonates occur together. The early-stage carbonate is limited to the southern third of the central vein system whereas the late-stage carbonate is restricted to the northern two-thirds.

The manganese-rich early-stage carbonate is the only carbonate thus far found along the Bulldog vein (fig. 15a). It is very similar both in composition and texture to the carbonate found along the southern Amethyst vein (fig. 15b). This similarity suggests that these carbonates were deposited from the same type of fluids, and that therefore these two vein systems were open at the same time. By the same reasoning, the manganese-rich carbonate (PHW-A) found along the P vein (fig. 15c) was also probably deposited during the same period; this carbonate is the northernmost early-stage carbonate found, with the exception of the carbonate in the Equity mine.

Although the two Equity mine rhodochrosite samples (PMB-HT and PHW-BQ)

Figure 15. Compositional ranges of early- and late-stage carbonate samples plotted within the system $MnCO_3$-$FeCO_3$-$CaCO_3$-$MgCO_3$ projected from the $MgCO_3$ apex and arranged according to vein system. Four sample localities (PBB-112, PBB-113, PMB-CI, PBB-25) have been plotted on both the Amethyst vein and OH vein figures. These samples are located in the area of structural discontinuity where the OH vein has lost its identity into a swarm of minor fractures and where the samples could have been in contact with depositing fluids from either the Amethyst or OH veins (or both).

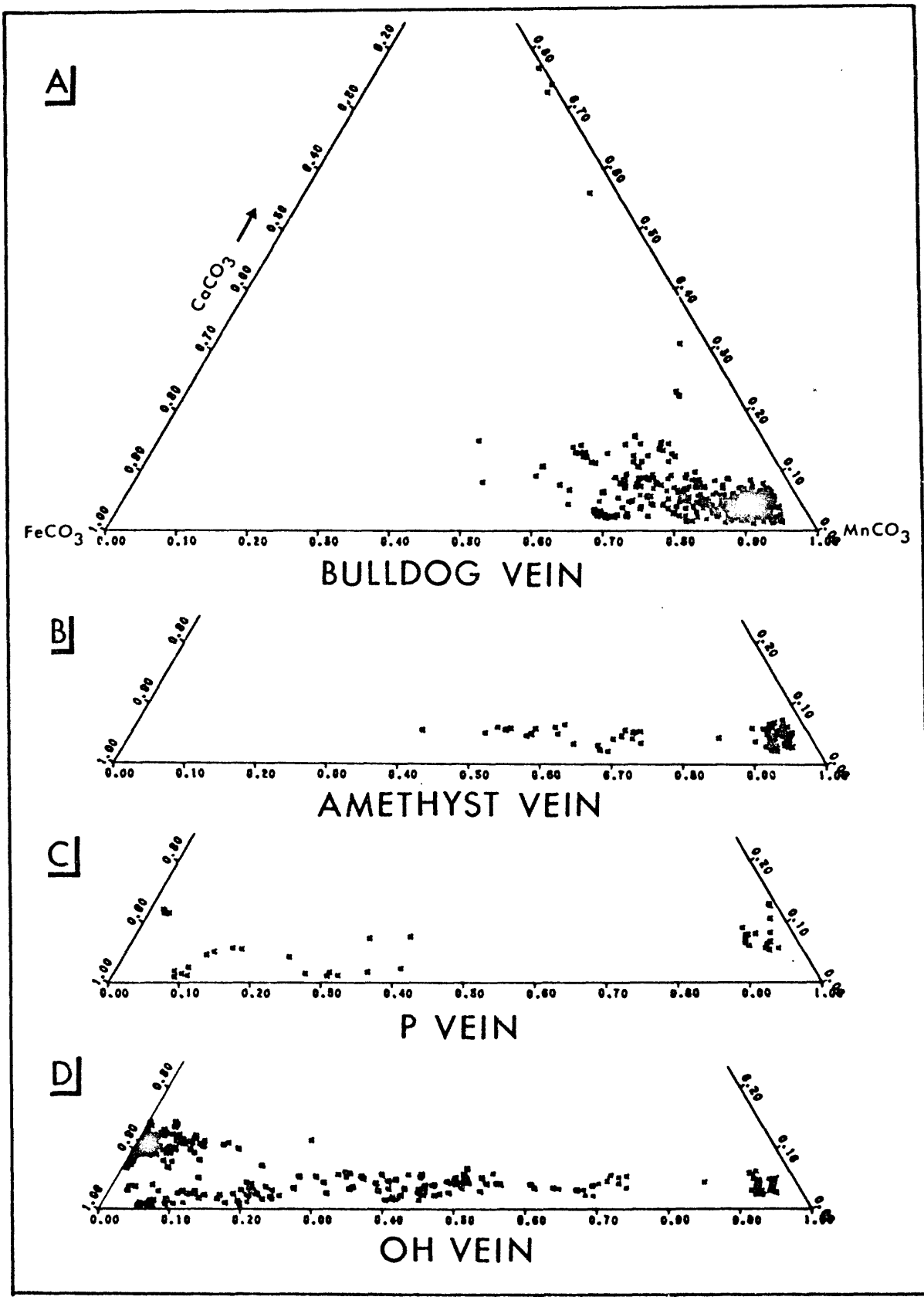
A
CaCO3
FeCO3
MnCO3
BULLDOG VEIN
B
AMETHYST VEIN
C
P VEIN
D
OH VEIN

are similar in composition to the rhodochrosite from the southern third of the Creede district, it is difficult to reach useful conclusions about them at this point. The Equity mine is geographically removed from the main vein system, and the minerals associated with the rhodochrosite are restricted to inesite ($Ca_2Mn_7Si_{10}O_{28}(OH)_2 \cdot 5H_2O$), which has not been identified in any other locality in the district, and quartz; no barite, which is so abundant in the southern third of the district, has been reported from the Equity mine. On the other hand, the wallrock alteration is mineralogically very similar to that along the OH and Bulldog veins. Overall, it appears that knowledge of the Equity mine is still too meager to permit judgement as to whether the ore deposition in the Equity mine was part of the main mineralization.

Late-stage siderite-manganosiderite localities are restricted almost entirely to the OH vein (fig. 15d). Other siderite localities include one (PBB-159) of the two carbonate localities along the P vein (fig. 15c) and one locality (PMB-LG) along the northern part of the Amethyst vein, the northernmost late-stage carbonate found. Siderite was probably deposited further north, but the northern Amethyst vein is presently inaccessible. Siderite of the P-vein and manganosiderite of the Amethyst vein both have compositional ranges that are compatible with the range defined by the rest of the late-stage carbonates on the OH vein and were, therefore, probably deposited by similar fluids during the same time period. No siderite has been recognized along the southern Amethyst or Bulldog veins.

There are several possible interpretations for the geographic restrictions of the two stages of carbonate deposition in the Creede district. The predominance of the early-stage carbonate in the southern portions of the district suggests that the northern portions may not have been open

during the period of rhodochrosite deposition. The restriction of the rhodochrosite along the OH vein and P vein to areas near their intersection with the southern Amethyst vein, which was open at that time, would then also be understandable. All veins probably would have been open during siderite-manganosiderite deposition (Stage C) since the enveloping main-stage mineralization (Stages B and D) is present along all the veins.

An alternative explanation is that the early -stage carbonate was deposited throughout the district and was subsequently hydrothermally leached in the northern portions. Substantial leaching of rhodochrosite has been seen along the southern Amethyst and Bulldog veins. The isolated rhodochrosite locality along the P-vein (PHW-A) could then easily be interpreted as a remnant that survived the extensive leaching. However, it is not possible to document the original extent of early-stage carbonate deposition. Only a few molds of rhodochrosite crystals (e.g., sample locality PMB-NB) have been found, probably because Stage A was nearly monomineralic and because leaching apparently took place prior to Stage B deposition.

Another explanation for the distribution of the carbonates involves the possibility that the rhodochrosite and/or siderite could represent a lateral facies which either died out completely or is represented by some other mineral assemblage further north or south respectively. The quartz overlying the wallrock in the OH vein could possibly be a northern facies of the rhodochrosite. Another alternative explanation is that the siderite might represent deposition from convecting hydrothermal fluids which had previously been in contact with and leached the rhodochrosite; the more iron-rich composition of the later carbonate may have been due to the presence of an iron buffer system.

Carbonate Phase Relations

Subsolidus phase relations in the binary systems $CaCO_3$-$FeCO_3$, $MgCO_3$-$FeCO_3$, $MnCO_3$-$FeCO_3$ and in the ternary systems $CaCO_3$-$MgCO_3$-$FeCO_3$ and $CaMg(CO_3)_2$ - $CaMn(CO_3)_2$ - $CaFe(CO_3)_2$ have been examined through phase equilibrium studies by Rosenberg (1960; 1963a; 1963b; 1967; 1968). The general temperature range covered was from 550°C to 350°C, although some experimental runs at the lower temperatures were not completed because reaction rates were so slow, attainment of equilibrium taking several months or more. The experimental runs were carried out at CO_2 pressures sufficient to prevent dissociation of the carbonate. From these data and from additional data from previous investigations of binary carbonate systems, Rosenberg (1960) predicted the phase relations in the quaternary system $MnCO_3$-$FeCO_3$-$CaCO_3$-$MgCO_3$ (fig. 16) at 450°C. Even though fluid inclusions studies (Roedder, 1965; 1977) show that the Creede ores were deposited at much lower temperatures (around 250°C), figure 16 is useful in that it shows a maximum size for the one-phase fields, which probably decrease only slightly in size at lower temperatures.

Figure 17 shows the microprobe analyses of the Creede carbonates projected onto the same base as in figure 16. The analyses were plotted separately on each triangle by projection from the appropriate fourth apex. Only analyses with less than 30 mole percent $FeCO_3$ and less than 30 mole percent $MnCO_3$ were plotted respectively on the $MnCO_3$-$CaCO_3$-$MgCO_3$ and $FeCO_3$-$CaCO_3$-$MgCO_3$ triangles to avoid undue distortion of the data. All data were plotted in the central $MnCO_3$-$FeCO_3$-$CaCO_3$ triangle since $MgCO_3$ contents are low. All except the six analyses from PBB-147 which contained greater than 20 mole percent $CaCO_3$ were plotted on the $MnCO_3$-$FeCO_3$-$MgCO_3$ triangle.

Comparison of figures 16 and 17 shows that the Creede carbonate data

Figure 16. Phase relations for the system $MnCO_3$-$FeCO_3$-$CaCO_3$-$MgCO_3$ at 450°C.

Abbreviations:
sid. = siderite
rho. = rhodochrosite
ct. = calcite
mag. = magnesite
dol. = dolomite
ank. = ankerite
s.s. = solid solution

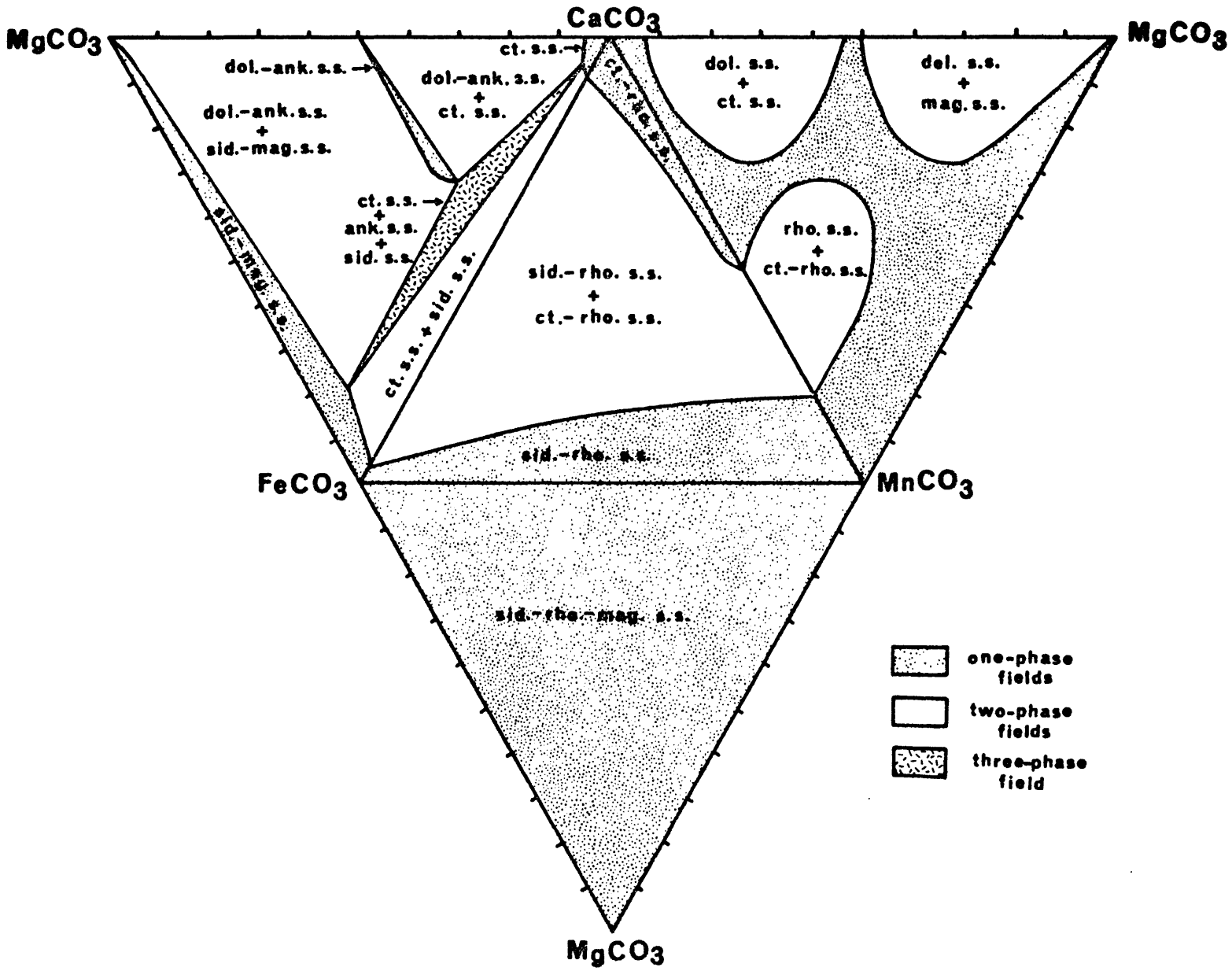
CaCO3
MgCO3
MgCO3
FeCO3
MnCO3
MgCO3
dol.-ank. s.s.
dol.-ank. s.s.
+
ct. s.s.
ct. s.s.
dol.-ank. s.s.
+
sid.-mag. s.s.
ct. s.s.
+
ank. s.s.
+
sid. s.s.
sid.-mag. s.s.
ct. s.s. + sid. s.s.
ct.-rho. s.s.
sid.-rho. s.s.
+
ct.-rho. s.s.
dol. s.s.
+
ct. s.s.
dol. s.s.
+
mag. s.s.
rho. s.s.
+
ct.-rho. s.s.
sid.-rho. s.s.
sid.-rho.-mag. s.s.
one-phase fields
two-phase fields
three-phase field

Figure 17. Compositional range of all the carbonate samples analyzed by electron microprobe plotted within the system $MnCO_3$-$FeCO_3$-$CaCO_3$-$MgCO_3$. Single-phase fields are shown within the system $MnCO_3$-$FeCO_3$-$CaCO_3$.

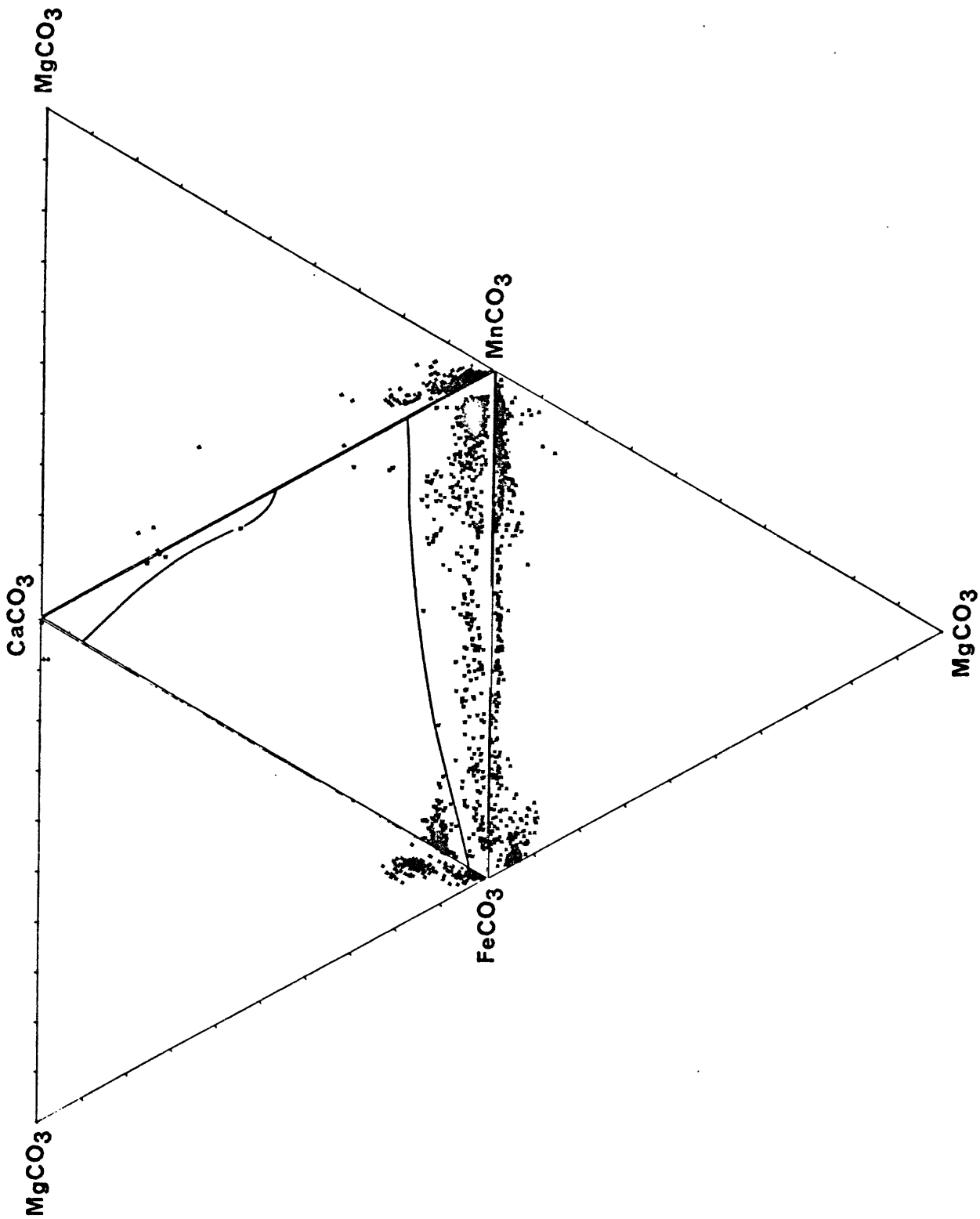
MgCO3
MnCO3
CaCO3
MgCO3
MgCO3
FeCO3

are consistent, for the most part, with the experimentally determined solid solution between siderite and rhodochrosite. It is interesting to note that the compositional range of each carbonate generation is more or less mutually exclusive (figs. 9 and 12), even though the combined analyses of both generations cover the entire range of solid solution. The compositional limitations within each generation suggest that the chemistry of the ore-fluid and/or the geochemical conditions under which deposition took place were more important than crystal chemical factors. The limited range in $MgCO_3$ contents in the $MnCO_3$-$FeCO_3$-$MgCO_3$ solid solution field suggests limitations due to the chemistry of the ore fluid.

The distinctive bimodal grouping of the siderite compositions is immediately apparent in figure 17, the break between the two groups being most apparent with respect to $CaCO_3$ contents. Comparison with figure 16 indicates that even at 450°C, the higher-calcium siderites would fall in the two phase field of calcite + siderite. However, powder diffraction patterns of sample locality ER-119, a siderite containing predominantly the high-calcium siderite, show that these carbonates consist of only one phase. Measurement of a powder pattern taken with chromium radiation showed a unit cell with dimensions of $a_0 = 4.711$ and $c_0 = 15.521$. The sharp limitations on the compositional range of the high-calcium siderites suggest the possibility of a 9 to 1 ordering of calcium ions with the iron and manganese ions. However, x-ray precession photographs of single crystals showed no evidence of a superlattice. Hence, the high-calcium siderite must either represent a metastable phase or an unanticipated stable siderite-like phase field which perhaps should have a mineralogically distinct name. It is probably significant that the leaching of the late-stage carbonate that took place subsequent to high-calcium siderite deposition appears to have

affected the presumably more stable low-calcium core of the rhombs than the high-calcium outer rim (figs. 14a and 14d).

Although all of the rhodochrosite analyses appear to fall within the one-phase field, the small subgroup of the high-calcium rhodochrosite exemplified by sample locality DH-23 (fig. 10a) was also examined using X-ray diffraction techniques. X-ray precession photographs of a single crystal of high -calcium rhodochrosite from locality DH-23 showed no superlattice, but the powder pattern permitted measurement of three similar rhodochrosite unit cells of varying degrees of sharpness (medium sharp: a = 4.781, c = 15.79; diffuse: a = 4.755, c = 15.65; very diffuse; a = 4.73, c = 15.59). The sharp cell would represent a carbonate with a composition falling roughly midway between the two main compositional groups in locality DH-23 (fig. 10a). The diffuse cell corresponds with calculated measurements for the lower lefthand analysis in fig. 10a. The very diffuse cell would correspond with a slightly more iron-rich, calcium-poor analysis. The preservation of several reasonably distinct unit cells documents changes in the composition of the ore fluids which must have taken place in sharp increments rather than gradually.

Isotope Data

Isotopic study has become an increasingly important approach in the process of understanding the genesis of an ore deposit. At Creede, isotopic analyses of the carbonate minerals and of three associated quartz separates were carried out to evaluate the origin of the hydrothermal fluids for the carbonate stages and to determine the source of the carbon. These isotope data were gathered as part of a more comprehensive study done in cooperation with R. O. Rye, the results of which will be reported

in several additional papers. All isotopic analyses were carried out by R. O. Rye and J. Whelan, U.S. Geological Survey, Denver, Colorado.

The isotopic data are reported as $\delta^{18}O$, $\delta^{13}C$ and δD where

$$\delta = \left(\frac{R_{sample}}{R_{standard}} - 1 \right) \times 1000$$

where R is $^{18}O/^{16}O$, $^{13}C/^{12}C$ or D/H. The isotopic values discussed below are therefore not absolute values but represent relative deviations from a standard value. For oxygen and deuterium values, the standard used is Standard Mean Ocean Water (SMOW) (Craig, 1961). For carbon values, the standard used is the Chicago PDB standard (Craig, 1957).

Sixteen carbonate samples were chosen for isotopic analysis on the basis of compositional variations, distribution within the vein systems and position in the sequence of mineral deposition. Three quartz samples were chosen for isotopic analyses based on their textural relations with the carbonate, suggestive of contemporaneous precipitation. The deuterium values were determined directly from analyses of primary fluid-inclusion liquids from two rhodochrosite samples. The similarity among the values of the analyses suggests that secondary inclusions are not a significant problem. The oxygen and carbon isotopic compositions of the fluids were determined indirectly from calculations using the isotopic analyses of the carbonate minerals, which are presumed to be in equilibrium with the fluids depositing them. The calculations are based on the calcite - H_2O and calcite - CO_2 fractionation curves of O'Neil and others (1969) and Bottinga (1968). The fractionation curves for rhodochrosite should be very close to those for calcite because fractionation curves tend to be mass dependent.

For the quartz analyses, the quartz-H_2O fractionation curve of Bottinga and Javoy (1973) was used.

Isotopic fractionation between fluid and mineral is temperature dependent. It is, therefore, necessary to estimate the temperature of formation before determining the isotopic composition of the fluid from the mineral data. Fluid inclusion data from sphalerite, quartz, and fluorite have shown that temperatures at the time of ore deposition at Creede were around 250°C (Roedder, 1965; 1977; Barton and others, 1977). Although no fluid inclusion measurements have yet been made on the carbonates, fluid inclusions in the fluorite on which much of the siderite precipitated show a temperature range of 210°C to 270°C. Until better data are available, an average temperature of carbonate deposition of 250°C will be assumed on the premise that the temperature range during carbonate deposition was not substantially different than during main-stage ore deposition. In addition to being temperature dependent, $\delta^{13}C$ values are also a function of pH, f_{O_2} and the isotopic composition of the carbon ($\delta^{13}C_{\Sigma C}$) in the ore fluid. It is assumed that at Creede the pH is fixed by the hydrolysis of feldspar to sericite when $a_{K+} = 10^{-1.33}$ (pH = 5.4 at 250°C, essentially neutral).

Table 5 shows the isotopic compositions of the analyzed carbonate and quartz samples and of the waters from which they precipitated. The two carbonate stages appear to be very similar isotopically, the relatively narrow range of oxygen values suggesting similar conditions during both periods of carbonate deposition. The calculated $\delta^{18}O$ values for fluids in equilibrium with the carbonate at 250°C range from +4.2‰ to +9.9‰, with most values falling between +7‰ and +9.9‰. The two δD values measured, both from the rhodochrosite stage, are -78‰ and -82‰.

Isotopic fractionation between carbonate and associated quartz samples

TABLE 5. Isotopic analyses of Creede carbonates.

SAMPLE	VEIN	LOCATION	ISOTOPIC COMPOSITIONS OF WATERS *						ISOTOPIC COMPOSITIONS OF MINERALS					
			Quartz	Rhodochrosite			Siderite		Quartz	Rhodochrosite		Siderite	
			$\delta^{18}O$	$\delta^{18}O$	$\delta^{13}C$	δD	$\delta^{18}O$	$\delta^{13}C$	$\delta^{18}O$	$\delta^{18}O$	$\delta^{13}C$	$\delta^{18}O$	$\delta^{13}C$
PMB-KA-542-71	Bulldog	130' above 9360 50' north of A180 manway	-1.2	6.8	-5.3	-	-	-	10.10	13.6	-6.6	-	-
PBB-132-8-74B	"	9360 level, south end 243 crosscut	-	7.4	-4.9	-78	-	-	-	14.2	-6.2	-	-
PBB-145-37-74	"	9360 level, 145 crosscut	0.77	8.4	-5.2	-	-	-	12.07	15.7	-6.5	-	-
PMB-MU-642A-74	"	9360 level, north slusher drift off 145 crosscut	-	7.8	-4.9	-	-	-	-	14.6	-6.2	-	-
PBB-147-50-74	"	9360 level, 59 slusher drift	-2.94	7.8	-5.0	-	-	-	8.36	14.6	-6.4	-	-
PMB-GC-338-68	"	9360 level, A72 crosscut east	-	9.4	-4.2	-	-	-	-	16.2	-5.5	-	-
PMB-LP-596-74	"	9200 level, slusher drift 291	-	8.0	-5.3	-	-	-	-	14.8	-6.6	-	-
PMB-NB-658-74	"	9200 level, 50' south of 291 crosscut	-	4.4	-5.7	-82	-	-	-	11.2	-7.0	-	-
PMB-FW-331-68	Amethyst	Comm. 4, 50' north of west crosscut	-	4.2	-5.6	-	-	-	-	11.0	-6.9	-	-
PBB-40-119-59	OH	7 level, 80' north of 8 Raise	-	-	-	-	9.9	-6.9	-	-	-	16.7	-8.2
ER-119-65	"	60' above 9 level, 30' south of 19 Raise	-	-	-	-	9.6	-6.2	-	-	-	16.4	-7.5
PMB-BO-227-65	"	9 level, 90' south of K3 Raise	-	-	-	-	8.1	-4.8	-	-	-	14.9	-6.1
PBB-28-90-59	"	9 level, 50' south of 17 Raise	-	-	-	-	7.8	-5.0	-	-	-	14.6	-6.3
PMB-K-50-59	"	11 level, 10½ Raise	-	-	-	-	4.9	-2.7	-	-	-	11.7	-4.0
PBB-112-36-68	"	NW drift 80' south of Volunteer Raise	-	9.7	-5.7	-	-	-	-	16.5	-7.0	-	-

*Estimated assuming T = 250°C; pH = 5.4; $f_{O_2} > 10^{-38}$

can be used to estimate temperature of deposition. However, in using this technique a number of important assumptions must be made. First, it must be shown (or assumed) that the quartz and carbonate grew in isotopic equilibrium with each other (that is, grew together from essentially the same fluids). For this evidence, one is dependent almost completely on textural information. Second, the hydrothermal fluids must be assumed to have maintained a uniform isotopic composition over the period of time represented by the samples taken. Even if the isotopic composition of the fluids did fluctuate over time, it would still be possible to measure reasonable isotopic fractionation between the quartz and carbonate if their growth rates were similar; however, the isotopic values would then represent only an average of all the fluctuating isotopic compositions. Third, the assumption must be made that the original isotopic compositions of the minerals have been preserved. Fourth, the fractionation curves must be assumed to be reliable.

With respect to the fourth assumption, it must be noted that there is discrepancy among the three most widely used curves for the quartz-water fractionation (Clayton and others, 1972, Bottinga and Javoy, 1973). Figure 18 shows the three quartz-calcite fractionation curves calculated from these quartz-water curves and the currently accepted calcite-water fractionation curve (O'Neil and others, 1969). At 250°C, the expected fractionation of oxygen isotopes between quartz and calcite is either 2.19‰ (curve A_1), 3.05‰ (curve A_2), or 4.02‰ (curve B). All of the curves give positive values for the fractionation factors, meaning that the oxygen isotope values of quartz should be more positive than those for carbonate if the two minerals grew in isotopic equilibrium. However, the measured fractionations between the analyzed quartz-carbonate pairs are -3.5‰ (PMB-KA), -3.63‰

Figure 18. Plot of calculated quartz-calcite oxygen isotope fractionation curves based on three different models for the quartz-water fractionation. Calcite-water fractionation from O'Neil and others (1969). Quartz-water fractionation from Clayton and others (1972) (curves A_1 and A_2) and from Bottinga and Javoy (1973) (curve B; the value used in this study). Note that $\delta^{18}O_{quartz} - \delta^{18}O_{calcite} = 1000 \ln\alpha_{quartz\text{-}calcite}$, where $\alpha_{quartz\text{-}calcite}$ is the fractionation factor.

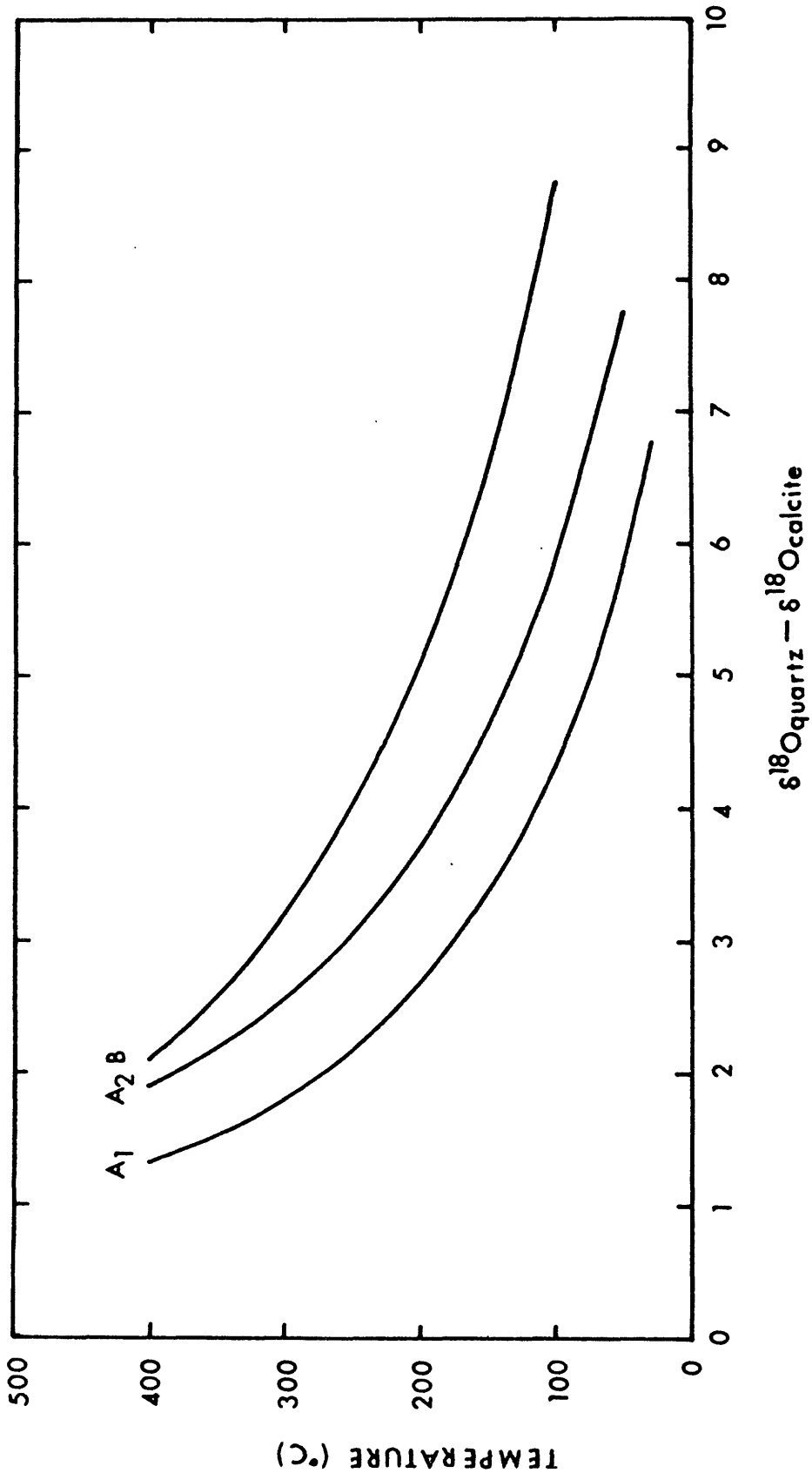
TEMPERATURE (°C)
500
400
300
200
100
0
0
1
2
3
4
5
6
7
8
9
10
$\delta^{18}O_{quartz} - \delta^{18}O_{calcite}$
A_1
A_2 B

(PBB-145) and -6.24‰ (PBB-147). These values indicate that the quartzes and the carbonates did not grow in isotopic equilibrium and that, therefore, the quartzes and the carbonates must have been deposited from different fluids.

The oxygen isotope and deuterium values of the waters in equilibrium with the carbonate minerals have been plotted on a $\delta^{18}O$-δD diagram (fig. 19) along with the isotope values from various other minerals from Creede (sphalerite, quartz, sericite, chlorite, adularia) (Robert O. Rye, written communication, 1976). The solid symbols denote samples for which both oxygen and deuterium were determined; open symbols represent samples for which only the oxygen isotopes have been analyzed. The carbonates appear to fall into a unique grouping in figure 19, located along the lower boundary of a box defining the typical range of isotope values for waters of deep-seated origin. The three light oxygen values in the carbonate group are enigmatic, but probably represent real values since the three samples are from three different vein systems and from both carbonate stages. The scatter could be due to variations in the temperature of deposition. The range of oxygen isotope and deuterium values for the carbonate waters at 250°C suggests that the carbonate fluids were either magmatic water or meteoric water which equilibrated with the country rock at near magmatic temperatures. Note that the quartz samples of the quartz-carbonate pairs are more enriched in ^{18}O (closer to the deep-seated water box) than almost all of the other quartz samples. The similarity in the oxygen isotope compositions between the two carbonate stages makes it unlikely that the CO_2 for the siderite came from leaching of the rhodochrosite by the dominantly meteoric ore fluids which characterized the quartz, sphalerite, sericite and chlorite. Had this been the case, the oxygen isotopes of the

Figure 19. $\delta^{18}O$- D plot of the hydrothermal fluids in equilibrium with the minerals during mineral deposition in the Creede mining district (temperature = 250°C). Solid symbols denote samples for which both $\delta^{18}O$ and δD have been analyzed; open symbols denote samples for which only $\delta^{18}O$ has been analyzed.

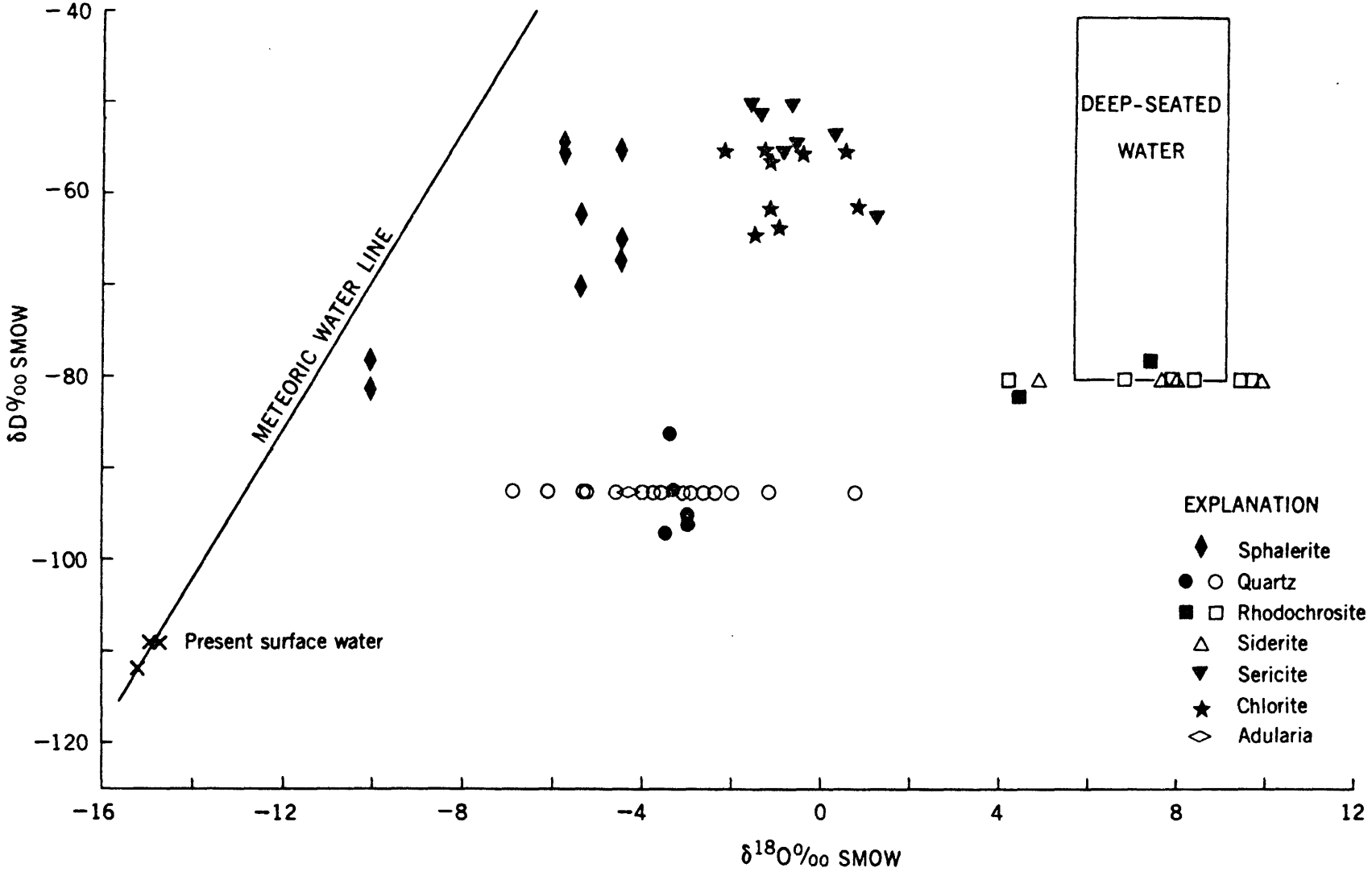
−40
−60
−80
−100
−120
δD‰ SMOW
METEORIC WATER LINE
Present surface water
DEEP-SEATED
WATER
EXPLANATION
Sphalerite
Quartz
Rhodochrosite
Siderite
Sericite
Chlorite
Adularia
−16
−12
−8
−4
0
4
8
12
δ18O‰ SMOW

siderite would surely be shifted towards the meteoric water line due to exchange with the transporting fluids.

It is possible that the quartz and carbonate could have been in isotopic equilibrium but that later re-equilibration at considerably lower temperatures (around 100°C) could have taken place. However, recrystallization textures have only been tentatively identified in the rhodochrosite stage and have not been seen in the perched-rhomb siderite stage. In addition, vugs in which the fluorite underlying the siderite was not leached must have been sealed off following Stage C deposition so that the siderite would not have had the opportunity to re-equilibrate with meteoric waters at lower temperatures. Several investigators have analyzed carbonates from other ore deposits such as Providencia, Mexico (Rye, 1966), the Bluebell mine, British Columbia (Ohmoto and Rye, 1970) and Casapalca, Peru (Rye and Sawkins, 1974) and have not reported any post-depositional re-equilibration; however, they do report predominantly deep-seated sources for the carbonates.

$\delta^{13}C$ values of the carbonate minerals range from -4.0‰ to -8.2‰ (fig. 20 and table 5) and also imply a deep-seated source for the solutions which deposited the carbonate. These values suggest that the source of carbon is either the mantle, a large volume of homogenized crustal carbon or, less likely, a carbonatite complex. Also plotted in fig. 20 are three isotopic analyses of the earlier travertine of the Creede Formation, located on the periphery of the Creede caldera. The striking isotopic difference between this carbonate and the vein carbonate indicates two different sources for the carbonates. The very different trace- and minor-element contents of the travertines as compared with the vein carbonates are also consistent with two different sources. Steven and Friedman (1968) suggest that the travertine may have been deposited from meteoric waters at

Figure 20. $\delta^{13}C$-$\delta^{18}O$ plot of the Creede carbonates (solid circles) and of the travertine (solid squares) from the Creede Formation. Travertine data from Steven and Friedman (1968).

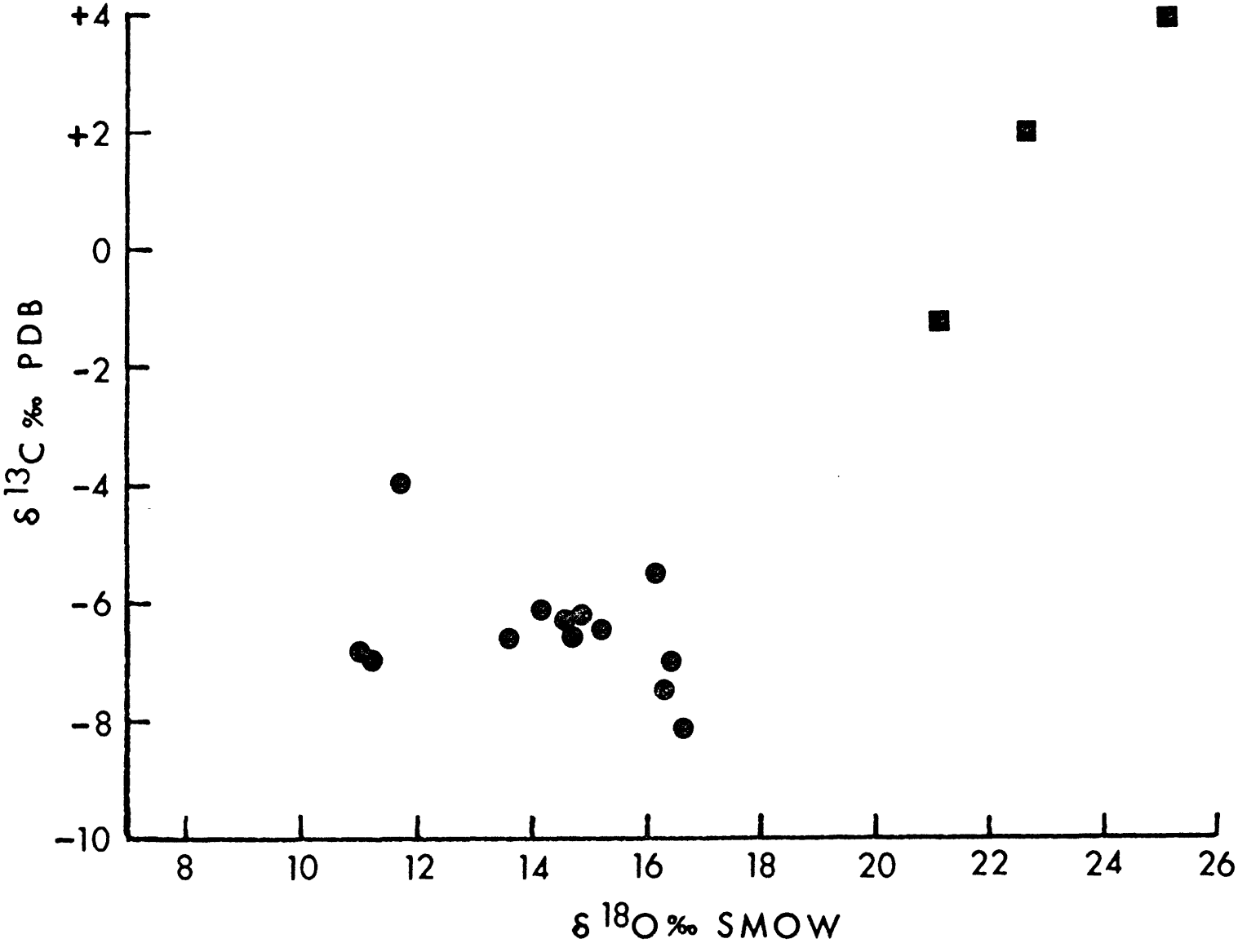
+4
+2
0
-2
-4
-6
-8
-10
δ 13C ‰ PDB
8
10
12
14
16
18
20
22
24
26
δ 18O ‰ SMOW

low temperature from a sedimentary source; as noted earlier, it is just possible that both carbonate and evaporate units of Mesozoic age underlie the Creede district.

Geochemical Environment During Carbonate Deposition

The mineral assemblages in ore deposits are the legacy of conditions that once existed. In a sense, they are akin to the punch line of a story when the rest of the story has been lost. Just as the general gist of the story can sometimes be deduced from the punchline, the conditions of deposition and the composition of the ore solution can frequently be delimited from the compositions and particular association of the minerals precipitated. In neither the story nor the ore deposit do the deductions represent an absolute truth, however, and — as has been suggested by Krauskopf (1968) — it is unlikely that the finest details can ever be worked out.

In order to use the precipitated minerals as evidence of the environment of deposition, the basic assumption must be made that the minerals precipitated were more or less in equilibrium with the depositing fluids. With respect to the Creede carbonates, the alternate leaching and deposition, especially of the rhodochrosite stage, implies that conditions at least bracketed equilibrium. Another important assumption is that no post-depositional changes have taken place. The presence of mineral zoning attests to the fluctuations in the composition of the hydrothermal solutions, to the lack of subsequent internal homogenization and to the lack of other post-depositional changes. The Creede carbonates show significant compositional variation and some zoning, although the zoning is difficult to document due to the complex textures and to the near absence of visual aids. The intricate patchy nature of the iron and manganese distribution in the

carbonate demonstrates that diffusion of ions was not particularly effective within the buried carbonate layers and that post-depositional changes have been few. The precipitating carbonate was in all likelihood at least in surface equilibrium with the depositing solutions. Barton and others (1963) discuss in some detail the problems of discerning equilibrium in ore deposits.

Many variables influence the precipitation and compositional variation of minerals. Some of the more important variables with respect to ore deposits include pH, temperature, pressure, and the fugacities and species concentrations in solution. In this study, both temperature and pressure can be fairly well delimited. A temperature of 250°C has been chosen based on fluid inclusion studies, mostly of the later coarser-grained ore generation (Stage D), (Barton and others, 1977). Fluid-inclusion studies also showed that the ore fluids were boiling at times, suggesting a maximum pressure of approximately 50 bars (the pressure at which 1 molal NaCl boils at 270°C, the maximum temperature from fluid inclusions (Haas, 1971)).

Barton and others (1977) used phase equilibria and thermodynamic data to establish limitations on the geochemical environment during ore deposition along the OH vein. Table 6 lists the values chosen for the parameters necessary to define a reference environment of ore deposition and also shows the sources for the data. The reference environment refers to the most typical environment in which the characteristic OH vein mineral assemblage of galena + sphalerite (with 1 or 2 mole % FeS) + chalcopyrite + pyrite + hematite + chlorite + quartz would have formed. The stability fields of the minerals pertinent to the Creede ore deposit are shown in figure 21a. Note that the field of iron-rich chlorite, which is ubiquitous along the OH vein, usurps the field of magnetite, which is absent at Creede.

TABLE 6. General Environmental Parameters for the OH Vein (From Barton and others, 1977).

Parameter	Range observed	Value chosen for Reference Environment	Source of Information
Temperature	190-268°C	250°C	fluid inclusions[1]
Pressure	40-50 bars	50 bars	evidence of boiling in fluid inclusions
Depth	500-600 metres	500 metres	estimated from pressure
Salinity	4 to 12 weight percent	6 weight percent 1 molal	analyses of fluid inclusions
Cl	0.92-1.86 molal	1 molal	analyses of fluid inclusions
Na/K	7.4-9.9 molal	9 molal	analyses of fluid inclusions
Total S	0.018-0.30 molal	0.06 weight percent[2] 0.02 molal	analyses of fluid inclusions
pH	--	5.4	calculated[3]

[1]Most of the fluid inclusion evidence is from the later half of the mineralization which is much coarser-grained.

[2]Because of the problem of sulfur contributed by oxidation of sulfides during sample handling, the lower total sulfur values are considered more reliable.

[3]The common occurrence of nearly fresh sanidine in the wallrock immediately adjacent to mineralization and numerous occurrences of adularia in sulfide-bearing vein filling throughout the OH vein strongly suggest that potash feldspar was indeed stable in the ore-forming environment. Minor amounts of sericite are found with the feldspar (though the nature of the distribution of sericite makes its paragenesis somewhat ambiguous) and quartz is nearly ubiquitous; thus the potassium content of the ore fluid can be put into the feldspar hydrolysis reaction to determine that the pH was 5.41, not far from neutral at 250°C (Montoya and Hemley, 1975).

Figure 21. A) Log a_{S_2} - log a_{O_2} diagram showing the stability fields of minerals pertinent to ore deposition on the OH vein. Temperature used is 250°C. The entire magnetite field is usurped by the chlorite field (shaded). The pyrrhotite-pyrite boundary is the same as the contour for 20 mole % FeS in sphalerite. Quartz is present throughout the diagram. From Barton and others (1977).

Abbreviations: py = pyrite, ccp = chalcopyrite, bn = bornite, hem = hematite, chl = chlorite.

B) Log a_{S_2} - log a_{O_2} diagram showing the pertinent field for mineralization on the OH vein (temperature = 250°C; pH = 5.4). Heavy lines show boundaries between pyrite, pyrrhotite, chlorite, and hematite (see fig. 21A). 'A' represents the reference environment for conditions during mainstage ore deposition; 'F' represents the limit of transgressions by the ore solutions down the chlorite-pyrite buffer; other environments noted in the diagram are not pertinent to this paper. Excursions into the finely dotted areas are forbidden by the absence of pyrrhotite or bornite, or by a total concentration of sulfur in solution greater than 1 mole per kilogram. The coarsely dotted areas are unlikely environments due to a total concentration of sulfur in solution from 0.1 to 1 mole per kilogram. From Barton and others (1977).

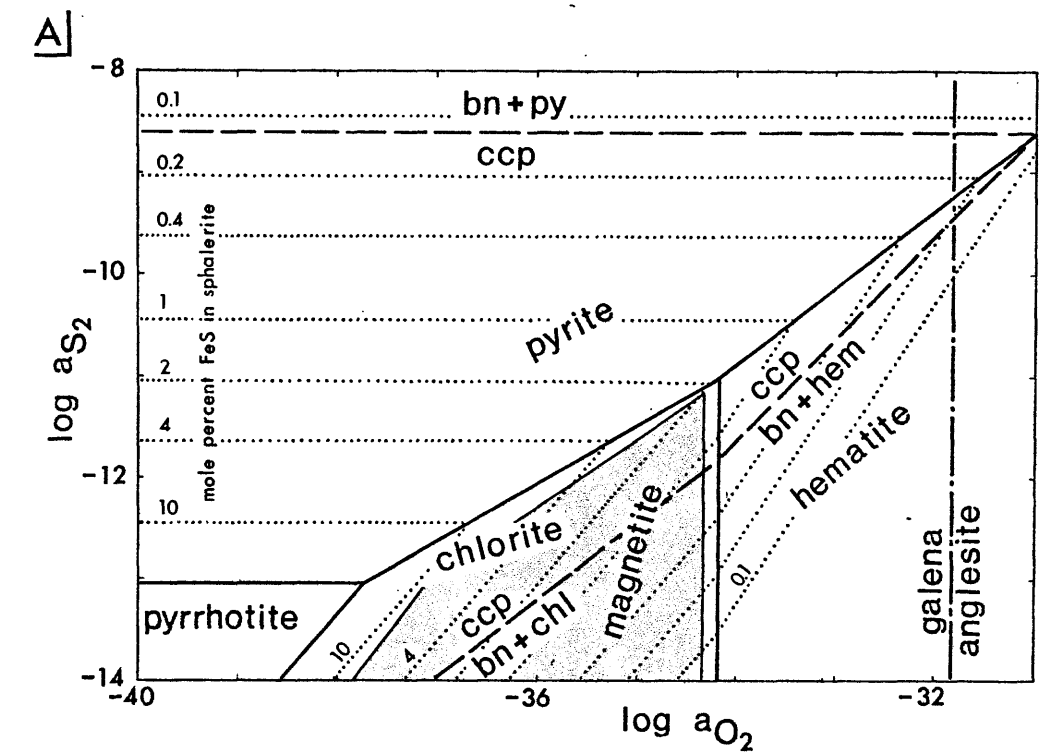
A
-8
-10
-12
-14
log a_{S_2}
0.1
0.2
0.4
1
2
4
10
mole percent FeS in sphalerite
bn + py
ccp
pyrite
chlorite
ccp
bn + chl
magnetite
ccp
bn + hem
hematite
galena
anglesite
pyrrhotite
10
4
0.1
-40
-36
-32
log a_{O_2}

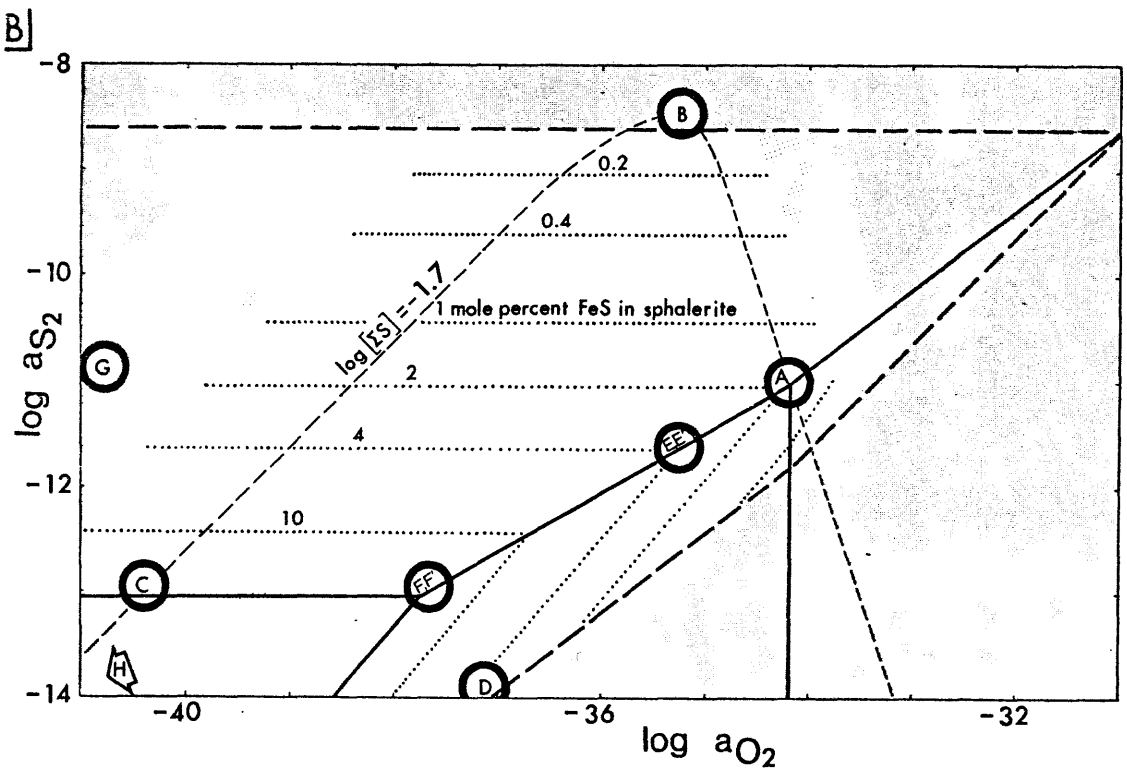
B
-8
-10
-12
-14
log a_{S_2}
B
0.2
0.4
log [Fs] = -1.7
1 mole percent FeS in sphalerite
2
4
10
G
A
EE
C
FF
H
D
-40
-36
-32
log a_{O_2}

Figure 21. (continued)

C) Log a_{S_2} - log a_{O_2} diagram showing the stability fields of pertinent manganese and barium minerals at 250°C and pH = 5.4 superimposed on the essential features of figure 21B. Mn_2O_3 falls outside of the plotted field.

——— rhodochrosite field when P_{CO_2} = 50 bars;

-·-·-·- rhodochrosite field when P_{CO_2} = 2 bars;

— — boundary between barite and witherite when P_{CO_2} = 50 bars;

- - - - - - boundary between barite and witherite when P_{CO_2} = 2 bars.

D) Log a_{S_2} - log a_{O_2} diagram showing the stability fields of pertinent iron and barium minerals at 250°C and pH = 5.4 superimposed on the essential features of figure 21B. The dashed pattern shows the siderite field when P_{CO_2} = 50 bars.

C

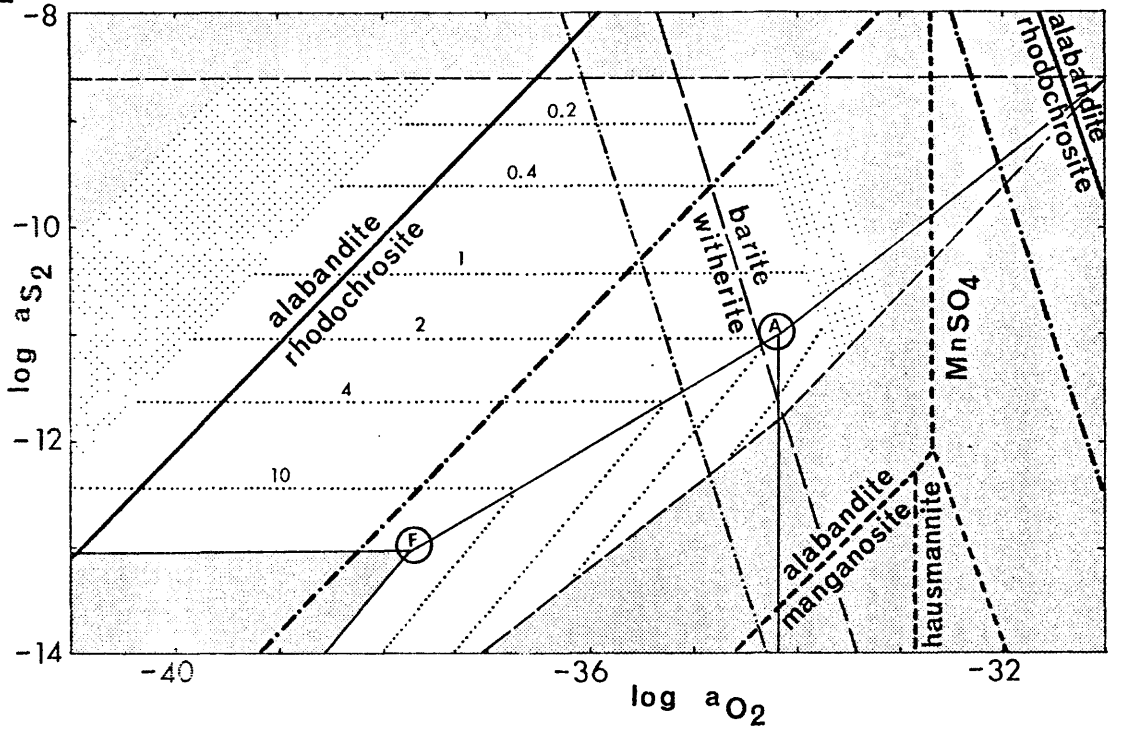
-8
-10
-12
-14
log a_{S_2}
-40
-36
-32
log a_{O_2}
0.2
0.4
1
2
4
10
alabandite
rhodochrosite
barite
witherite
alabandite
manganosite
hausmannite
$MnSO_4$
alabandite
rhodochrosite
A
F

D

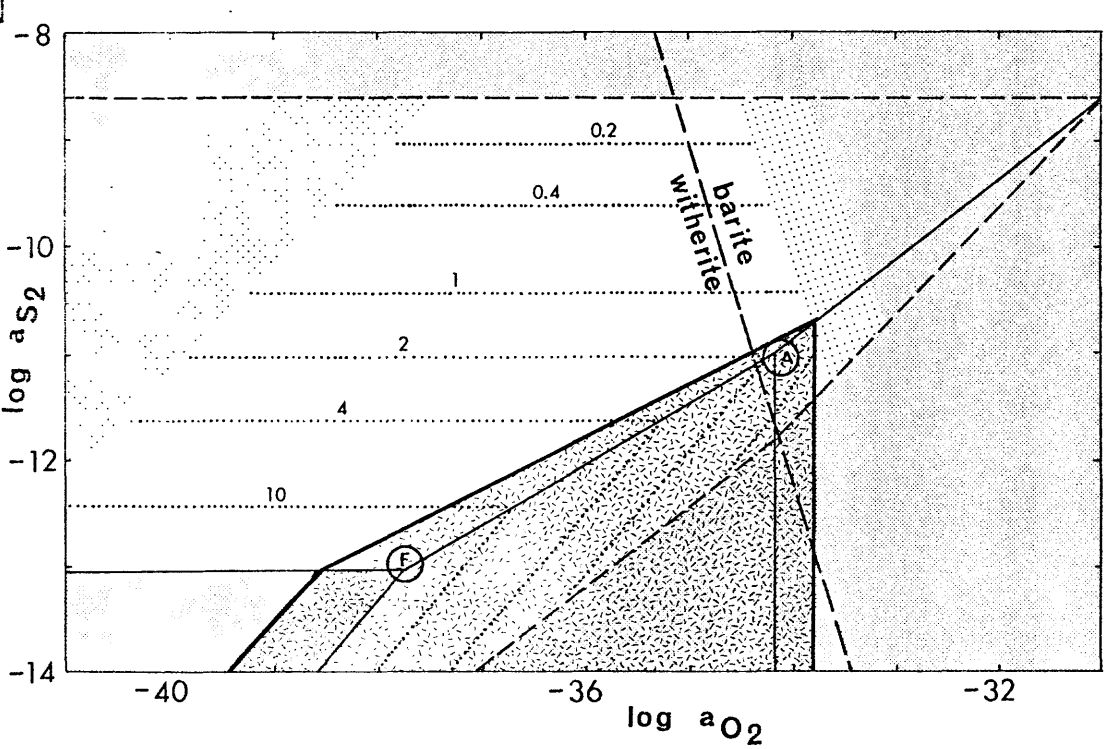
-8
-10
-12
-14
log a_{S_2}
-40
-36
-32
log a_{O_2}
0.2
0.4
1
2
4
10
barite
witherite
A
F

Figure 21b shows the more limited region of interest for mineralization. Mineralization could not have taken place in the finely dotted areas because of the presence of pyrite, hematite and chalcopyrite coupled with the absence of bornite and pyrrhotite at Creede, and/or because of a concentration of total sulfur in solution greater than 1 mole/kg. Concentrations of total sulfur greater than 1 mole/kg would cause larger freezing point depressions of fluid inclusion liquids than observed (Barton and others, 1977). A range of total concentration of sulfur in solution of 0.1 to 1 mole/kg is also unlikely and is shown by the coarsely dotted pattern in figure 21b. The reference environment for ore deposition is denoted by the symbol 'A' at the chlorite-hematite-pyrite triple point. Variations in the oxidation and sulfidation states in the OH vein fluids have been recorded by iron fluctuations in the sphalerite (containing from 0.1 to 20 mole % FeS); the high-iron fluctuations can be explained by excursions along the chlorite + pyrite buffer curve between the reference environment 'A' to environment 'F' (fig. 21b).

To determine whether conditions during carbonate deposition were compatible with the reference environment, 'A', for main-stage ore deposition, diagrams similar to that of figure 21b have been constructed for minerals pertinent to the two carbonate generations. Figure 21c shows the mineral stability fields at 250°C for manganese oxides, sulfide, sulfate and carbonate and for barite and witherite. Figure 21d shows the mineral stability fields for iron oxide, sulfides and carbonate and for iron-rich chlorite. These diagrams were constructed using the procedure described by Holland (1959; 1965). Sources of the mineral data used are listed in table 7.

Calculations indicate that the dominant species of carbon is CO_2 rather

TABLE 7. Thermodynamic data, and their sources, used in constructing figures 21c and 21d.

Reaction	ΔG° at 250°C (kjoule)	Source
Manganese		
$Mn + 1/2\ O_2 \rightarrow MnO$	-346.219	Robie and others (in press)
$Mn + 1/2\ S_2 \rightarrow MnS$	-243.042	" " " "
$3Mn + 2\ O_2 \rightarrow Mn_3O_4$	-1203.206	" " " "
$Mn + 1/2\ S_2 + 2\ O_2 \rightarrow MnSO_4$	-899.032	" " " "
$Mn + C + 3/2\ O_2 \rightarrow MnCO_3$	-761.261	" " " "
$Mn + Si + 3/2\ O_2 \rightarrow MnSiO_3$	-1184.339	" " " "
Iron		
$Fe + 1/2\ S_2 \rightarrow FeS$	-126.775	Barton and others (1977)
$Fe + S_2 \rightarrow FeS_2$	-194.592	Robie and others (in press)
$2Fe + 3/2\ O_2 \rightarrow Fe_2O_3$	-939.057	Haas and Robie (1973)
$3Fe + 2\ O_2 \rightarrow Fe_3O_4$	-683.373	" " "
$Fe + C + 3/2\ O_2 \rightarrow FeCO_3$	-635.008	Wetlaufer (this study)
Miscellaneous Gases		
$C + O_2 \rightarrow CO_2$	-394.925	Robie and others (in press)
$2S \rightarrow S_2$	+46.195	" " " "
$H_2 + 1/2\ O_2 \rightarrow H_2O$	-217.882	" " " "
$H_2O_{liquid} \rightarrow H_2O_{gas}$	-15.32	Haas (1970)
$C + 2H_2 \rightarrow CH_4$	-30.340	Robie and others (in press)
$C + 1/2\ O_2 \rightarrow CO$	-157.436	Robie and others (in press)
$H_2 + 1/2\ S_2 \rightarrow H_2S$	-40.57	" " " "
Miscellaneous Minerals		
$Si + O_2 \rightarrow SiO_2$	-815.215	Robie and others (in press)
$Ba + 1/2\ S_2 + 2\ O_2 \rightarrow BaSO_4$	-1300.065	" " " "
$Ba + C + 3/2\ O_2 \rightarrow BaCO_3$	-1107.112	" " " "
$Zn + 1/2\ S_2 \rightarrow ZnS$	-221.424	" " " "
$Zn + C + 3/2\ O_2 \rightarrow ZnCO_3$	-670.046	Robie and Waldbaum (1968)
$PB + 1/2\ S_2 \rightarrow PbS$	-116.874	" " " "
$Pb + C + 3/2\ O_2 \rightarrow PbCO_3$	-573.342	" " " "
$6.36H_2 + 12Fe + 8Si + 18O_2 \rightarrow H_{12.73}Fe_{12}Si_8O_{36}$	-11,171.280[1]	Barton and others (1977)

[1]Calculated from the chlorite-hematite buffer reaction with log a_{O_2} = -34.2 (Creede reference environment). Corrected from Barton and others (1977).

than CO, CH_4 or HCO_3^-. The possible range of carbon dioxide pressures was delimited by taking a maximum of 50 bars (see table 6) and by taking a minimum based on the reaction

$$MnSiO_3 + CO_2 \rightleftarrows MnCO_3 + SiO_2.$$

The rhodochrosite at Creede is stable with quartz (the system is quartz saturated) and no pyroxmanganite ($MnSiO_3$) has been identified at Creede. Therefore, the minimum CO_2 pressure was calculated for which rhodochrosite was stable with respect to pyroxmanganite ($\log CO_2 = .295$, or roughly 2 bars). It is assumed that this minimum can also be applied to the siderite stage because manganese silicate never appears to have formed on exposed rhodochrosite surfaces, some of which must have been at times in contact with the fluids depositing the siderite.

Figure 21c shows that at all CO_2 pressures reasonable during rhodochrosite deposition, the rhodochrosite field preempts the manganosite (MnO) field. This situation is consistent with the absence of primary manganese oxides at Creede; some secondary manganese oxides are present due to alteration of rhodochrosite. The rhodochrosite field also encompasses the reference environment, 'A', indicating that conditions during rhodochrosite deposition would have been compatible with those during main-stage ore deposition. The barite and witherite field boundary has also been plotted at maximum and minimum CO_2 pressures. The intimate presence of rhodochrosite with barite indicates that they are stable together even though they did not co-precipitate. The limitations on the barite field suggests that although conditions during the rhodochrosite and barite stage were compatible with environment 'A', they were not compatible with the brief excursions during main-stage ore deposition to environment F.

The low iron content of the sphalerite disseminated in the rhodochrosite

supports the implication that rhodochrosite deposition would not have taken place near environment F (where iron content in sphalerite should be 20 mole %). Electron microprobe analyses of the sphalerite in 3 rhodochrosite sample localities show up to 3 mole % FeS (mean of 0.4 mole %), up to 2.6 mole % MnS (mean of 0.6 mole %) and from 0 to 4.5 mole % CdS. There appears to have been no significant post-depositional interchange of elements between the rhodochrosite and the sphalerite.

The proximity of the barite-witherite transition to the reference environment suggests that a closer look should be taken for the presence of witherite and at the barium contents of the rhodochrosite. Semi-quantitative analyses of the rhodochrosite (table 3) do show up to 0.12 weight % barium.

Calculations on the stability of the zinc and lead carbonates with respect to sphalerite and galena show that the pure carbonates are unstable at 250° at such low CO_2 pressures. Nevertheless, small amounts of zinc and lead in the rhodochrosite were detected by electron microprobe and by semi-quantitative analyses. If a good thermodynamic model of the $ZnCO_3$-$MnCO_3$ solid solution were available, an estimate of the activity of the $ZnCO_3$ in the rhodochrosite at Creede could be made and used in further defining the CO_2 pressure. Shikazono (1977) was able to use the zinc contents of siderites coexisting with sphalerite from two Japanese ore deposits to evaluate the redox conditions under which they precipitated.

Constructing a log a_{S_2} - log a_{O_2} diagram pertinent to the late-stage carbonate is somewhat more complicated for the early-stage carbonate because the most recent thermochemical data in the literature predict too low a stability for siderite, even for the maximum CO_2 pressure at Creede. That is, the existing thermochemical data deny the textural relations at Creede that indicate that the assemblage hematite + siderite is stable at 250°C

and 50 bars total pressure.

Based on the siderite-hematite assemblage at Creede, the range for a new free energy of formation of siderite at 250° has been calculated (ΔG_f° = -635 to -649 kjoule). The limiting values were calculated from the equation

$$2FeCO_3 + 1/2\ O_2 \rightleftarrows Fe_2O_3 + CO_2$$

assuming respective CO_2 pressures of 50 bars and of 2 bars and a log a_{O_2} of -33.78. This oxygen value was chosen because it represents the maximum oxygen fugacity at which the siderite + hematite assemblage would be stable where total concentration of sulfur is less than 0.1 mole/kg (table 6, figure 21b). The iron content of coexisting sphalerite should be low at this oxygen fugacity (approximately 1.5 mole % FeS). Siderite does not appear to have precipitated simultaneously with sphalerite (or any sulfides), but its precipitation on unleached low-iron sphalerite (ER-119) indicates that low-iron sphalerite was stable with respect to the carbonate fluids. Table 8 shows the variations among the most recent predicted free energies of siderite at 250°C in the literature. The value for the free energy of siderite derived by French (1971) from measurements of the magnetite-hematite and graphite buffers comes the closest to agreeing with the stability suggested by the textural relations at Creede. French's free energy of formation of siderite is about 14 kjoule (3 kcal) lower than that suggested by the Creede assemblage, assuming the maximum CO_2 pressure, which is well within the limits of uncertainty in French's experimental data.

The siderite field as plotted in figure 21d uses the value of ΔG_f° = -635 kjoule for siderite formation since it is closest to French's free energy value. The environment of deposition of siderite + hematite

TABLE 8. Most recent proposed free energies of formation of siderite at 250°C.

Source	ΔG° at 250°C (kjoule)
Robie and Waldbaum (1968) for S° Wagman and others (1969) for ΔH_{298}	-615
French (1971)	-620[1]
Wetlaufer (this study)	-635 (to -649)

[1]Corrected for more recent magnetite data (Haas and Robie, 1973).

is fairly well delimited in figure 21d. The range of a_{S_2} is limited by the absence of pyrite with the siderite (although siderite is seen in contact with pyrite so that these minerals could not have been too far out of equilibrium) and by the absence of bornite. The range of a_{O_2} is limited by the siderite-hematite boundary (which has been defined at log a_{O_2} = -33.78 due to the limitations of the total concentration of sulfur in solution (see figure 21b and table 6) and by the chlorite-hematite boundary.

The siderite-chlorite textural relations indicate that proximity of the siderite-hematite boundary to the chlorite-hematite boundary is both reasonable and probably necessary. There is no textural evidence for the coprecipitation of chlorite and siderite, and nor is there any indication of chlorite altering to siderite or visa versa. However, siderite must have been more or less stable in the presence of chlorite because chlorite was abundant before and after Stage C deposition. Therefore, whereas the siderite field must be larger than the chlorite field in figure 21d to permit siderite deposition without chlorite deposition, it cannot be too much larger or the siderite might not be stable in the presence of chlorite.

Any physico-chemical change which expands the siderite field to a size larger than that of the chlorite field will favor siderite deposition. The most likely factor is an increase in the total carbon in the hydrothermal system. This increase could easily be brought about by injection of a pulse of deep-seated, or magmatic, fluids, which is consistent with the source of the carbon and oxygen for the carbonates as indicated by the isotopic analyses. The volumetric and spatial restrictions of this carbonate stage suggest that the magmatic spurt was not large nor extended in time. Addition of only a relatively small amount of carbon is necessary since small changes in CO_2 pressure have a large effect on the size of the

siderite field (e.g., a 10 bar decrease in CO_2 pressure would shrink the siderite field as plotted in figure 21d at 50 bars pressure so that chlorite would become the stable phase).

Several factors, such as temperature, pH, and P_{CO_2} changes, may have caused siderite precipitation once the physico-chemical environment was within the siderite stability field. Temperature changes are probably not a deciding factor for siderite deposition because the temperature fluctuated considerably prior to siderite deposition (e.g., over a 60°C range during deposition of the underlying fluorite) without siderite deposition. An increase in pH would cause siderite deposition but would also cause the simultaneous precipitation of sulfides. Siderite rhombs are found overlying unetched sphalerite indicating that the fluids were saturated with respect to sphalerite. However, siderite and sulfides are never found intergrown, suggesting that pH changes were not an important factor. An increase in total CO_2, besides making siderite stable over chlorite, would cause siderite precipitation. A small influx of magmatic fluids rich in CO_2 seems the most probable cause of siderite deposition and is consistent with the isotopic evidence suggesting different sources for the sulfide and carbonate fluids.

Conditions during rhodochrosite deposition were probably very similar to those during siderite deposition, the main discriminator between the two carbonates being only the Fe/Mn ratio. The similarity among the carbon and oxygen isotopes of the carbonates also suggests similar conditions of deposition for both carbonate stages.

IV. CONTINUING STUDIES

Many aspects of the carbonate minerals at Creede remain to be investigated. Of these, the more important are noted below. Study of the fluid inclusions in the carbonate is necessary to provide a more accurate temperature (or range of temperatures) of deposition for the carbonate stages. Fluid inclusions may also give some clues with respect to the possibility of recrystallization in the early-stage carbonate. Freezing studies of fluid inclusions will define the salinity and CO_2 concentration of the depositing fluids.

Additional mineralogical studies of the carbonates and of the minerals associated with the carbonates will also contribute to a better understanding of the role of the carbonates at Creede. The lead, zinc, barium and strontium contents in the carbonate and in the barite must be evaluated. In addition, examination of both the siderite and the rhodochrosite by transmission electron microscopy should provide some insight into the frequently patchy nature of the compositional variations. The manganese variations in the chlorite are particularly important because the chlorite appears to have been the only other primary manganese-bearing phase in the Creede ore deposit. Detailed mineralogical study of the barite associated with the rhodochrosite (and with the one siderite locality, PBB-159) will help to define the geochemical conditions during carbonate deposition.

A look at the lead and strontium isotopes of the carbonates, barite, sericite, and adularia at Creede will aid in sorting out the diverse sources that the oxygen, hydrogen and carbon isotopes suggest. Rare earth contents

should also be evaluated with respect to possible sources of the fluids. Sulfur isotope and minor-element studies of the sulfides encased in the rhodochrosite will also help to define respectively the source and the environment of deposition for the carbonate.

V. SUMMARY

The carbonates at Creede are limited to two stages in the paragenesis. An early carbonate was deposited prior to the main ore deposition and a later carbonate was deposited during a major break in ore deposition. The early manganese-rich carbonate is far more significant volumetrically (by a factor of 10^3 to 10^4) than the later iron-rich carbonate. Both stages are limited spatially, the rhodochrosite restricted generally in the southern third of the vein system and the siderite-manganosiderite stage predominating in the northern two-thirds of the vein system. The similarity between the rhodochrosite along the Bulldog vein and that along the southern Amethyst suggests that these veins were open at the same time and saw similar fluids. Compositional variations within each carbonate stage appear to be so complex that neither temporal nor spatial significance can be extracted.

Consideration of thermochemical data shows that conditions for deposition of rhodochrosite were compatible with the reference environment proposed by Barton and others (1977) for main-stage mineralization. Conditions for deposition of siderite need not have been very different from those of the reference environment. In each case, only a slight increase in CO_2 probably brought about carbonate deposition. A number of assumptions have been made in order to compare the stability fields on f_{S_2} - f_{O_2} diagrams of the carbonates with those of the ore minerals. First, the CO_2 pressure has been limited between 2 and 50 bars based respectively on the absence of manganese silicates and on temperature and salinity measurements of fluid

inclusions and the observation that some of them show evidence of boiling. Second, it has been assumed that the temperature of deposition remained fairly uniform at around 250°C during carbonate deposition. Third, a new free energy of formation was calculated for siderite as defined by the mineral assemblage seen at Creede because the available thermochemical data predict too small a stability field for siderite under the above conditions; the new free energy value falls within the experimental error of the most reliable recent data (French, 1971).

The carbon and oxygen isotopic compositions of the rhodochrosite and the siderite are very similar, suggesting a similar origin from a deep-seated source. The isotopes of the carbonates are decidedly different from those of the main ore-bearing fluids, which appear to have been of meteoric origin.

This paper proposes that each period of carbonate deposition was brought about by an influx of carbon due to the introduction of magmatic fluids. The early-stage carbonate was probably deposited during the initial burst of magmatic fluids from the buried pluton proposed by Steven and Eaton (1975). As the circulating hydrothermal system matured, it became dominated by lighter meteoric waters from which the early fine-grained ore was deposited. The late-stage carbonate precipitation was probably caused by a final spurt of magmatic fluid from the pluton. The limited distribution and volume of the siderite suggest that the spurt was both brief and local. The higher-iron contents of the late-stage carbonate probably resulted from the presence of the pyrite-chlorite buffer, which was not present during early-stage carbonate deposition. Subsequent to siderite deposition, the heat from the pluton continued to drive the hydrothermal circulating system, again dominantly charged by meteoric waters, which

deposited the coarser-grained ore stage. The importance of the carbonates to the Creede study lies in the fact that they provide the only unequivocal evidence of deep-seated, probably magmatic, contributions to the Creede ore-forming system.

APPENDIX

SAMPLE	$CaCO_3$	$MnCO_3$	$FeCO_3$	$MgCO_3$	SAMPLE	$CaCO_3$	$MnCO_3$	$FeCO_3$	$MgCO_3$
	BULLDOG VEIN					0.133	0.694	0.149	0.022
						0.121	0.723	0.133	0.021
PHW-L-20A-75	0.055	0.838	0.102	0.003		0.143	0.689	0.141	0.023
	0.046	0.844	0.102	0.006		0.141	0.693	0.143	0.023
	0.052	0.808	0.126	0.013		0.141	0.701	0.132	0.024
						0.113	0.681	0.183	0.021
PMB-JX-538-71	0.022	0.860	0.103	0.011		0.138	0.633	0.188	0.038
	0.029	0.863	0.094	0.012		0.112	0.715	0.146	0.025
	0.030	0.857	0.103	0.009		0.136	0.573	0.248	0.042
	0.035	0.868	0.087	0.008		0.131	0.703	0.145	0.020
	0.023	0.874	0.092	0.007		0.145	0.438	0.387	0.029
	0.039	0.850	0.098	0.011		0.134	0.568	0.262	0.035
	0.039	0.849	0.100	0.009		0.121	0.676	0.168	0.033
	0.039	0.855	0.096	0.007		0.152	0.643	0.170	0.032
	0.032	0.861	0.097	0.007		0.120	0.656	0.187	0.034
PMB-KA-542-71	0.018	0.863	0.110	0.007	PMB-GC-338-68	0.084	0.852	0.050	0.012
	0.035	0.854	0.098	0.010		0.038	0.887	0.061	0.013
	0.025	0.878	0.085	0.008		0.031	0.906	0.053	0.009
	0.037	0.869	0.083	0.009		0.029	0.904	0.059	0.006
	0.024	0.899	0.069	0.006		0.041	0.890	0.061	0.006
	0.042	0.874	0.073	0.009		0.036	0.899	0.059	0.005
	0.027	0.869	0.094	0.008		0.043	0.737	0.204	0.013
	0.030	0.887	0.074	0.007		0.030	0.770	0.180	0.019
	0.024	0.869	0.098	0.007		0.024	0.916	0.055	0.004
	0.035	0.867	0.088	0.009		0.060	0.867	0.060	0.011
DH-23	0.080	0.481	0.418	0.018	PBB-147-50-74	0.061	0.893	0.040	0.003
	0.124	0.571	0.260	0.042		0.039	0.908	0.044	0.007
	0.125	0.716	0.136	0.021		0.050	0.884	0.054	0.009
	0.140	0.655	0.168	0.035		0.140	0.655	0.168	0.035

SAMPLE	$CaCO_3$	$MnCO_3$	$FeCO_3$	$MgCO_3$
	0.034	0.897	0.059	0.009
	0.037	0.909	0.048	0.005
	0.024	0.927	0.045	0.002
	0.470	0.337	0.032	0.160
	0.688	0.245	0.013	0.053
	0.721	0.213	0.006	0.059
	0.734	0.257	0.002	0.004
	0.205	0.614	0.073	0.105
	0.204	0.636	0.074	0.083
	0.306	0.646	0.037	0.010
	0.032	0.851	0.109	0.006
	0.048	0.758	0.162	0.030
	0.023	0.906	0.066	0.003
PBB-143-27-74	0.041	0.825	0.125	0.008
	0.025	0.906	0.065	0.002
	0.026	0.877	0.091	0.002
	0.032	0.880	0.082	0.004
	0.025	0.881	0.088	0.004
	0.028	0.879	0.085	0.005
	0.034	0.875	0.085	0.003
	0.027	0.880	0.086	0.004
	0.023	0.898	0.073	0.003
PMB-MP-633-74	0.030	0.892	0.071	0.005
	0.034	0.875	0.079	0.010
	0.043	0.867	0.079	0.008
	0.025	0.880	0.078	0.015
	0.024	0.905	0.064	0.005
	0.025	0.911	0.059	0.004
	0.023	0.888	0.083	0.005
	0.032	0.873	0.084	0.010
PMB-MQ-643-74	0.025	0.897	0.069	0.007

SAMPLE	$CaCO_3$	$MnCO_3$	$FeCO_3$	$MgCO_3$
	0.056	0.842	0.074	0.025
	0.045	0.864	0.078	0.012
	0.024	0.918	0.052	0.004
	0.014	0.942	0.042	0.001
	0.017	0.924	0.055	0.002
	0.019	0.860	0.117	0.003
	0.018	0.922	0.056	0.002
	0.054	0.854	0.080	0.010
	0.037	0.796	0.136	0.030
	0.020	0.815	0.141	0.021
	0.062	0.861	0.069	0.005
	0.034	0.873	0.078	0.013
PMB-LN-594-74	0.014	0.927	0.055	0.002
	0.024	0.840	0.127	0.007
	0.018	0.875	0.096	0.010
	0.016	0.928	0.051	0.002
	0.019	0.860	0.110	0.008
	0.017	0.811	0.165	0.005
	0.021	0.929	0.047	0.001
	0.016	0.803	0.174	0.005
	0.037	0.761	0.186	0.015
	0.016	0.939	0.041	0.001
	0.017	0.936	0.043	0.001
	0.013	0.899	0.082	0.002
	0.025	0.904	0.068	0.002
PMB-NA-655-74	0.044	0.901	0.047	0.004
	0.041	0.874	0.074	0.009
	0.042	0.847	0.095	0.013
	0.043	0.860	0.079	0.015
	0.059	0.815	0.103	0.021
	0.041	0.858	0.085	0.013
	0.060	0.812	0.114	0.012

SAMPLE	$CaCO_3$	$MnCO_3$	$FeCO_3$	$MgCO_3$
	0.040	0.903	0.047	0.008
	0.043	0.872	0.076	0.007
	0.049	0.833	0.105	0.010
	0.052	0.831	0.103	0.012
	0.051	0.839	0.098	0.010
	0.028	0.883	0.081	0.006
	0.054	0.867	0.067	0.011
	0.085	0.780	0.120	0.013
	0.050	0.888	0.047	0.013
	0.073	0.861	0.052	0.012
	0.046	0.870	0.076	0.007
	0.052	0.851	0.087	0.007
	0.048	0.850	0.092	0.008
	0.087	0.710	0.179	0.021
	0.051	0.881	0.053	0.012
	0.068	0.770	0.150	0.011
	0.042	0.904	0.041	0.012
PMB-MJ-624-74	0.043	0.880	0.070	0.005
	0.040	0.893	0.060	0.005
	0.042	0.868	0.079	0.009
	0.040	0.856	0.082	0.020
	0.057	0.728	0.201	0.013
	0.025	0.738	0.221	0.016
	0.025	0.777	0.176	0.019
	0.040	0.854	0.089	0.015
	0.041	0.775	0.173	0.009
	0.046	0.868	0.073	0.011
	0.044	0.882	0.065	0.006
	0.050	0.705	0.229	0.013
	0.033	0.900	0.059	0.005
	0.127	0.587	0.259	0.024
	0.120	0.601	0.253	0.024
	0.063	0.764	0.160	0.012

SAMPLE	$CaCO_3$	$MnCO_3$	$FeCO_3$	$MgCO_3$
	0.149	0.639	0.169	0.040
	0.066	0.856	0.071	0.005
	0.040	0.722	0.222	0.015
	0.038	0.697	0.248	0.016
	0.025	0.785	0.167	0.021
	0.050	0.861	0.078	0.008
	0.048	0.701	0.235	0.015
	0.058	0.722	0.205	0.014
	0.028	0.899	0.066	0.004
	0.049	0.771	0.164	0.015
	0.028	0.859	0.095	0.015
	0.078	0.707	0.178	0.036
	0.036	0.881	0.075	0.007
	0.034	0.838	0.104	0.022
	0.040	0.895	0.058	0.005
	0.022	0.899	0.070	0.006
	0.036	0.720	0.225	0.018
	0.037	0.859	0.089	0.013
PMB-LP-596-74	0.049	0.784	0.153	0.012
	0.038	0.892	0.064	0.005
	0.022	0.908	0.064	0.005
	0.027	0.887	0.081	0.002
	0.072	0.792	0.121	0.013
	0.058	0.830	0.101	0.009
	0.060	0.862	0.070	0.006
	0.076	0.820	0.093	0.009
	0.055	0.860	0.080	0.004
	0.052	0.858	0.081	0.007
	0.041	0.811	0.127	0.018
	0.070	0.771	0.148	0.009
	0.042	0.848	0.104	0.005
	0.060	0.873	0.060	0.005

SAMPLE	$CaCO_3$	$MnCO_3$	$FeCO_3$	$MgCO_3$
PMB-NB-658-74	0.072	0.787	0.128	0.012
	0.074	0.786	0.126	0.011
	0.063	0.815	0.108	0.012
	0.071	0.784	0.131	0.012
	0.057	0.693	0.208	0.040
	0.048	0.702	0.230	0.017
	0.053	0.758	0.159	0.029
	0.063	0.775	0.152	0.008
	0.051	0.803	0.134	0.009
	0.048	0.799	0.143	0.009
	0.030	0.832	0.130	0.006
	0.045	0.746	0.187	0.021
	0.053	0.800	0.134	0.010
	0.050	0.779	0.160	0.009
	0.068	0.774	0.145	0.011
	0.044	0.806	0.140	0.008
	0.058	0.793	0.136	0.010
	0.079	0.780	0.120	0.020
	0.037	0.665	0.237	0.059
	0.066	0.738	0.172	0.022
	0.048	0.650	0.271	0.030
	0.048	0.879	0.061	0.009
	0.046	0.888	0.058	0.007
	0.038	0.895	0.062	0.004
	0.036	0.902	0.057	0.004
	0.077	0.858	0.051	0.012
	0.028	0.774	0.185	0.011
	0.045	0.802	0.135	0.017
	0.067	0.754	0.157	0.020
	0.022	0.862	0.101	0.012
	0.057	0.784	0.148	0.009
	0.036	0.902	0.056	0.004
	0.047	0.894	0.046	0.011
	0.047	0.881	0.061	0.009
	0.055	0.727	0.207	0.010
	0.035	0.909	0.052	0.002
	0.058	0.853	0.071	0.015
	0.062	0.875	0.054	0.007
	0.028	0.851	0.110	0.007
	0.038	0.797	0.151	0.012
	0.033	0.860	0.101	0.005
	0.025	0.852	0.111	0.009
	0.043	0.820	0.124	0.010
	0.053	0.807	0.127	0.011
	0.045	0.730	0.205	0.017
PMB-MZ-653-74	0.031	0.888	0.074	0.006
	0.070	0.760	0.142	0.025
	0.078	0.692	0.208	0.020
	0.072	0.755	0.136	0.036
	0.045	0.885	0.061	0.007
	0.039	0.907	0.047	0.005
	0.036	0.902	0.055	0.005
PMB-MY-652-74	0.037	0.909	0.050	0.002
	0.029	0.916	0.050	0.003
	0.040	0.908	0.048	0.002
	0.029	0.898	0.067	0.004
	0.043	0.902	0.049	0.003
	0.038	0.902	0.054	0.003
	0.051	0.902	0.041	0.003
	0.023	0.917	0.057	0.002
	0.029	0.879	0.078	0.013
	0.031	0.866	0.085	0.016
	0.015	0.915	0.067	0.001
	0.037	0.866	0.080	0.016
	0.018	0.923	0.056	0.001
	0.035	0.903	0.057	0.004

SAMPLE	$CaCO_3$	$MnCO_3$	$FeCO_3$	$MgCO_3$
	0.039	0.898	0.055	0.005
	0.050	0.896	0.044	0.006
	0.040	0.769	0.174	0.016
	0.057	0.893	0.044	0.005
	0.036	0.846	0.109	0.006
	0.052	0.907	0.037	0.001
	0.053	0.903	0.042	0.001
	0.057	0.891	0.047	0.002
	0.042	0.855	0.094	0.006
	0.045	0.897	0.051	0.003
PMB-MU-642-74	0.023	0.819	0.155	0.002
	0.026	0.894	0.072	0.006
	0.040	0.843	0.108	0.008
	0.028	0.880	0.078	0.013
	0.018	0.889	0.088	0.003
	0.032	0.863	0.092	0.011
	0.030	0.873	0.086	0.008
	0.024	0.873	0.095	0.005
	0.026	0.872	0.093	0.008
	0.030	0.867	0.092	0.008
	0.023	0.883	0.081	0.012
	0.031	0.870	0.091	0.006
	0.042	0.753	0.192	0.009
	0.037	0.858	0.094	0.008
	0.044	0.864	0.081	0.008
	0.032	0.864	0.092	0.009
	0.041	0.849	0.097	0.012
	0.048	0.844	0.101	0.005
	0.037	0.829	0.120	0.012
	0.029	0.884	0.074	0.010
PBB-145-36-74	0.094	0.682	0.218	0.003
	0.043	0.838	0.112	0.003

SAMPLE	$CaCO_3$	$MnCO_3$	$FeCO_3$	$MgCO_3$
	0.060	0.848	0.087	0.003
	0.044	0.820	0.130	0.004
	0.049	0.818	0.126	0.003
	0.039	0.853	0.105	0.002
	0.050	0.844	0.104	0.001
	0.059	0.834	0.099	0.005
	0.046	0.873	0.076	0.003
	0.055	0.860	0.077	0.007
	0.035	0.825	0.128	0.011
	0.039	0.892	0.062	0.005
PMB-KC-445-71	0.035	0.854	0.089	0.020
	0.014	0.838	0.118	0.027
	0.061	0.863	0.060	0.015
	0.070	0.856	0.055	0.016
	0.033	0.824	0.124	0.016
PBB-132-8-74	0.040	0.878	0.075	0.005
	0.033	0.880	0.080	0.004
	0.032	0.888	0.076	0.002
	0.033	0.876	0.083	0.006
	0.046	0.851	0.093	0.008
	0.040	0.859	0.094	0.005
	0.031	0.881	0.081	0.005
	0.051	0.846	0.095	0.005
	0.054	0.865	0.069	0.011
	0.038	0.883	0.067	0.010
	0.051	0.857	0.082	0.009
	0.052	0.886	0.056	0.004
	0.040	0.896	0.055	0.007
	0.038	0.899	0.057	0.005
	0.043	0.874	0.077	0.005
	0.070	0.856	0.066	0.005
	0.031	0.860	0.098	0.009

SAMPLE	$CaCO_3$	$MnCO_3$	$FeCO_3$	$MgCO_3$
	0.055	0.864	0.070	0.009
	0.048	0.896	0.052	0.002
	0.052	0.885	0.057	0.002
	0.049	0.890	0.057	0.002
	0.057	0.878	0.059	0.004
	0.050	0.871	0.075	0.003
	0.071	0.847	0.073	0.006
	0.052	0.867	0.073	0.006
	0.047	0.881	0.064	0.006
	0.046	0.891	0.053	0.009
	0.026	0.892	0.062	0.019
	0.031	0.797	0.150	0.020
	0.051	0.886	0.058	0.003
	0.043	0.884	0.066	0.005
	0.041	0.799	0.151	0.006
	0.039	0.873	0.082	0.004
	0.022	0.892	0.083	0.002
	0.076	0.595	0.318	0.009
	0.046	0.864	0.081	0.006
	0.024	0.881	0.083	0.010
	0.043	0.849	0.100	0.008
	0.060	0.828	0.100	0.009
	0.041	0.896	0.055	0.006
	0.051	0.875	0.066	0.006
	0.018	0.855	0.113	0.011
	0.059	0.860	0.075	0.004
	0.027	0.843	0.124	0.004
	0.054	0.843	0.091	0.009
	0.035	0.895	0.060	0.009
	0.045	0.886	0.060	0.006
	0.044	0.619	0.319	0.016
	0.058	0.872	0.060	0.008
	0.056	0.862	0.076	0.005
	0.058	0.856	0.076	0.009

SAMPLE	$CaCO_3$	$MnCO_3$	$FeCO_3$	$MgCO_3$
PMB-UH-873-76	0.040	0.916	0.041	0.002
	0.054	0.775	0.150	0.018
	0.092	0.704	0.178	0.024
	0.079	0.697	0.206	0.017
	0.063	0.868	0.061	0.006
	0.050	0.882	0.064	0.003
	0.054	0.901	0.040	0.004
	0.072	0.700	0.214	0.011
	0.061	0.802	0.131	0.004
	0.050	0.878	0.067	0.004
	0.054	0.891	0.049	0.003
	0.025	0.902	0.067	0.003
	0.059	0.899	0.036	0.005
	0.062	0.840	0.085	0.011
	0.064	0.891	0.037	0.005
	0.038	0.925	0.034	0.001
	0.053	0.892	0.047	0.008
	0.084	0.784	0.125	0.005
	0.126	0.624	0.222	0.026
	0.045	0.907	0.041	0.004
	0.054	0.900	0.039	0.004
	0.040	0.904	0.049	0.004
	0.085	0.727	0.160	0.026
	0.070	0.720	0.189	0.018
	0.031	0.884	0.081	0.002
	0.092	0.750	0.132	0.022
	0.066	0.597	0.301	0.033
	0.027	0.932	0.038	0.002
	0.091	0.552	0.341	0.014
	0.084	0.775	0.131	0.007
	0.083	0.809	0.101	0.005
	0.061	0.882	0.054	0.001
	0.109	0.598	0.246	0.046
	0.097	0.767	0.120	0.015

SAMPLE	$CaCO_3$	$MnCO_3$	$FeCO_3$	$MgCO_3$	SAMPLE	$CaCO_3$	$MnCO_3$	$FeCO_3$	$MgCO_3$
	0.111	0.665	0.193	0.028		0.066	0.877	0.047	0.008
	0.040	0.923	0.034	0.001		0.051	0.909	0.035	0.003
	0.040	0.920	0.034	0.004		0.028	0.718	0.250	0.001
	0.053	0.888	0.055	0.002		0.034	0.667	0.292	0.006
	0.056	0.853	0.085	0.002		0.086	0.825	0.081	0.006
	0.073	0.708	0.207	0.008		0.024	0.691	0.279	0.004
	0.087	0.761	0.138	0.011		0.033	0.675	0.283	0.006
	0.046	0.855	0.095	0.002		0.025	0.675	0.293	0.005
	0.046	0.877	0.074	0.001		0.027	0.685	0.282	0.004
	0.066	0.859	0.069	0.004		0.055	0.881	0.056	0.005
	0.076	0.737	0.178	0.006		0.024	0.719	0.254	0.000
	0.059	0.883	0.052	0.004		0.072	0.851	0.069	0.005
	0.056	0.886	0.052	0.002		0.071	0.685	0.228	0.014
	0.075	0.789	0.130	0.004		0.116	0.578	0.250	0.054
	0.062	0.888	0.043	0.005		0.084	0.679	0.196	0.039
	0.051	0.836	0.107	0.003		0.067	0.895	0.033	0.003
	0.051	0.884	0.055	0.009		0.035	0.876	0.083	0.005
	0.051	0.806	0.133	0.007		0.090	0.732	0.154	0.021
	0.071	0.889	0.034	0.004		0.107	0.602	0.241	0.048
	0.024	0.888	0.081	0.005		0.053	0.667	0.240	0.037
	0.071	0.756	0.162	0.009		0.100	0.524	0.307	0.068
	0.062	0.774	0.154	0.007		0.103	0.677	0.190	0.028
	0.073	0.787	0.132	0.005		0.078	0.667	0.220	0.032
	0.069	0.886	0.038	0.004		0.085	0.712	0.190	0.011
	0.079	0.882	0.036	0.001		0.073	0.800	0.120	0.005
	0.064	0.898	0.032	0.002		0.036	0.846	0.111	0.005
	0.027	0.705	0.266	0.000		0.078	0.675	0.230	0.014
	0.022	0.690	0.283	0.002		0.076	0.714	0.179	0.029
	0.030	0.671	0.293	0.004		0.088	0.662	0.233	0.015
	0.063	0.868	0.062	0.005		0.083	0.665	0.219	0.031
	0.071	0.824	0.095	0.007		0.087	0.700	0.191	0.020
	0.024	0.699	0.271	0.005		0.058	0.899	0.035	0.004
	0.064	0.660	0.263	0.011		0.039	0.907	0.047	0.003
	0.123	0.583	0.248	0.045		0.037	0.792	0.163	0.006

SAMPLE	$CaCO_3$	$MnCO_3$	$FeCO_3$	$MgCO_3$
	0.056	0.907	0.032	0.003
	0.030	0.883	0.080	0.003
	0.047	0.906	0.040	0.004
	0.053	0.756	0.178	0.011
		AMETHYST VEIN		
PMB-FW-331-68	0.050	0.898	0.042	0.009
	0.052	0.884	0.055	0.006
	0.029	0.928	0.039	0.004
	0.070	0.885	0.037	0.006
	0.067	0.881	0.046	0.004
	0.064	0.900	0.029	0.005
	0.059	0.905	0.031	0.004
	0.051	0.907	0.035	0.005
	0.061	0.902	0.029	0.004
	0.062	0.902	0.032	0.002
	0.061	0.882	0.044	0.009
PMB-II-441-70	0.041	0.924	0.031	0.002
	0.037	0.905	0.056	0.002
	0.059	0.905	0.029	0.005
	0.049	0.917	0.026	0.005
	0.053	0.921	0.022	0.003
	0.050	0.916	0.027	0.005
	0.074	0.896	0.024	0.004
PBB-123-47-68	0.034	0.925	0.035	0.005
	0.063	0.909	0.023	0.002
	0.038	0.873	0.080	0.008
	0.046	0.912	0.036	0.003
	0.057	0.900	0.038	0.002
	0.061	0.905	0.018	0.004

SAMPLE	$CaCO_3$	$MnCO_3$	$FeCO_3$	$MgCO_3$
	0.057	0.904	0.036	0.002
	0.049	0.905	0.042	0.002
PMB-FO-322-68	0.060	0.858	0.073	0.007
	0.037	0.920	0.037	0.004
	0.042	0.917	0.035	0.002
	0.035	0.914	0.042	0.007
	0.047	0.887	0.049	0.015
	0.055	0.891	0.042	0.009
PMB-LG-582-74	0.056	0.516	0.414	0.011
	0.059	0.524	0.406	0.008
	0.066	0.595	0.328	0.009
	0.061	0.585	0.344	0.008
	0.053	0.696	0.237	0.013
	0.050	0.555	0.381	0.011
	0.050	0.555	0.382	0.013
	0.061	0.504	0.422	0.011
	0.052	0.492	0.446	0.007
	0.050	0.593	0.346	0.008
	0.047	0.550	0.390	0.010
	0.059	0.558	0.371	0.010
		OH VEIN		
PBB-44-159-59	0.029	0.369	0.573	0.026
	0.053	0.253	0.679	0.012
	0.031	0.643	0.305	0.018
	0.042	0.364	0.578	0.014
	0.042	0.468	0.473	0.015
	0.041	0.478	0.465	0.015
	0.039	0.431	0.508	0.019
	0.041	0.534	0.406	0.017

SAMPLE	$CaCO_3$	$MnCO_3$	$FeCO_3$	$MgCO_3$
	0.048	0.389	0.547	0.014
	0.045	0.377	0.555	0.021
	0.035	0.431	0.509	0.022
	0.034	0.612	0.337	0.014
	0.034	0.586	0.363	0.016
	0.043	0.491	0.450	0.014
	0.054	0.340	0.595	0.009
	0.040	0.447	0.499	0.013
	0.051	0.418	0.509	0.021
	0.029	0.515	0.441	0.013
	0.050	0.343	0.592	0.014
	0.051	0.509	0.430	0.009
	0.040	0.579	0.365	0.014
	0.052	0.320	0.616	0.011
	0.038	0.666	0.283	0.011
	0.041	0.518	0.426	0.012
	0.056	0.365	0.562	0.015
	0.060	0.313	0.612	0.013
	0.047	0.469	0.465	0.016
	0.066	0.480	0.440	0.011
PBB-40-123-59	0.007	0.072	0.919	0.001
	0.010	0.060	0.926	0.001
	0.009	0.089	0.893	0.006
	0.031	0.025	0.921	0.021
	0.023	0.136	0.827	0.012
	0.010	0.101	0.888	0.001
	0.008	0.064	0.921	0.004
	0.006	0.068	0.921	0.002
	0.010	0.062	0.914	0.013
	0.083	0.007	0.833	0.075
	0.084	0.006	0.867	0.042
	0.011	0.053	0.928	0.005
	0.094	0.007	0.851	0.044

SAMPLE	$CaCO_3$	$MnCO_3$	$FeCO_3$	$MgCO_3$
	0.070	0.009	0.868	0.052
	0.065	0.006	0.884	0.042
	0.087	0.008	0.869	0.034
	0.008	0.054	0.930	0.004
	0.078	0.007	0.854	0.060
	0.083	0.007	0.863	0.045
	0.087	0.015	0.853	0.043
	0.099	0.011	0.842	0.045
	0.015	0.089	0.891	0.004
	0.007	0.052	0.936	0.004
	0.103	0.007	0.837	0.052
	0.007	0.068	0.922	0.001
	0.036	0.337	0.616	0.009
	0.077	0.008	0.876	0.037
	0.088	0.004	0.845	0.060
	0.112	0.008	0.824	0.052
	0.097	0.018	0.837	0.046
	0.104	0.004	0.842	0.048
	0.078	0.007	0.869	0.044
PBB-38-116-59	0.110	0.018	0.815	0.056
	0.095	0.004	0.835	0.063
	0.112	0.024	0.805	0.057
	0.104	0.002	0.832	0.060
	0.129	0.040	0.762	0.067
	0.118	0.032	0.793	0.054
	0.104	0.057	0.746	0.091
	0.125	0.039	0.766	0.068
	0.131	0.035	0.744	0.088
	0.116	0.017	0.813	0.052
	0.118	0.025	0.800	0.054
ER-123-65	0.098	0.062	0.747	0.091
	0.074	0.093	0.739	0.092

SAMPLE	$CaCO_3$	$MnCO_3$	$FeCO_3$	$MgCO_3$
	0.035	0.209	0.715	0.038
	0.012	0.203	0.782	0.001
	0.099	0.060	0.741	0.097
	0.099	0.083	0.737	0.080
	0.096	0.144	0.725	0.034
	0.092	0.078	0.779	0.048
	0.095	0.044	0.810	0.049
	0.096	0.050	0.799	0.053
	0.104	0.087	0.731	0.076
	0.091	0.053	0.758	0.095
	0.016	0.235	0.739	0.006
	0.099	0.074	0.750	0.075
	0.098	0.046	0.800	0.054
	0.095	0.055	0.795	0.053
	0.013	0.185	0.775	0.025
	0.016	0.221	0.751	0.011
	0.078	0.063	0.840	0.017
	0.103	0.123	0.719	0.053
	0.100	0.060	0.764	0.075
	0.109	0.074	0.752	0.062
	0.109	0.071	0.727	0.093
	0.009	0.193	0.789	0.008
	0.069	0.187	0.700	0.042
	0.034	0.409	0.544	0.010
	0.053	0.277	0.657	0.010
	0.101	0.118	0.731	0.049
PBB-32-103-59	0.106	0.050	0.784	0.058
	0.087	0.048	0.817	0.045
	0.099	0.019	0.824	0.057
	0.114	0.050	0.766	0.069
	0.099	0.034	0.819	0.046
	0.094	0.029	0.825	0.050
	0.106	0.025	0.816	0.049

SAMPLE	$CaCO_3$	$MnCO_3$	$FeCO_3$	$MgCO_3$
	0.115	0.050	0.769	0.065
	0.098	0.034	0.832	0.035
	0.089	0.053	0.816	0.039
	0.095	0.025	0.829	0.049
	0.095	0.046	0.814	0.043
	0.094	0.021	0.836	0.046
	0.096	0.054	0.806	0.043
	0.092	0.023	0.833	0.052
	0.023	0.159	0.812	0.003
	0.023	0.197	0.774	0.003
	0.115	0.031	0.804	0.048
	0.094	0.057	0.804	0.044
	0.089	0.085	0.778	0.044
	0.099	0.029	0.818	0.052
	0.033	0.335	0.624	0.006
	0.034	0.257	0.702	0.004
	0.043	0.293	0.651	0.011
	0.022	0.199	0.771	0.005
	0.106	0.052	0.784	0.055
	0.104	0.070	0.758	0.065
	0.098	0.092	0.756	0.051
	0.030	0.103	0.860	0.005
	0.040	0.191	0.746	0.020
	0.026	0.306	0.659	0.006
	0.095	0.022	0.828	0.053
	0.113	0.040	0.765	0.080
	0.113	0.050	0.767	0.069
	0.100	0.028	0.822	0.048
	0.033	0.192	0.761	0.012
	0.024	0.209	0.760	0.004
PBB-28-90-59	0.092	0.041	0.822	0.043
	0.106	0.023	0.828	0.042
	0.099	0.015	0.848	0.036

SAMPLE	$CaCO_3$	$MnCO_3$	$FeCO_3$	$MgCO_3$
	0.086	0.029	0.833	0.050
	0.096	0.017	0.838	0.048
	0.104	0.062	0.777	0.056
	0.018	0.132	0.842	0.005
	0.015	0.063	0.898	0.021
	0.095	0.018	0.835	0.051
	0.015	0.068	0.890	0.024
	0.011	0.113	0.866	0.008
	0.101	0.010	0.851	0.036
	0.097	0.024	0.823	0.055
	0.017	0.083	0.861	0.038
	0.029	0.118	0.824	0.027
	0.076	0.049	0.822	0.051
	0.066	0.062	0.828	0.042
	0.037	0.032	0.902	0.026
	0.025	0.118	0.832	0.022
	0.025	0.094	0.833	0.045
ER-119-65	0.087	0.011	0.863	0.038
	0.104	0.005	0.832	0.057
	0.101	0.008	0.840	0.050
	0.099	0.008	0.837	0.054
	0.098	0.009	0.841	0.050
	0.101	0.005	0.838	0.054
	0.115	0.015	0.820	0.049
	0.114	0.016	0.811	0.057
	0.039	0.055	0.877	0.028
	0.030	0.069	0.888	0.010
	0.038	0.023	0.912	0.025
	0.113	0.010	0.813	0.063
	0.101	0.013	0.866	0.018
	0.106	0.008	0.834	0.050
	0.093	0.011	0.835	0.059
	0.117	0.006	0.820	0.055

SAMPLE	$CaCO_3$	$MnCO_3$	$FeCO_3$	$MgCO_3$
	0.110	0.006	0.827	0.054
	0.108	0.006	0.832	0.052
	0.134	0.003	0.800	0.061
	0.111	0.006	0.837	0.044
	0.130	0.007	0.807	0.054
	0.068	0.005	0.861	0.064
	0.122	0.006	0.818	0.053
PBB-130-32-67	0.111	0.241	0.633	0.013
	0.104	0.018	0.840	0.036
	0.109	0.016	0.822	0.051
	0.022	0.241	0.726	0.010
	0.027	0.202	0.749	0.021
	0.094	0.027	0.798	0.078
	0.100	0.013	0.824	0.062
	0.087	0.017	0.838	0.056
	0.086	0.035	0.828	0.049
	0.083	0.025	0.813	0.077
	0.085	0.026	0.813	0.073
	0.025	0.110	0.848	0.015
	0.010	0.169	0.792	0.026
	0.050	0.113	0.811	0.023
	0.102	0.022	0.836	0.038
	0.086	0.030	0.805	0.077
	0.097	0.017	0.836	0.048
	0.020	0.228	0.731	0.019
PMB-BO-227-65	0.097	0.080	0.805	0.017
	0.017	0.159	0.821	0.002
	0.031	0.199	0.752	0.017
	0.121	0.027	0.778	0.072
	0.031	0.183	0.769	0.016
	0.097	0.033	0.804	0.064
	0.112	0.018	0.808	0.060

SAMPLE	$CaCO_3$	$MnCO_3$	$FeCO_3$	$MgCO_3$
	0.043	0.184	0.753	0.017
	0.025	0.208	0.748	0.018
PMB-RV-241-65	0.056	0.420	0.506	0.016
	0.042	0.535	0.415	0.005
	0.059	0.319	0.604	0.016
	0.045	0.459	0.476	0.017
	0.056	0.306	0.624	0.012
	0.038	0.441	0.498	0.021
	0.025	0.175	0.782	0.017
	0.031	0.226	0.727	0.014
	0.050	0.484	0.447	0.018
PMB-CI-258-65	0.063	0.882	0.047	0.006
	0.035	0.890	0.039	0.035
	0.038	0.895	0.060	0.005
	0.035	0.924	0.036	0.003
	0.049	0.887	0.058	0.004
PMB-K-50-59	0.051	0.480	0.451	0.017
	0.042	0.481	0.458	0.017
	0.025	0.460	0.498	0.013
	0.051	0.469	0.462	0.016
	0.015	0.389	0.577	0.018
	0.027	0.473	0.485	0.013
	0.017	0.400	0.571	0.011
	0.035	0.487	0.464	0.010
	0.024	0.438	0.521	0.013
	0.020	0.400	0.567	0.011
	0.015	0.438	0.533	0.010
	0.034	0.427	0.524	0.012
	0.030	0.437	0.518	0.013
	0.017	0.403	0.562	0.017
	0.033	0.384	0.561	0.020

SAMPLE	$CaCO_3$	$MnCO_3$	$FeCO_3$	$MgCO_3$
	0.030	0.430	0.520	0.019
	0.026	0.431	0.528	0.013
	0.023	0.408	0.553	0.013
	0.056	0.479	0.449	0.014
	0.023	0.453	0.504	0.017
	0.020	0.407	0.563	0.008
PBB-112-36C-68	0.024	0.666	0.302	0.005
	0.046	0.677	0.258	0.016
	0.042	0.673	0.274	0.008
	0.056	0.680	0.249	0.014
	0.035	0.714	0.239	0.009
	0.054	0.704	0.229	0.011
	0.034	0.624	0.333	0.007
	0.052	0.695	0.241	0.010
	0.022	0.679	0.292	0.005
	0.042	0.699	0.246	0.011
PBB-25-35H-68	0.051	0.919	0.025	0.003
	0.046	0.883	0.028	0.040
	0.043	0.891	0.050	0.016
	0.023	0.905	0.065	0.005
	0.044	0.815	0.127	0.012
	0.057	0.858	0.057	0.024
	0.029	0.883	0.068	0.018
	0.045	0.881	0.056	0.015
	0.030	0.903	0.060	0.005
	0.045	0.917	0.032	0.003
	0.055	0.881	0.054	0.009
	0.058	0.517	0.410	0.014
	0.031	0.910	0.055	0.002
	0.044	0.889	0.049	0.015
	0.022	0.916	0.058	0.002
	0.031	0.660	0.301	0.007

SAMPLE	$CaCO_3$	$MnCO_3$	$FeCO_3$	$MgCO_3$
	0.034	0.901	0.060	0.003
	0.056	0.401	0.527	0.013
	0.050	0.877	0.055	0.016
	0.048	0.907	0.036	0.006
	0.030	0.893	0.042	0.033
	0.027	0.906	0.055	0.009
PBB-113-37-68	0.047	0.890	0.049	0.011
	0.027	0.929	0.036	0.006
	0.041	0.894	0.053	0.009
	0.043	0.886	0.053	0.016
		P VEIN		
PBB-159-11-76	0.025	0.098	0.850	0.025
	0.044	0.112	0.807	0.036
	0.011	0.303	0.684	0.001
	0.051	0.123	0.813	0.010
	0.012	0.317	0.666	0.002
	0.056	0.146	0.780	0.016
	0.115	0.017	0.818	0.047
	0.017	0.303	0.677	0.001
	0.114	0.020	0.823	0.042
	0.018	0.356	0.624	0.000
	0.075	0.383	0.528	0.012
	0.109	0.028	0.811	0.049
	0.109	0.024	0.819	0.046
	0.109	0.021	0.817	0.051
	0.024	0.399	0.573	0.001
	0.055	0.158	0.766	0.020
	0.015	0.270	0.711	0.001
	0.042	0.229	0.706	0.021
	0.072	0.327	0.584	0.016

SAMPLE	$CaCO_3$	$MnCO_3$	$FeCO_3$	$MgCO_3$
	0.012	0.105	0.875	0.005
	0.020	0.083	0.892	0.005
	0.015	0.095	0.876	0.012
	0.010	0.088	0.891	0.008
PHW-A-1-75	0.125	0.855	0.009	0.010
	0.061	0.862	0.070	0.004
	0.127	0.853	0.009	0.009
	0.104	0.864	0.019	0.011
	0.077	0.832	0.065	0.024
	0.077	0.831	0.061	0.028
	0.088	0.815	0.063	0.032
	0.075	0.807	0.028	0.088
	0.063	0.832	0.035	0.069
	0.050	0.832	0.042	0.074
	0.056	0.889	0.050	0.002
	0.056	0.905	0.032	0.003
	0.065	0.888	0.043	0.002
	0.065	0.849	0.072	0.011
	0.066	0.812	0.068	0.052
	0.076	0.819	0.049	0.054
		EQUITY MINE		
PHW-BQ-96-75	0.065	0.907	0.017	0.009
	0.055	0.906	0.025	0.012
	0.056	0.880	0.032	0.030
PMB-HT-421-70	0.117	0.735	0.141	0.005
	0.083	0.822	0.083	0.010
	0.040	0.930	0.020	0.008
	0.095	0.867	0.020	0.016

LIST OF REFERENCES

Albee, A.L., and Ray, Lily (1970) Correction factors for electron probe microanalysis of silicates, oxides, carbonates, phosphates, and sulfates: Analytical Chemistry, vol. 42, p. 1408-1414.

Barton, P.B., Jr., Bethke, P.M., and Roedder, E. (1977) Environment of ore deposition in the Creede mining district, San Juan Mountains, Colorado: Part III. Progress toward the interpretation of the chemistry of the ore-forming fluid for the OH vein: Econ. Geol., vol. 72, p. 1-24.

Barton, P.B., Jr., Bethke, P.M., and Toulmin, P., 3rd (1963) Equilibrium in ore deposits: Min. Soc. of America Special Paper 1, p. 171-185.

Bence, A.E., and Albee, A.L. (1968) Empirical correction factors for the electron microanalysis of silicates and oxides: Journal of Geology, vol. 76, p. 382-403.

Bertin, E.P. (1971) Principles and practice of X-ray spectrometric analysis: Plenum Press, New York, 679 p.

Bethke, P.M., and Barton, P.B., Jr. (1971) History of filling of the OH vein, Creede, Colorado: Econ. Geol., vol. 66, p. 1265.

Bethke, P.M., Barton, P.B., Jr., Lanphere, M.A., and Steven, T.A. (1976) Environment of ore deposition of the Creede mining district, San Juan Mountains, Colorado: II. Age of mineralization: Econ. Geol., vol. 71, p. 1006-1011.

Bottinga, Y. (1968) Calculation of fractionation factors for carbon and oxygen isotopic exchange in the system calcite-carbon dioxide-water: J. Phys. Chem., vol. 72, p. 800-808.

Bottinga, Y., and Javoy, M. (1973) Comments on oxygen isotope geothermometry: Earth Planet. Sci. Letters, vol. 20, p. 250-265.

Brown, W.L. (1934) The fluorescence of manganiferous calcites: University of Toronto Studies, Geological series no. 36, p. 45-53.

Cannaday, F.X. (1950) The OH vein and its relation to the Amethyst fault: unpublished Master's thesis, Colorado School of Mines, 57 p.

Chaffee, M.A. (1967) A study of the geology and hydrothermal alteration north of the Creede mining district, Mineral, Hinsdale and Saguache Counties, Colorado: unpublished Ph.D. dissertation, University of Arizona, 194 p.

Clayton, R.N., O'Neil, J.R., and Mayeda, T.K. (1972) Oxygen isotope exchange between quartz and water: Jour. Geophys. Research, v. 77, no. 17, p. 3057-3067.

Craig, Harmon (1957) Isotopic standards for carbon and oxygen and correction factors for mass-spectrometric analyses of carbon dioxide: Geochim. et Cosmochim. Acta, vol. 12, p. 133-149.

Craig, Harmon (1961) Standards for reporting concentrations of deuterium and oxygen-18 in natural waters: Science, vol. 133, p. 1833-1834.

Deer, W.A., Howie, R.A., and Zussman, J. (1962) Rock-forming minerals: Vol. 5 Non-silicates, New York, John Wiley and Sons, Inc., 371 p.

Emmons, W.H., and Larsen, E.S. (1913) A preliminary report on the geology and ore deposits of Creede, Colorado: U.S. Geol. Survey Bull. 530, p. 42-65.

Emmons, W.H., and Larsen, E.S. (1923) Geology and ore deposits of the Creede District, Colorado: U.S. Geol. Survey Bull. 718, 193 p.

French, Bevan M. (1971) Stability relations of siderite ($FeCO_3$) in the system Fe-C-O: American Journal of Science, vol. 271, p. 37-78.

Haas, J.L., Jr. (1970) Fugacity of H_2O from 0° to 350°C at the liquid-vapor equilibrium and at 1 atmosphere: Geochim. et Cosmochim. Acta, vol. 34,

p. 929-932.

Haas, J.L., Jr. (1971) The effect of salinity on the maximum thermal gradient of a hydrothermal system at hydrostatic pressure: Econ. Geol., vol. 66, p. 940-946.

Haas, J.L., Jr., and Robie, R.A. (1973) Thermodynamic data for wüstite, $Fe_{0.947}O$, magnetite, Fe_3O_4, and hematite, Fe_2O_3 [abs.]: Am. Geophys. Union Trans., vol. 54, p. 438.

Holland, H.D. (1959) Some applications of thermochemical data to problems of ore deposits. I. Stability relations among the oxides, sulfides, sulfates and carbonates of ore and gangue minerals: Econ. Geol., vol. 54, p. 184-233.

Holland, H.D. (1965) Some applications of the thermochemical data to problems of ore deposits. II. Mineral assemblages and the composition of ore-forming fluids: Econ. Geol., vol. 60, p. 1101-1166.

Hull, D.A. (1970) Geology of the Puzzle Vein, Creede mining district, Colorado: unpublished Ph.D. dissertation, University of Nevada, Reno, 151 p.

Jackson, Daniel, Jr. (1974) Homestake's hard work pays off at Bulldog Mountain mine: Engineering and Mining Journal, vol. 5, p. 65-70.

Krauskopf, K.B. (1968) A tale of ten plutons: Geol. Soc. America Bull. 79, p. 1-17.

Larsen, E.S. (1930) Recent mining developments in the Creede district, Colorado: U.S. Geol. Survey Bull. 811, p. 89-112.

Larsen, E.S., Jr., and Cross, W. (1956) Geology and petrology of the San Juan region, southwestern Colorado: U.S. Geol. Survey Prof. Paper 258, 303 p.

Lipman, P.W., Fisher, F.S., Mehnert, H.H., Naeser, C.W., Luedke, R.G., Steven, T.A. (1976) Multiple ages of mid-Tertiary mineralization and alteration

in the western San Juan Mountains, Colorado: Econ. Geol., vol 71, p. 571-588.

Lipman, P.W., Steven, T.A., and Mehnhart, H. (1970) Volcanic history of the San Juan Mountains, Colorado, as indicated by potassium-argon dating: Geol. Soc. America Bull. 81, p. 2329-2352.

Meeves, H.C., and Darnell, R.P. (1968) Study of the silver potential, Creede District, Mineral County, Colorado: Bureau of Mines Information Circular 8370, 58 p.

Montoya, J.W., and Hemley, J.J. (1975) Activity relations and stabilities in alkali feldspar and mica alteration reactions: Econ. Geol., vol 70, p. 577-582.

Ohmoto, H., and Rye, R.O. (1970) The Bluebell Mine, British Columbia. I. Mineralogy, paragenesis, fluid inclusions, and the isotopes of hydrogen, oxygen, and carbon: Econ. Geol., vol. 65, p. 417-437.

O'Neil, J.R., Clayton, R.N., and Mayeda, T. (1969) Oxygen isotope fractionation in divalent metal carbonates: Jour. Chem. Physics, vol. 51, p. 5547-5548.

Ratté, J.C., and Steven, T.A. (1967) Ash flows and related rocks associated with the Creede caldera, San Juan Mountains, Colorado: U.S. Geol. Survey Prof. Paper 524-H, 58 p.

Reddick, K.L. (1968) Heats of reaction for carbonate mineral deposition: Symposium on Analytical Calorimetry, Division of Polymer Chemistry, American Chemical Society, San Francisco Meeting, March 31-April 5, 1968, p. 1033-1038.

Robie, R.A., Hemingway, B.S., Fisher, J.R. (in press) Thermodynamic properties of minerals and related substances at 298.15 K and one bar: U.S. Geol. Survey Bull.

Robie, R.A., and Waldbaum, D.R. (1968) Thermodynamic properties of minerals

and related substances at 298.15°K (25.0°C) and one atmosphere (1.013 bars) pressure and at higher temperatures: U.S. Geol. Survey Bull. 1259, 255 p.

Roedder, E. (1965) Evidence from fluid inclusions as to the nature of the ore-forming fluids: Symposium on problems of post-magnetic ore deposition, Prague 1963, Prague Geol. Survey Czechoslovakia, vol. 2, p. 375-384.

Roedder, E. (1977) SEG distinguished lecture in scientific research: Fluid inclusions as tools in mineral exploration: Econ. Geol., vol 72, p. p. 503-525.

Rosenberg, P.E. (1960) Subsolidus studies in the system $CaCO_3$-$MgCO_3$-$FeCO_3$-$MnCO_3$: Ph.D. thesis, Pennsylvania State University, 135 p.

Rosenberg, P.E. (1963a) Subsolidus relations in the system $CaCO_3$-$FeCO_3$: Amer. Jour. Sci., vol. 261, p. 683-690.

Rosenberg, P.E. (1963b) Synthetic solid solutions in the systems $MgCO_3$-$FeCO_3$ and $MnCO_3$-$FeCO_3$: Amer. Mineral., vol. 48, p. 1396-1400.

Rosenberg, P.E. (1967) Subsolidus relations in the system $CaCO_3$-$MgCO_3$-$FeCO_3$ between 350° and 550°C: Amer. Mineral., vol. 52, p. 787-796.

Rosenberg, P.E. (1968) Subsolidus relations on the dolomite join $CaMg(CO_3)_2$-$CaFe(CO_3)_2$-$CaMn(CO_3)_2$: Amer. Mineral., vol 53, p. 880-889.

Rye, R.O. (1966) The carbon, hydrogen, and oxygen isotopic composition of the hydrothermal fluids responsible for the lead-zinc deposits at Providencia, Zacatecas, Mexico: Econ. Geol., vol. 61, p. 1399-1427.

Rye, R.O., and Sawkins, F.J. (1974) Fluid inclusion and stable isotope studies on the Casapalca Ag-Pb-Zn-Cu deposit, central Andes, Peru: Econ. Geol., vol. 69, p. 181-205.

Shikazono, Naotatsu (1977) Composition of siderite and the environments of formation of vein-type deposits in Japan: Econ. Geol., vol 72, p. 632-641.

Smith, R.L. (1960) Zones and zonal variations in welded ash flows: U.S. Geol. Survey Prof. Paper 354-F, p. 149-159.

Smith, R.L., and Bailey, R.A. (1968) Resurgent cauldrons, in Coats, R.R., Hay, R.L., and Anderson, C.A., eds., Studies in volcanology - A memoir in honor of Howel Williams: Geol. Soc. America Mem. 116, p. 613-662.

Steven, T.A. (1969) Possible relation of mineralization to thermal springs in the Creede district, San Juan Mountains, Colorado: A discussion: Econ. Geol., vol. 64, p. 696-698.

Steven, T.A., and Eaton, G.P. (1975) Environment of ore deposition in the Creede mining district, San Juan Mountains, Colorado: I. Geologic, hydrologic, and geophysical setting: Econ. Geol., vol. 70, p. 1023-1037

Steven, T.A., and Friedman, I. (1968) The source of travertine in the Creede Formation, San Juan Mountains, Colorado: U.S. Geol. Survey Prof. Paper 600-B, p. B29-B36.

Steven, T.A., and Lipman, P.W. (1976) Calderas of the San Juan volcanic field, southwestern Colorado: U.S. Geol. Survey Prof. Paper 95B, 35p.

Steven, T.A., Mehnert, H.H., and Obradovich, J.D. (1967) Age of volcanic activity in the San Juan Mountains, Colorado, in Geological Survey Research 1967: U.S. Geol. Survey Prof. Paper 575-D, p. D47-D55.

Steven, T.A., and Ratté, J.C. (1960) Relation of mineralization to caldera subsidence in the Creede district, San Juan Mountains, Colorado, in Short papers in the geological sciences: U.S. Geol. Survey Prof. Paper 400-B, P. B14-B17.

Steven, T.A., and Ratté, J.C. (1965) Geology and structural control of ore deposition in the Creede district, San Juan Mountains, Colorado: U.S. Geol. Survey Prof. Paper 487, 90 p.

Steven, T.A., and Ratté, J.C. (1973) Geology of the Creede quadrangle, Mineral

and Saguache Counties, Colorado: U.S. Geol. Survey Geol. Quad. Map, GQ-1053.

Tweto, O. (1968) Geologic setting and interrelationships of mineral deposits in the Mountain Province of Colorado and south-central Wyoming, p. 551-588, in Ore Deposits of the United States, 1933-1967, vol. 1: The Am. Inst. of Mining, Metall. and Petroleum Eng. Inc., New York, 990 p.

A

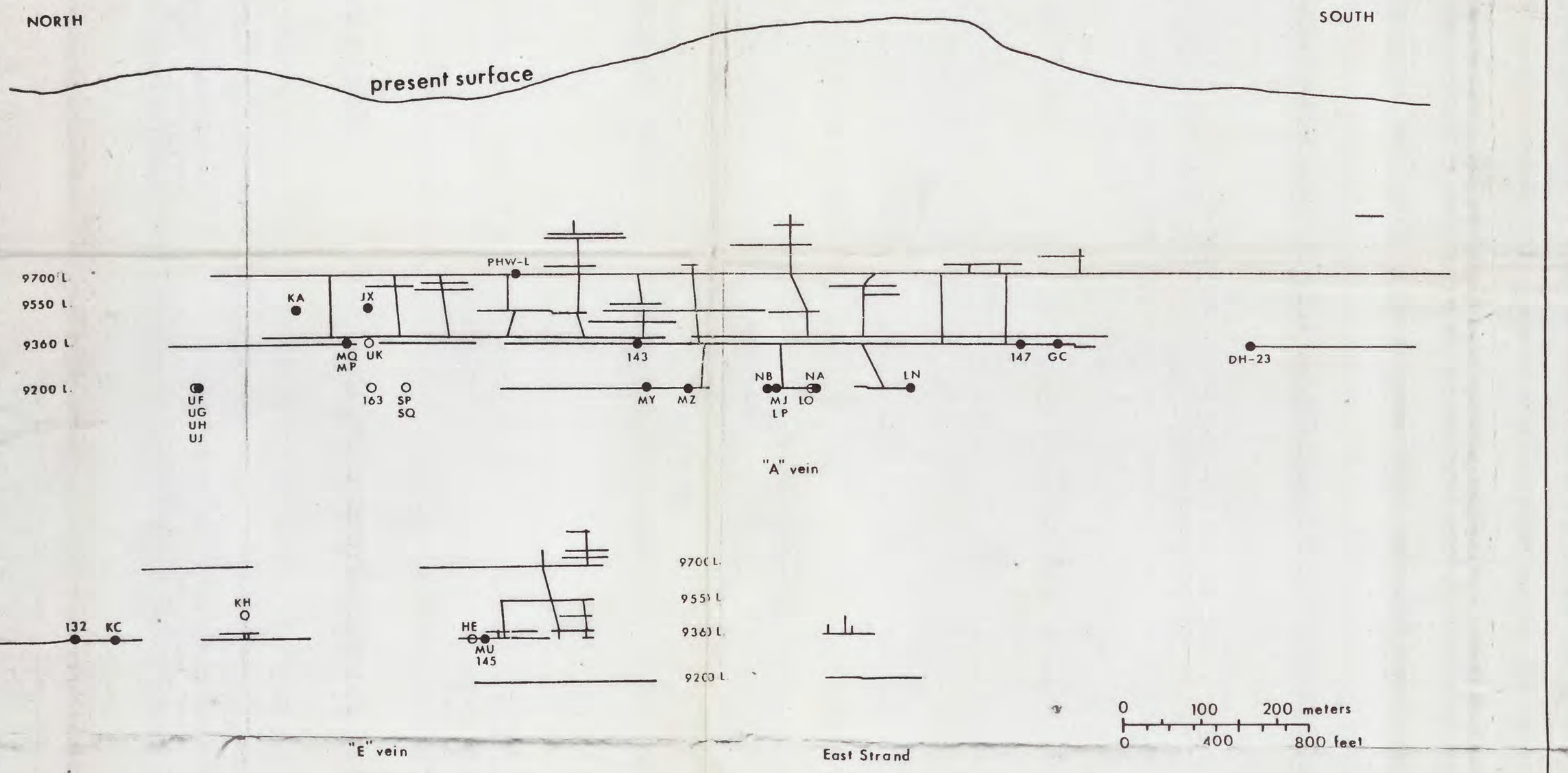

Bulldog vein*

B

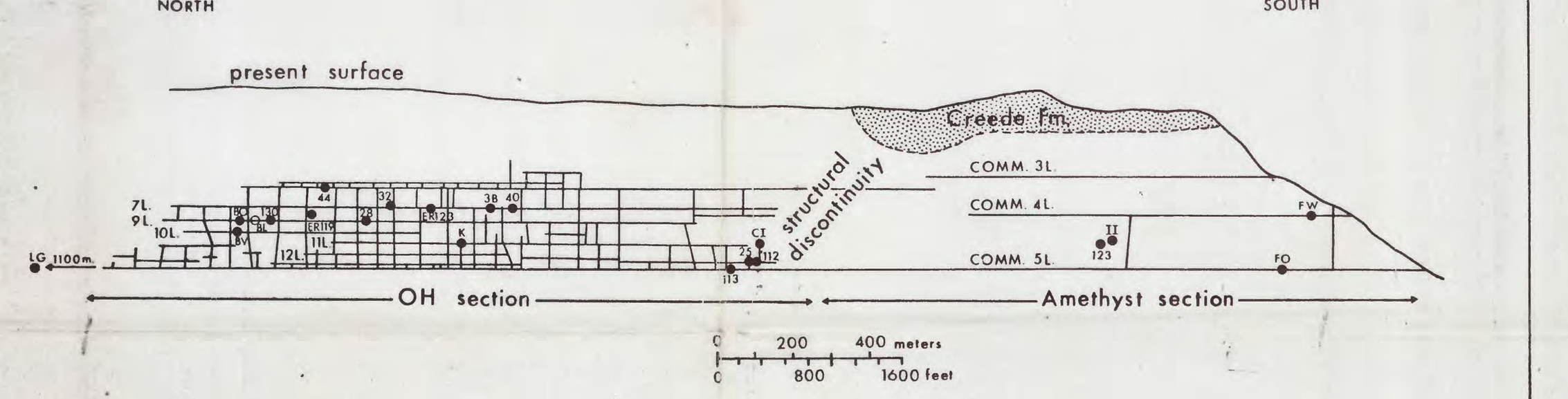

C

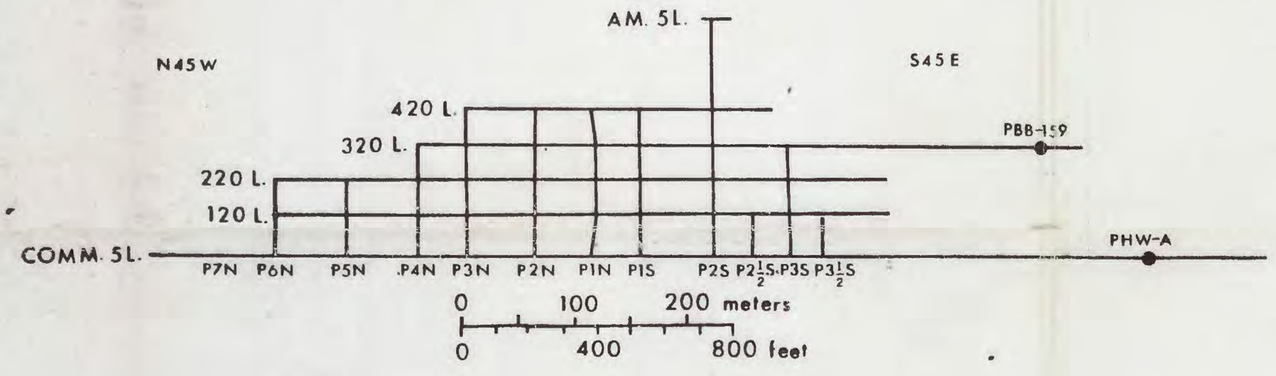

P vein

D

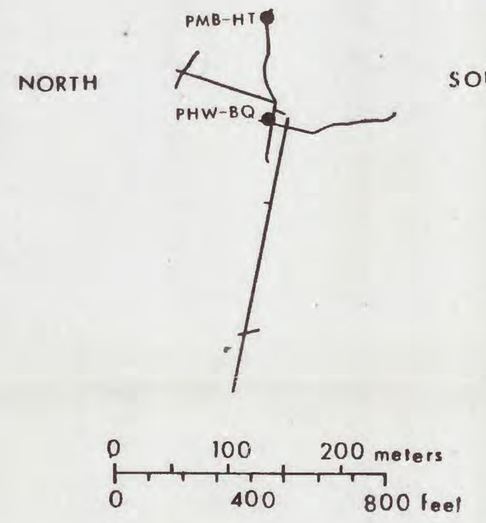

Equity mine

Plate 1. Distribution of sample localities within the Creede mining district. A) longitudinal section of the Bulldog vein*; B) longitudinal section of the southern Amethyst and OH veins (sample PMB-LG has been projected onto the OH vein from the Amethyst vein, and sample PMB-FW, which lies off-structure, has been projected onto the Amethyst vein); C) longitudinal section of the P vein; D) plan view of the Equity mine (from Steven and Ratté, 1965). Sample localities designated only by numerals have had the 'PBB' prefix dropped; sample localities designated only by alphabetical characters have had the 'PMB' prefix dropped. Solid circles denote localities in which the carbonate has been analyzed by electron microprobe; open circles denote localities in which the carbonate has not been analyzed.

*The Bulldog vein system consists of several splits or branches. The major development has been along the "A" vein. Workings along the "E" vein and the East Strand are shown below the "A" vein in their proper north-south position. Redrawn from longitudinal section supplied by Homestake Mining Company.

77-706